Title
Multiscale in-situ spatiotemporal characterization of polymers

Author
Huynh, Nha Uyen Tran

Publication Date
2022

UNIVERSITY OF CALIFORNIA SAN DIEGO

SAN DIEGO STATE UNIVERSITY

Multiscale In-situ Spatiotemporal Characterization of Polymers

A Dissertation submitted in partial satisfaction of the requirements
for the degree Doctor of Philosophy

in

Engineering Sciences (Mechanical and Aerospace Engineering)

by

Nha Uyen Huynh

Committee in charge:

San Diego State University

Professor George Youssef, Co-Chair
Professor Wenwu Xu

University of California, San Diego

Professor Prabhakar Bandaru, Co-Chair
Professor Shengqiang Cai
Professor Yu Qiao

2022

The Dissertation of Nha Uyen Huynh is approved, and it is acceptable in quality and form for publication on microfilm and electronically.

University of California San Diego

San Diego State University

2022

DEDICATION

This dissertation is dedicated to my mother, Thu Tran and my father, Cung Huynh, whose sacrifices and commitment to raising four independent, strong women have not been squandered.

TABLE OF CONTENTS

LIST OF FIGURES

LIST OF TABLES

ACKNOWLEDGEMENTS

First, I would like to extend my deepest gratitude and appreciation to my advisor, Professor George Youssef, for his unwavering support, guidance, and push for me to recognize and achieve my ambitions. His vast technical skills, passionate work ethics, and commendable leadership is tough to match; as long as I strive to be a reputable colleague, I will be successful in my professional endeavors.

I would like to acknowledge my co-advisor, Professor Prabhakar Bandaru, for his insightful feedback and counsel over the past years.

I would also like to thank my committee members: Professors Shengqiang Cai, Yu Qiao, and Wenwu Xu for their positive energy and constructive assessment.

Last, but certainly not least, to my former and current colleagues of the Experimental Mechanics Laboratory, thank you for your help and encouragements. Your exemplary hard work and meticulous care for your projects inspired and affirmed my desire to pursue a doctorate.

The research leading to these results was supported by the United States Department of Defense under Grant Agreement No. W911NF1410039 and W911NF1810477. The National Science Foundation under Award No. 1925539 also supported the research. The authors are also grateful for internal funding from San Diego State University. The authors also acknowledge the use of equipment at the San Diego State University Electron Microscopy Facility acquired by NSF instrumentation grant DBI-0959908.

Chapter 1, in full, is a reprint of the material as it appears in Journal of Engineering Materials and Technology 2021. Huynh, Nha Uyen; Youssef, George, ASME, 2021. The dissertation author was the primary investigator and author of this paper.

Chapter 2, in full, is a reprint of the material as it appears in Experimental Mechanics 2020. Huynh, Nha Uyen; Youssef, George, Springer, 2020. The dissertation author was the primary investigator and author of this paper.

Chapter 3, in part, is a reprint of the material as it appears in Macromolecular Materials and Engineering 2021. Huynh, Nha Uyen; Gamez, Carlos; Youssef, George, Wiley, 2021. The dissertation author was the primary investigator and author of this paper.

Chapter 4, in full, is a reprint of the material as it appears in International Journal of Mechanical Sciences 2021. Gamez, Carlos; Huynh, Nha Uyen; Youssef, George, Science Direct, 2021. The dissertation author was the secondary investigator and author of this paper.

Chapter 5, in part, is currently being prepared for submission for publication of the material. Huynh, Nha Uyen; Koohbor, Behrad; Youssef, George. The dissertation author was the primary researcher and author of this material.

VITA

2012 Bachelor of Science in Mechanical and Aerospace Engineering, University of California, Davis

2018 Master of Science in Mechanical Engineering, San Diego State University

2022 Doctor of Philosophy in Engineering Sciences (Mechanical and Aerospace Engineering), University of California San Diego and San Diego State University

PUBLICATIONS

1. **Nha Uyen Huynh** and George Youssef. "Ex-situ Spectroscopic Characterization of Residual Effects of Thermomechanical Loading on Polyurea." Journal of Engineering Materials and Technology (2021): 1-27.

2. **Nha Uyen Huynh**, Carlos Gamez, and George Youssef. "Spectro-microscopic Characterization of Elastomers Subjected to Laser-induced Shock Waves." Macromolecular Materials and Engineering: 2100506.

3. Scott Newacheck, **Nha Uyen Huynh**, and George Youssef. “Colossal crystals in P3HT:PCBM blends for enhanced organic magnetism ” Crystal Growth & Design, Accepted 2021.

4. Carlos Gamez, **Nha Uyen Huynh**, and George Youssef. “In-silico experimentations of multimode shock response of polyurea.” International Journal of Mechanical Sciences 2021, 204, 106542.

5. Ryan Stampfli, **Nha Uyen Huynh**, George Youssef “Long-term Converse Magnetoelectric Response of Actuated 1-3 Multiferroic Composite Structures.” Magnetochemistry, Multiferroic Materials 2021, 7, 55.

6. George Youssef, Scott Newacheck, **Nha Uyen Huynh**,and Carlos Gamez. “Multiscale characterization of E-Glass/Epoxy composite exposed to extreme environmental conditions.” Journal of Composites Science, Special Issue: Characterization and Modelling of Composites, Volume II 2021, 5, 80.

7. Aryan Blourchian, Atif Mohammed Shaik, **Nha Uyen Huynh**, and George Youssef. “Segmental Evolution of Ultraviolet Weathered Polyurea.” Journal of Polymer Research 2021, 28, 117.

8. George Youssef, Somer Nacy, and **Nha Uyen Huynh**. “Mechanics of Microspheres Reinforced Hollow Microcells.” Journal of Applied Mechanics 2021, 28, 117.

9. Dillan Stengel, J. Bennett Addison, David Onofrei, **Nha Uyen Huynh**, George Youssef, and Gregory P. Holland. “Hydration-induced β-sheet Crosslinking of a-helical-rich Spider Prey-wrapping Silk.” Advanced Functional Materials 2021, 31, 13.

10. **Nha Uyen Huynh** and George Youssef. “Physical Evidence of Stress-induced Conformational Changes in Polymers” Experimental Mechanics.” Experimental Mechanics 2020, 3, p. 1-13.

11. Sophia Do, **Nha Uyen Huynh**, Nathan Reed, Atif Mohammed Shaik, Somer Nacy, and George Youssef. “Partially-Perforated Self-Reinforced Polyurea Foams.” Applied Sciences, Advances in Foamed Polymers Special Issue 2020, 10, 5869.

12. George Youssef, Jordan Smilo, Aryan Blourchian, **Nha Uyen Huynh**, and Arbi V. Karapetian. “Multifunctional Fused Deposition Modeled Acrylonitrile Butadiene Styrene-based Structures with Embedded Conductive Channels.” Journal of Engineering Materials and Technology 2021, 143:011001.

13. **Nha Uyen Huynh**, Jordan Smilo, Aryan Blourchian, Arbi V. Karapetian, and George Youssef. “Property-Map of Epoxy-Treated and As-Printed Polymeric Additively Manufactured Materials.” International Journal of Mechanical Sciences 2020, 181, 105767.

14. Youssef, G., Nathan Reed, **Nha Uyen Huynh**, Brooke Rosenow, and Kristoffer Manlulu “Experimentally-validated Predictions of Impact Response of Polyurea Foams using Viscoelasticity based on Bulk Properties.” Mechanics of Materials 2020, 148, 103432.

15. Nathan Reed, **Nha Uyen Huynh**, Brooke Rosenow, Kristoffer Manlulu, and George Youssef. “Synthesis and Characterization of Elastomeric Polyurea Foam.” Journal of Applied Polymer Science 2019, 137, 48839.

16. Shaik, Atif Mohammed, **Nha Uyen Huynh**, and George Youssef. “Micromechanical Behavior of Ultraviolet-Exposed Polyurea.” Mechanics of Materials (2019): 103244.

17. **Nha Uyen Huynh**, Sam Kassegne, George Youssef. “Comparative study of tuning of microfabrication parameters for improving electrochemical performance of platinum and glassy carbon microelectrodes in neural prosthetics.” Journal of Microsystem Technologies 2020, 46, 775-785.

18. Hirabayashi, M., **Nha Uyen Huynh**, S. Witsell, A. Perez, L. Sandoval, N. Yamada, and S. Kassegne. “In-Vitro Real-Time Coupled Electrophysiological and Electrochemical Signals Detection with Glassy Carbon Microelectrodes.” J. Electrochemical Society 2017, 164, no. 5: B3113-B3121.

ABSTRACT OF THE DISSERTATION

Multiscale In-situ Spatiotemporal Characterization of Polymers

by

Nha Uyen Tran Huynh

Doctor of Philosophy in Engineering Sciences (Mechanical and Aerospace Engineering)

University of California San Diego, 2022
San Diego State University, 2022

Professor George Youssef, Co-Chair
Professor Prabhakar Bandaru, Co-Chair

Polymers are an important class of materials with a broad spectrum of mechanical properties that warrant their utility in various applications. Modern polymer characterization techniques have been valuable in providing multiscale insight into the structure and properties, including molecular structure and morphology, and thermal and mechanical properties, respectively. However, these techniques have been performed postmortem or have limitations that are unsuitable for in-situ characterization. The latter hinders the complete understanding of dynamic mechanical responses in polymers and the corresponding fundamental molecular mechanisms. Therefore, this research aims to develop a novel experimental solid mechanics setup capable of loading elastomeric polymers at various strain rates while concurrently interrogating the sample with a bulk spectroscopic technique using terahertz waves. The resulting time and frequency domains data and the supporting micrographs, computational and analytical solutions, digital image correlation, and light-matter interaction analyses substantiate the validity of utilizing terahertz-based spectroscopy to capture the underlying molecular mechanisms of mechanically loaded polymers. Furthermore, the fundamental insight gained through the in-situ spatiotemporal characterization of dynamically loaded polymers will accelerate the development of shock-tolerant and impact-resistant materials.

INTRODUCTION

Polymers is an essential class of material that is ubiquitous in a broad range of applications, ranging from biomedical to space. The widespread utility of polymers indicates a diverse loading condition extending over many decades of strain rates. The latter plays a major role in the mechanical performance of polymers given their time-dependent and rate-sensitivity properties. However, there exists a gap in the fundamental understanding of their behavior as it links to the molecular structure and the associated mobilities as a function of the strain rate. Therefore, the objective of this research is to develop a new experimental mechanics protocol that investigates and highlights the ultrahigh strain rate mechanical behavior of polymers. In essence, the approach is to develop an in-situ characterization technique coupling a bulk spectroscopy with a noncontact laser-induced shock wave to reveal the inter and intramolecular vibrations as well as the interrelationship in the interchain bonding and the applied load. In doing so, we can capture a comprehensive understanding of the convoluted molecular mechanisms attributed to the dynamic mechanical performance of polymers to advance the development cycle through in-situ characterization. Here, the scientific rationales for employing the laser-induced shock wave and terahertz-based spectroscopy are first introduced followed by the general structure of the dissertation. The brevity of the introduction is substantiated by a comprehensive background in each of the subsequent chapters, providing further insights into the state-of-the-art.

Materials behave differently depending on the strain rate, i.e., rate of deformation. For example, the yield strength has been shown to increase as the loading rate increases [1]. The same materials may have ductile behavior when loaded at quasi-static or low strain rate, while it experiences brittle failure as the strain rate significantly increases. When the strain-rate is above 10^2 s^{-1}, it is considered high strain rate and the load is classified as dynamic. Generally, the strain rate regimes are $10^2 < \dot{\varepsilon} < 10^4\ s^{-1}$ for high strain rate, $10^4 < \dot{\varepsilon} < 10^6\ s^{-1}$ for very high strain rate, and $\dot{\varepsilon} > 10^6$ for ultrahigh strain rate [2,3]. The latter is used to investigate fundamental material attributes such as flow stress, wave propagation, and failure processes. Different experimental techniques are used to accomplish a specific strain rate regime. Taylor impact [4] and Split-Hopkinson Pressure Bar [5–7] experimental setups are capable of loading materials at strain rates between $10^2\ s^{-1}$ and $10^5\ s^{-1}$, while Plate Impact [8] and laser-induced stress wave [9–13] techniques can load materials at ultrahigh strain rate, i.e., $\dot{\varepsilon} > 10^6$. Each of these experimental techniques has been developed to isolate the material behavior over a narrow range of loading conditions to facilitate the interpretation of test data. Since the strain rate is dependent on the duration and amplitude of the applied stress, it is difficult to simultaneously load the test structure at ultrahigh strain rate, high strain, and high amplitude applied stress. Such loading scenario, if even achievable, would be complex and difficult to interpret due to the coupling between experimental parameters. Nonetheless, subjecting materials to shock waves at different pressure levels allows the determination of the equation of state over very broad conditions and offers insights into the deformation and failure mechanisms [14,15] especially when coupled with spectroscopy technique (e.g., THz-TDS). Failure evolves through void nucleation, growth and coalescence. If sufficiently large areas fail in this manner, the material will rupture and spall, i.e., spallation. Dynamic fracture by spalling can also be achieved in brittle materials, which may begin with micro cracking and branching to form inter-granular or trans-granular fracture surfaces. Postmortem examination of the cross-sectioned sample reveals gross failure due to the large size, number and density of voids in the spall plane [16]. However, the ability of the materials to mitigate the impact prior to catastrophic failure remains unknown since in-situ interrogation currently not possible, hence the need for the proposed de nova experimental setup.

Laser-induced shock waves (LSW) were first explored in the early 1960s, after significant advancement in Q-switched lasers [15,17,18]. The basic stress wave generation process relies on focusing a high energy pulsed laser on an energy absorbent sacrificial layer. This layer absorbs the energy and undergoes extremely quick thermal expansion that launches a high amplitude shock wave into the test structure. The compressive stress wave travels through the sample and reflects either at the interface between different materials due to the acoustic impedance mismatch or at the free surface. When the amplitude of the reflected tensile wave exceeds the tensile strength of the sample, debonding of adjacent layers or spalling occurs, respectively. The amplitude of generated stress waves can be enhanced by covering the energy absorbent with a material transparent to the incident laser source. The amplitude was found to further increase by adding an opaque material between the laser absorbent layer and the constraining layer. Investigations by Gupta et al. incorporated a thin aluminum film as an energy-absorbing layer and a thin transparent coating of solid waterglass as a confining layer, as well as using an optical interferometer to measure the real time displacement of the film surface [10,12,19]. By changing the planar substrate into a triangular prism and allowing the originally generated longitudinal wave to mode-convert into a shear wave, Wang et al. successfully extended laser spallation to mixed-mode and pure-shear loading [13]. The application of this technique has been extended from the adhesion of blanket thin films [9,13,20], to patterned thin films [21,22], and adhesion between biological cells and inorganic substrates [23,24]. Youssef and coworkers used LSW technique to measure the interfacial strength of directly bonded Si-Si and Ge-GaAr wafers, which showed significant improvement in reported bond energies over traditional methods, i.e., Maszara's method [25]. Recently, laser-induced shock waves have been used in microstructural material characterization to study nucleation, propagation, coalescence, and dislocation mobility and annihilation [26,27]. For example, Youssef et al. and Colorado et al. demonstrated the effect of ultrahigh strain rate laser-generated stress waves on copper nano-pillars and nanowires under compression and bending, respectively [26,27]. Overall, the laser-induced shock wave technique is unique in four aspects: 1) the depth of the heat-affected zone is limited to only a few micrometers away from the energy absorbent layer; 2) the ultrahigh strain rate stress wave inherits the temporal characteristics of the nanoseconds duration of the laser pulse, that is, the time for creep or for post loading annealing to take place is negligible; 3) the induced strains due to the propagating stress waves is small, which is generally limited to elastic strain regime; and 4) LSW is a contact-free optical loading setup enabling the establishment of the proposed de novo experimental setup to simultaneously load and characterize the sample.

In the area of polymer spectroscopy, the near- and mid-infrared frequency bands are the principal frequency ranges, where the absorption peaks mainly arise from highly localized intramolecular deformation such as hindered rotation or stretching oscillation of covalent bonds [28,29]. However, in the far-infrared (i.e., terahertz regime from ~100 GHz to ~10 THz), the electromagnetic waves interact with collective motions of large molecules such as inter- and intramolecular vibrations of the polymer chains, which makes spectroscopy techniques within this frequency range prime for studying the properties of polymers. THz time-domain spectroscopy (THz-TDS) offer several advantages over conventional far-infrared spectroscopic techniques. First, the signal-to-noise ratio for frequencies below 3 THz is higher than with most conventional techniques [30]. Second, the detectors operate at room temperature [30]. Third, it allows for the simultaneous measurements of the complex refractive index ($\bar{n} = n + ik$, where n is the phase velocity and k is the extinction coefficient), and the thickness of the sample [31]. Fourth, the sample thickness for the THz TDS temperature scans is sufficient to characterize a bulk material; hence, surface phenomena like the depression of T_g for thin polymer layers can be neglected [32]. Fifth, many polymers are transparent to the THz wave facilitating in-situ interrogation. Finally, the contact-free measurement enables the quantification of the material parameters directly even at cryogenic temperatures (especially important herein since impact mitigating polymer such as polyurea have sub-zero T_g) without requiring correction or extrapolation for considering the thermal expansion of the sample. In all, THz-TDS not only clearly outperforms classical techniques but also allows for easy integration with dynamic loading mechanism.

In the first chapter, THz-TDS was used to investigate the residual effect of thermally and mechanically loaded polyurea. The temporal characteristics of the signals were used to extract the optical properties as a function of sample thickness and loading conditions. The mechanically loaded samples showed detectable residual effect whereas it was nearly negligible in thermally loaded polyurea. In general, terahertz-based spectroscopy was shown to be a promising tool for in situ and in operando investigations of field-dependent polymer responses. The second chapter introduces preliminary results of a novel technique that in situ probe the mechanical properties of polymers using terahertz waves. A dielectric elastomer actuator (DEA) structure was used as the mechanical loading mechanism. Finite element analysis is used to model and simulate the DEA to quantify the induced stresses at the observation site, where the electrode configuration was specifically designed for the transmission of terahertz waves without any obstruction of the observation site. The results provided evidence into the interrelationship between the conformational changes in polymers and the applied mechanical stress. Chapter 3 marks a multiscale characterization approach of the intrinsic mechanical attributes of polymers. Here, a LSW experimental technique was used to submit the samples to a strain rate exceeding 10^6 s^{-1} at low strains (<<1%) and investigate the mechanical response, and terahertz-based spectroscopy was incorporated terahertz to detect and report any molecular conformational changes. Additionally, atomic force microscopy (AFM) and scanning electron microscopy (SEM) techniques were used to elucidate changes in the microscale properties, topography, and morphology. Remarkably, failure modes not previously associated with laser spallation technique have been documented. The spectral changes found in the THz regime between the pre- and post-loaded samples substantiated the validity of terahertz spectroscopy in uncovering the underlying mechanism associated with the impact mitigating properties of dynamically loaded polyurea. In the 4th chapter a computational model is employed to elucidate various phenomena associated with the generation, propagation, and interaction of shock waves in viscoelastic material. The results focused on the regions at the leading and trailing edges of the shock wavefront. Generally, the wavefront interacted with the accompanying and reflected waves, resulting in compromising the purity of the sought-after loading condition. Therefore, the resulting simulated response can be used to improve analysis of experimental data and quantify the deformation and failure mechanisms of polymers subjected to hypervelocity impacts. Chapter 5 is focused on using in-situ light-matter interactions to reveal the microstructural mobility by temporally exploiting molecular processes during creep response. Digital image correlation (DIC) revealed development of strain striations and mechanisms responsible for the hard and soft domain mobilities. Terahertz spectral analyses demonstrated the contributions of hard segments interchain hydrogen bonding while the domain mobility was examined using experimental and computational light scattering approaches. The latter uncovered dynamic scattering and elucidated the change in the complex refractive index of the to the different optical properties in soft and hard segments. Our study paved way for quantitative measurements of molecular mobility of polymer during mechanical loading and sheds light on the origin of the shock tolerance in some elastomers with segmental microstructure. Finally, the last chapter summarizes the future work following the contributions of this research.

References

1. Miller, P. High Strain-Rate Material Behavior by Short Pulse Laser-Generated Stress Waves. (2014).

2. Ramesh, K. T. High Rates and Impact Experiments. in *Springer Handbook of Experimental Solid Mechanics* 929–960 (Springer US, 2008). doi:10.1007/978-0-387-30877-7_33.

3. Field, J., Walley, S., Proud, W. & Goldrein, H. Review of experimental techniques for high rate deformation and shock studies. *Int. J.* (2004).

4. Taylor, G. The use of flat-ended projectiles for determining dynamic yield stress. I. Theoretical considerations. *Proc. R. Soc.* (1948).

5. Zhao, J., Knauss, W. G. & Ravichandran, G. Applicability of the time – temperature superposition principle in modeling dynamic response of a polyurea. *Mech. Time Depend. Mater.* **11**, 289–308 (2008).

6. Shim, J. & Mohr, D. Using split Hopkinson pressure bars to perform large strain compression tests on polyurea at low, intermediate and high strain rates. *Int. J. Impact Eng.* **36**, 1116–1127 (2009).

7. Hopkinson, B. The effects of momentary stresses in metals. *Proc. R. Soc. London* (1904).

8. Jiao, T., Clifton, R. J. & Grunschel, S. E. High strain rate response of an elastomer. *AIP Conf Proc* **845 II**, 809–812 (2006).

9. Gupta, V., Argon, A. S., Parks, D. M. & Cornie, J. A. Measurement of interface strength by a laser spallation technique. *J. Mech. Phys. Solids* **40**, 141–180 (1992).

10. Gupta, V., Yuan, J. & Pronin, A. Nanosecond rise-time laser-produced stress pulses with no asymptotic decay. *Rev. Sci. Instrum.* (1993).

11. Pronin, A. & Gupta, V. Measurement of thin film interface toughness by using laser-generated stress pulses. *J. Mech. Phys. Solids* (1998).

12. Gupta, V., Yuan, J. & Pronin, A. Recent developments in the laser spallation technique to measure the interface strength and its relationship to interface toughness with applications

to metal/ceramic,. *J. Adhes. Sci.* (1994).

13. Wang, J., Weaver, R. & Sottos, N. A parametric study of laser induced thin film spallation. *Exp. Mech.* (2002).

14. Ragan, C. E. Ultrahigh-pressure shock-wave experiments. *Phys. Rev. A* **21**, 458–463 (1980).

15. Ready, J. F. Effects due to absorption of laser radiation. *J. Appl. Phys.* **36**, 462–468 (1965).

16. Wietzke, S. *et al.* Terahertz time-domain spectroscopy as a tool to monitor the glass transition in polymers. **17**, 19006–19014 (2009).

17. Ready, J. Industrial applications of lasers. in (1997).

18. Ready, J. Mechanism of electron emission produced by a giant-pulse laser. *Phys. Rev.* (1965).

19. Pronin, A. N. N. & Gupta, V. Measurement of thin film interface toughness by using laser-generated stress pulses. *J. Mech. Phys. Solids* **46**, 389–410 (1998).

20. Vossen, J. L. Measurements of Film-Substrate Bond Strength By Laser Spallation. *ASTM Spec. Tech. Publ.* 122–133 (1978) doi:10.1520/stp38629s.

21. Raman, S. N., Ngo, T., Lu, J. & Mendis, P. Experimental investigation on the tensile behavior of polyurea at high strain rates. *Mater. Des.* **50**, 124–129 (2013).

22. Kim, H., Citron, J., Youssef, G., Navarro, A. & Gupta, V. Dynamic fracture energy of polyurea-bonded steel/E-glass composite joints. *Mech. Mater.* **45**, 10–19 (2012).

23. Hu, L. *et al.* Cell adhesion measurement by laser-induced stress waves. *J. Appl. Phys.* **100**, (2006).

24. Miller, P., Hu, L. & Wang, J. Finite element simulation of cell–substrate decohesion by laser-induced stress waves. *J. Mech. Behav. Biomed.* (2010).

25. Youssef, G. *et al.* Inter-wafer bonding strength characterization by laser-induced shock waves Inter-wafer bonding strength characterization by laser-induced shock waves. **094902**,

1–5 (2012).

26. Youssef, G. *et al.* The influence of laser-induced nanosecond rise-time stress waves on the microstructure and surface chemical activity of single crystal Cu nanopillars. *J. Appl. Phys.* **113**, (2013).

27. Colorado, H., Navarro, A. & Prikhodko, S. Ultrahigh strain-rate bending of copper nanopillars with laser-generated shock waves. *J. Appl.* (2013).

28. Wietzke, S. *et al.* Terahertz spectroscopy on polymers : A review of morphological studies. *J. Mol. Struct.* **1006**, 41–51 (2011).

29. Krimm, S. Infrared spectra of high polymers. in *Fortschritte Der Hochpolymeren-Forschung* 51–172 (Springer-Verlag, 1960). doi:10.1007/BFb0050351.

30. Han, P. Y. *et al.* A direct comparison between terahertz time-domain spectroscopy and far-infrared Fourier transform spectroscopy. *J. Appl. Phys.* **89**, 2357–2359 (2001).

31. Scheller, M., Jansen, C. & Koch, M. Analyzing sub-100- l m samples with transmission terahertz time domain spectroscopy. *Opt. Commun.* **282**, 1304–1306 (2009).

32. Forrest, J., Dalnoki-Veress, K., Stevens, J. & Dutcher, J. Effect of free surfaces on the glass transition temperature of thin polymer films. *Phys. Rev. Lett.* (1996).

CHAPTER 1

Ex-situ Spectroscopic Characterization of Residual Effects of Thermomechanical Loading on Polyurea

Nha Uyen Huynh and George Youssef*

Experimental Mechanics Laboratory, Mechanical Engineering Department, San Diego State University, 5500 Campanile Drive, San Diego, CA 92182-1323, USA

Abstract

The residual effect of thermally and mechanically loaded polyurea samples was investigated in this study using terahertz time-domain spectroscopy (THz-TDS). Samples of different thicknesses were submerged in liquid nitrogen and reached cryogenic isothermal conditions while another set of samples were extracted from quasi-statically loaded strips. All samples were interrogated using THz-TDS since terahertz waves exhibit non-ionizing, nondestructive interactions with polymers. The time-domain terahertz signals were used to extract the optical and electrical properties as a function of sample thickness and loading conditions. The residual effect was prominent in the mechanically loaded samples compared to a nearly negligible presence in thermally loaded polyurea. On average, the results of the thermally loaded samples were subtle when compared to the virgin samples, whereas samples that were mechanically stretched showed a considerable difference in the characteristics of the time-domain signals. For example, the peak amplitude in the time-domain signal of the stretched thick sample showed a 9% difference from that of the virgin sample, whereas the thermally loaded sample saw only a 4.9% difference. Spectral analysis reported the frequency-dependent, complex refractive index of virgin and loaded polyurea as a function of thickness and spectral peaks associated with fundamental vibrational modes of the polyurea structure. The disappearance of three spectral peaks, 0.56 THz, 0.76 THz, and 0.95 THz elucidated the residual effect of the mechanically loaded samples. In general, terahertz spectroscopy was shown to be a promising tool for future *in situ* and *in operando* investigations of field-dependent polymer responses.

Keywords: residual effects, terahertz spectroscopy, polyurea elastomer, Thermomechanical loading, Polymer Response

***Corresponding Author: gyoussef@sdsu.edu**

1.1 Introduction

Despite more than two decades of persistent research efforts involving several prominent researchers, polyurea elastomers still attract significant analytical, computational, and experimental investigations spanning over a wide range of length and time scales [1]. Polyurea is an elastomeric material with exceptional physical properties, including high stretchability, high tear and tensile strength, and moisture and chemical resistance [2,3]. Polyurea has been actively investigated for numerous applications [1,4–6], of which impact mitigation in a variety of environmental conditions has been a prime focus. For example, polyurea adhesive was found to increase the fracture toughness of composite marine joint by 1.3 fold compared to Hysol epoxy [7]. A polyurea monolithic coating layer has been shown to improve the blast resistance of armor steel and aluminum plates [8,9], composite sandwich panels, joints and structures [3,10], and sports gears [11,12]. In an attempt to further enhance the impact performance of polyurea, several reports investigated the mechanical properties of reinforced polyurea matrix composites using carbon nanotubes [13,14], fly ash [15], and polyurea microspheres [16–18], reporting various degrees of improvement of the local deformation resistance but with no appreciable overall enhancements. In general, the performance of polyurea in impact scenarios is attributed to (1) the strain rate sensitivity [19–22] and (2) the microstructure composing of interpenetrating hard and soft segments [23–27]. Recently, Shahi et al. performed an exhaustive experimental investigation on the role of the hard and soft segments dispersion and of the chain length on the thermomechanical properties of polyurea with different compositions of the constituents [28]. They reported that the composition plays a role in the high strain response of polyurea by altering the post-yield hardening behavior. Alternatively, Gupta et al. and Youssef et al. were successful in foaming polyurea after recognizing the positive effect of adding a thin layer of polyurea to several sports gears [29,30]. Polyurea foams were effective in mitigating biomechanical impacts due to low-velocity loading [17,30–33]. In all, polyurea remains a fascinating material from the basic and applied research perspectives.

The mechanical behavior of polyurea has been heavily investigated in response to different environmental and loading conditions experimentally, including a wide range of strain rates (~10^{-3} s^{-1} to 10^{7} s^{-1}) [4,19,20], temperatures (-100°C – 50°C) [6,34,35], salinity [3,6], and ultraviolet radiation [6,36–39]. As the tensile strain rate increases, polyurea exhibits phase transition from the rubbery to the glassy regime passing through the leathery region, depending on the testing rate, where the strain-to-failure decreased while the yield stress and ultimate failure stress increased [20–22,40,41]. Our group examined the effect of extended exposure to ultraviolet radiation on the elastic, hyperelastic, and viscoelastic properties of polyurea [36–39]. It was found that the hyperelasticity of polyurea remained unchanged, while the ultraviolet radiation increased the stiffness and resulted in the formation of surface microcracks extending 45 µm into the samples after 15 weeks of continuous exposure [39]. Che et al. investigated the response of polyurea in a marine environment, including ultraviolet radiation, for up to 150 days [42]. Che and collaborators attributed the aging response of polyurea to an increase in phase separation and chain scission of N-H, C=O, and C-O-C, and the hydrogen-bonded urea carbonyl group [42]. More recently, Mforsoh et al. also examined the compressive response of polyurea after exposure to aggressive marine environments, including salinity, temperature, and ultraviolet radiation [6]. They found that the strain energy decreased after extended exposure to saline water but increased after ultraviolet radiation. However, despite extensive research on the mechanical response of polyurea under different loading conditions, there is a gap in the knowledge about the residual effect of mechanical and thermal loadings on polyurea microstructure, potentially compromising its long-term reliability in repeated loading scenarios. This knowledge gap is the primary motivation of the research leading to this paper.

The post-loading microstructure of polyurea has been examined using X-ray scattering and Brillouin scattering spectroscopy [43,44]. The X-ray studies performed on polyurea-metal bilayer plates elucidated the strain hardening response of polyurea and its contribution to the overall energy dissipation of the composite structure [44], which was attributed to the sample preparation process. The hard segments failed under the influence of the high stress associated with high strain testing, hence increasing strain hardening. On the other hand, Brillouin scattering spectroscopy was used to extract the longitudinal and shear sound velocities of polyurea at pressures up to 13.5 GPa [43]. Since polyurea vitrifies under extreme strain hardening, conventional mechanical testing and characterization techniques cannot capture the subtle changes in material properties upon solidification. The material properties of polyurea under high pressure, high strain rate conditions were then determined by correcting the high-frequency Brillouin data to account for viscoelastic effects, resulting in the extraction of better estimates of the change in the density from the Brillouin sound velocity data [43]. Another promising spectroscopy technique in the area of *ex-situ* or *in situ* characterization of loaded-polymers is terahertz time-domain spectroscopy since it is suitable for noncontact, noninvasive, and non-ionizing interrogation of polymers. This research examined the optical and mechanical response of elastomeric material under mechanical stresses using a novel *in situ* terahertz time-domain spectroscopic technique [45]. The resulting time-domain signals at different applied stresses were used to elucidate subtle changes in the elastomer microstructure by investigating the temporal characteristics of the terahertz waves interacting with the samples. In other words, terahertz time-domain spectroscopy was used to provide physical evidence of mechanically stress-induced conformational changes of polymers, signified by changes in the complex index of refraction. While being a macroscopic property, the latter can be used to reveal microscopic properties such as the change in the polarizability using Lorentz-Lorenz and Clausius-Mossotti relations.

This research aims to elucidate of the residual effects of thermal and mechanical loading on polyurea elastomers after submersion in cryogenic and quasi-static loading conditions, respectively. Cast polyurea disks with two different thicknesses were first extracted from two cast sheets and fully submerged in liquid nitrogen (LN_2) to reach isothermal conditions for up to 3 h. The additional specimens were extracted from the same sheets for quasi-static tensile testing at a strain rate of 0.01 s^{-1} up to 100% strain using a ±1 kN load frame (Instron 5843). Therefore, one set of samples with a thickness of 1661±25 μm was separately tested under uniaxial tension and cryogenic isothermal condition. Another set of polyurea samples with thickness of 497±65 μm was also tested under the same testing conditions. The choice of this range of thickness was based on *a priori* work, showing thin film polyurea with <2mm in thickness to be effective in mitigating impacts in several applications [9,29]. Moreover, the thickness range was selected based on the specification of the terahertz spectrometer developed in our laboratory. The tested samples (thermally or mechanically) were then allowed to rest in ambient conditions for four hours. The optical properties of the samples were assessed using terahertz time-domain spectroscopy (THz-TDS) operating in the transmission mode, reporting the complex index of refraction as a function of frequency ranging from 0.4 to 1.3 THz.

1.2 Experimental Protocol

Polyurea sheets with different thicknesses were manufactured using a slab-molded technique, where the chemical constituents, diisocyanate (DOW Industrial, Isonate® 143L), and oligomeric diamine (AirProduct Inc., Versalink® P1000), were mechanically mixed with a 1:4 weight ratio, respectively. The sheets were first cured in ambient conditions for 24 h, and then in a vacuum oven at 80°C for an additional 24 h. The importance of the full curing cycle on the overall performance of the polyurea sheet was previously discussed in [46]. The average thickness of one sheet was 1661±25 μm, while the average thickness of the second sheet was 497±65 μm, in what is referred to hereafter as 'thick' and 'thin' samples, respectively. The samples thickness was based on the bandwidth and capabilities of our developed in-house terahertz-wave spectrometer. The notation of 'thin' and 'thick' is therefore descriptors and not categorical. Discs of 25.4 mm diameter were die cut using a hydraulic press from an area with consistent thickness from each sheet. Another disc-shaped specimen from each sheet was neither mechanically nor thermally loaded, referred to herein as the virgin samples. Thick and thin polyurea discs were soaked in liquid nitrogen (LN_2) for 180 min and 60 min, respectively, to where the discs reached isothermal conditions. The long soaking time was chosen to ensure thermal equilibrium even though the time required to reach isothermal condition was calculated to be only a few seconds based on the submersion condition and the thermal conductivity of polyurea (taken to be 0.16 $W \cdot mK^{-1}$) reported by Shahi et al. using one-dimensional heat conduction [28]. Notably, this thermal loading condition resulted in a thermal strain (ε_{th}) of 4.38% using a thermal expansion coefficient (α) of $2x10^{-4}$ K^{-1} based on $\varepsilon_{th} = \alpha \Delta T$, the ΔT is the difference between room temperature and the LN_2 bath [34]. Upon removal from the LN_2 bath, the samples were left to naturally reach ambient conditions for 240 min before being investigated using THz-TDS.

Polyurea strips with dimensions of 10.16 cm long x 2.54 cm wide were cut out from the same sheets for mechanical tensile loading. The 10.16 cm x 2.54 cm samples were loaded using an Instron 5843 load frame with a ±1 kN load cell. The strain was measured using an Instron 2603-84 large strain extensometer, where the samples were loaded in tension to a maximum strain of 100%. The corresponding maximum forces applied to the thick sample and thin sample were 258

N and 84 N. Upon removal from the load frame, three discs with a 25.4 mm diameter were removed from the loaded region of the stretched polyurea strips, as seen in Figure 1.1a. The straight notch in each sample (shown in Figure 1.1a-b) was introduced to ensure the direction of loading coincided with the direction of terahertz propagation during the spectroscopic investigation. The virgin, thermally, and mechanically loaded discs were fitted into mounts with an inner diameter of 25.4 mm to eliminate any tilt or misalignment during the measurement acquisition using THz-TDS. Each of the three plugs extracted from each stretched sample was interrogated with terahertz waves. For the thermally loaded sample, a polyurea disc of each thickness was soaked in the LN_2 bath, but three terahertz signals were collected from each sample. The specimen discs were lightly clamped between the surface of the mount on one side and a retaining ring on the other. This mounting method facilitated the handling and placement of each specimen during THz testing, where the focal point of the terahertz beam was guided to the center of the specimen, avoiding any obstruction. A schematic of the sample situated in the terahertz time-domain spectroscopy can be seen in Figure 1.2.

In our developed in-house THz-TDS setup, a laser source of pulsed femtosecond beam (Menlo Systems, ELMO 780 HP) is split into two different paths. The laser beam from the first path was focused on the active area of a photoconductive antenna transmitter (PCA,TeTechS, T-Era-100A-800) to generate terahertz waves. Once the THz waves propagated through the sample, located within the THz path, and collimated and focused onto a detector using a pair of off-axis mirrors, the signal was measured using a PCA receiver (TeTechS, T-Era-20D40P-800). At the same instant, the delayed laser beam from the second path activated the receiving photoconductive antenna converting the terahertz waves into a measurable electrical signal, which was recorded using a lock-in amplifier (Stanford Research Systems, SR830) and built in-house data acquisition system. The DAQ system is able to control the speed and record the travel distance of the delay leg while acquiring the data from the lock-in amplifier. It is worth noting that the output signal of the receiving THz antenna was passed through a low noise amplifier (TeTechS, Low Noise Amplifier) before being processed by the lock-in. The collected time-domain data was transformed into the frequency-domain using a fast Fourier transform (FFT). The frequency-domain data was used to calculate the real part of the refractive index and absorption coefficient using Eqn. 1.1 and 1.2, respectively.

$$n(f) = 1 + \frac{c[\varphi_{sample}(f) - \varphi_{reference}(f)]}{2\pi f d} \tag{1.1}$$

$$\alpha(f) = -\frac{2}{d} ln \frac{[n(f)+1]^2 |\hat{E}_{sample}(f)|}{[4n(f)]\, |\hat{E}_{reference}(f)|} \tag{1.2}$$

where, $\boldsymbol{n}$ and $\boldsymbol{\alpha}$ are the refractive index and absorption coefficient of the sample, respectively, $\boldsymbol{d}$ is the measured thickness of the sample and c is the speed of light in vacuum. $|\hat{E}_{reference}|$ is the complex amplitude of the reference while $|\hat{E}_{sample}|$ is the complex amplitude of the sample. $\varphi_{reference}$ and φ_{sample} are the phase of the reference and sample spectra, respectively. In here, the reference measurement refers to the terahertz signal obtained in air, i.e., a sample-free condition where the terahertz beam path is uninterrupted and unobstructed.

1.3 Results and Discussion

Figure 1.3a shows the THz time-domain signals of thermally and mechanically loaded samples compared to their virgin counterparts and the sample-free reference signals (collected when the samples were not present in the THz beam path). The primary wave characteristics of interest are summarized in Table 1.1, including the average thickness (post-loading thickness is reported for thermal and mechanical samples, which were mechanically measured), the peak amplitude, and the delay time. The calculated optical and electrical properties are also included in

Table 1.1. The notable reduction in amplitude and temporal shift in all the signals resulted from the convoluted effect of the thickness and the change in the index of refraction. For example, when comparing the reference (solid magenta line) with a thin (solid black line) and thick (dotted black line) virgin signal, the peaks appeared at 39.40 ps, 40.32 ps, and 43.13 ps, respectively, marking the temporal delay in the arrival of t_{thin} = 0.9167 ps and t_{thick} = 3.7333 ps. The average thickness of the thin samples was 476 µm, while the thick samples were 1686 µm, representing nearly a threefold increase ($d_{thin}/d_{thick} \approx$ 0.28), which is commensurable with the ratio of the time delay ($t_{thin}/t_{thick} \approx 0.25$). The disparity between these ratios signifies the contribution of the thickness-dependent change in the index of refraction. The real part of the refractive index (n) is related to the delay time (t), the thickness (d), and the speed of light (c) in vacuum, where $n = 1 + {}^{ct}/_{d}$. Therefore, the real refractive index of polyurea is estimated to be 1.65 and 1.52 for thick and thin samples, respectively, using the attributes of the time-domain signals in Table 1.1. Similarly, the rest of the temporal characteristics are used to estimate the imaginary part of the refractive index (a measure of the absorption coefficient), where $\kappa = \ln\left(\frac{2}{(n+1)}\frac{A_R}{A_S}\right)$ is based on the amplitude of the sample (A_S) and the reference (A_R) signals. Here, κ was defined based on the logarithmic decrement concept while considering the Fresnel coefficient in the case of total transmission. The imaginary part of the index of refraction for thin and thick polyurea are 0.15 and 0.45, respectively, since the amplitude of the time-domain signals were found to be 0.445 V and 0.309 V while the amplitude of the reference was 0.634 V.

In terms of the complex refractive index, the optical properties are then used to compute the dielectric function (ε) of polyurea since $\varepsilon = (n + i\kappa)^2$. The dielectric constant ($|\varepsilon|$) of thick and thin virgin polyurea samples was found to be 2.93 and 2.34, respectively, which is in reasonable agreement with the constants measured using the electrical method and reported to range between 3.5-4.2, depending on the preparation method (including the stoichiometric ratio and the type of diamine and isocyanate), temperature, and frequency [47,48]. In short, the difference in the values of the dielectric constant reported here using the optical properties, and that reported *a priori* using the electrical method is thought to be due to (1) the sample thickness used in the experiments and (2) the sample preparation approaches. Here, the samples were extracted from slab-molded polyurea sheets, while the samples used in the electrical testing experiment were prepared via vapor deposition polymerization or vacuum thermal vapor deposition techniques [47,49]. It is worth noting that the thickness plays a significant role in the final conformational arrangements within the sample, where an ultrathin configuration may be energetically favorable for a higher degree of crystallization [47,49]. The manufacturing process may also affect the conformations given factors such as the substrate clamping effect and confinement, resulting in mechanical anisotropy [50,51].

The strain percentage due to thermal loading by supercooling the sample in an LN_2 bath and then bringing it back to ambient temperature was estimated to be 4.38%, based on the difference in temperature (ΔT) and the thermal expansion coefficient (α), i.e., the strain is due to thermal effects. This low strain level is within the linear elastic region of the mechanical response of polyurea, which can be confirmed by projecting this low strain percentage on the engineering stress-strain curve shown in Figure 3b. The loading is thought to be completely reversible; hence, the residual stress and strain effects can be considered minimal in the case of thermal loading. It is worth noting that concurrently observing the molecular transitions of polyurea during cooling is a focus of future research and outside the scope of this investigation, where an accurate determination of the glass transition can be identified [52]. The negligible residual effect was also captured in the THz time-domain signal by comparing the data of the virgin and thermally loaded samples. For the thick samples, the peak amplitude and time delay changed by 4.9% and 0.01%, respectively, indicating the reversibility of the deformation. Similarly, the THz signals of the virgin and supercooled thin polyurea samples were also comparable. The peak amplitude of the thin samples was 0.476 V and 0.466 V for the virgin and thermally loaded samples with a time delay of 0.83 ps and 0.80 ps, respectively. In all, and regardless of the sample thickness, the thermal loading had a negligible residual effect, signifying the utility of polyurea over a broad range of temperatures [1].

In the case of mechanically loading the polyurea samples up to 100% strain, analysis of the THz time-domain signals reported a notable difference, indicating that the residual effect is present while signifying irreversibility. It is worth noting that the samples were characterized using THz-TDS, on average, two hours post-loading. There are three noteworthy observations, following a close examination of the time-domain signals in Figure 1.3a and the summary of the major attributes in Table 1.1. First, the thickness has exhibited a reduction of 18.8% and 11.5% for thick and thin samples, respectively. The remnant set in the thickness is attributed to the relatively short duration between testing and spectroscopic characterization, not providing ample time for full recovery based on the viscoelastic properties of polyurea. The mechanical loading at 100% strain corresponds to the engineering stress of 5.5 MPa, which is nearly twofold higher than the reported yield stress of the material [6]. Second, the amplitude of the terahertz time-domain signal increased, regardless of the thickness of the tested samples. On average, the amplitude of the thin samples increased by 14.6% and by 9% for the thick samples, compared with the signal amplitude of the virgin samples. The amplitude growth was accompanied by variations in the time delay. As discussed above, the amplitude and time delay changes are generally associated with the complex refractive index changes. Correspondingly, the latter was calculated to be $1.67+i0.39$ for the stretched thick sample and 1.66-i0.05 for the thin sample, which is greater than the complex index of refraction for the virgin samples reported above. It is then thought that the post-loading index represents a change in the molecular structure that resulted in less attenuation and dispersion of the THz electromagnetic waves as it propagates throughout the samples, which is realized by the reduction in the extinction coefficient (κ) for the stretched polyurea samples.

The essence of spectroscopic investigations is based on the existence of a set of molecular vibrational modes due to the interaction between the propagating electromagnetic waves and the material. The oscillations of the different bonds within the materials signify the final utility of the time-domain data in terms of the quality factor (Q), which is defined here as the ratio between the energy of the reference signal (i.e., signal collected without sample) to the energy of the sample signal (Figure 1.4a). The former represents the stored energy in the terahertz pulse, while the latter accounts for the dissipated energy due to the damped oscillations of the vibrating bonds observed by the propagating terahertz pulse as it interacts with the sample. The calculations of Q is shown schematically in Figure 1.4b and Eqn. 1.3 by considering the total area under the reference THz pulse ($\int_{t_1^r}^{t_2^r} E_r(t)dt$) and sample THz pulse ($\int_{t_1^s}^{t_2^s} E_s(t)dt$).

$$Q = 2\pi \frac{\int_{t_1^r}^{t_2^r} E_r(t)dt}{\int_{t_1^s}^{t_2^s} E_s(t)dt} \tag{1.3}$$

Figure 1.4c shows the quality factor results of thick and thin samples for the virgin, stretched, and supercooled samples, which succinctly summarizes all the conclusions elucidated via the consideration of the optical and electrical properties thus far. It is worth noting that the quality factor was calculated for each thickness and testing condition separately by comparing the signal collected from that sample to its reference data. Three overarching conclusions of time-domain data are concisely encoded in the Q values. First, the thickness plays a measurable role due to the attenuation and dispersion of the waves within the material, where the difference in Q was found to be 33% when comparing thin and thick virgin samples. The disproportionality of Q and thickness is attributed to the changes in the complex index of refraction, as discussed before. Second, mechanical loading tends to increase bond oscillation dampening since the Q values for the loaded thick and thin samples were smaller than their virgin counterparts by 11% and 44%, respectively. Third, and on the contrary, supercooling the thick sample resulted in a significant decrease in dampening, manifested in an increase of 10% and 23% in Q values comparative to virgin and mechanically loaded samples. The submersion in cryogenic temperatures is thought to freeze the chains, increasing the bond stiffness while reducing energy dissipation due to dampening. Future research can emphasize the interrelationship between the decrease in temperature and bond stiffness and recrystallization mechanisms using complementary methods such as X-ray diffraction, Raman Spectroscopy, and molecular dynamic simulations.

While analysis of the THz time-domain signals revealed important preliminary attributes of the samples, frequency-domain analysis is typically applied to extract the complex refractive index as a function of frequency spanning over the bandwidth. The bandwidth is selected based on the power spectral response of the THz antennas as well as the stability of the frequency transformation algorithm. Here, the frequency range for the thick and thin samples were 0.4 – 1.3 THz and 0.7 – 1.3 THz, respectively. The range was truncated during the material extraction process to ensure algorithm stability and robustness. Figure 1.5a shows the real part of the refractive index while Figure 1.5b is a plot of the absorption coefficient of the virgin, thermally, and mechanically loaded samples in two ranges of thicknesses. As concluded from the time-domain analysis, thermal loading results in an indifferent real part of the index compared to the virgin, where the difference is less than 0.2%, on average over the entire frequency range, for both thick and thin samples. Regardless of the testing conditions, the real part of the refractive index monotonically decreases with increasing frequency, while the absorption coefficient increases as a function of frequency. The frequency dependence of the refractive index is consistent with the description given in Eqn. 1.1 and 1.2, respectively, since the thickness was kept constant throughout the characterization using THz-TDS. On average, the refractive index of the thick and thin polyurea samples is relatively similar, where the latter is merely 0.02% greater than the former. In other words, the small difference between the index of refraction of the thick and thin polyurea samples indicates that they are thickness-independent in this scenario. The small variance in the index components values for a different regiment of samples at a given frequency is attributed to the threefold difference in thickness, as discussed before. Generally, the dispersion and attenuation of waves in a media are strongly coupled to the thickness through the delay time of arrival, commonly captured by the quality factor, as discussed above. The values of the index of refraction calculated from the frequency-domain analysis, Figure 1.5, are in good agreement with the time-domain analysis discussed above.

The virgin thick polyurea samples reported spectral peaks at 0.56, 0.76, 0.95, 1.10, 1.17, and 1.21 THz, while the thin samples only showed peaks at the last three values. Zhao et al. investigated the intermolecular vibrational modes in crystalline urea in the terahertz regime and, within the same range as the study herein, observed three absorption peaks at 0.69, 1.08, and 1.27 THz [53]. Figure 1.6 compares the chemical structure between crystalline urea and urea-linkage in the aromatic polyurea investigated in this study. The latter is connected to a larger structure via aromatic benzene rings instead of hydrogen bonds, which may account for some of the spectral peaks are seen in polyurea but not in the crystalline urea. Nonetheless, the good agreement of the 0.76, 1.10, and 1.21 THz absorption bands to the corresponding bands seen in [53] supports that those features seen in the polyurea refractive and absorbance spectra are ascribed to the urea-linkages of the monomer chain. It is important to note that the 0.56, 0.76, and 0.95 peaks in the spectra of the thick virgin and supercooled samples are no longer apparent in the stretched sample. It is speculated that the molecular vibrational modes at the abovementioned frequencies are no longer visible due to the damping, excitation, or restriction of motions of the bonds as a result of the physical strain induced on the polyurea. Based on cluster calculations and the potential energy distributions analysis, the peaks at 0.69 and 1.08 THz are attributed to the bending and twisting of bonded urea crystals, respectively [53]. It is reflected that the elimination of the 0.76 THz feature can be attributed to the limitation of the bending mode of the urea linkages, thus, making that vibrational mode invisible in the stretched polyurea spectrum.

1.4 Conclusion

Polyurea has and continues to capture the scientific interest, sparking computational, analytical, and experimental research to elucidate the property-structure-performance relationship. Polyurea samples with different thicknesses were mechanically or thermally loaded and interrogated with terahertz radiation to explicate the residual effect of the high-impact mitigating polymer after loading. The characteristics of the resulting averaged time-domain signals of six samples were used to calculate the change of optical and electrical properties of loaded and unloaded polyurea as a function of loading conditions and sample thickness. Such characteristics include the shift in time delay and change in amplitude of the main peak signal, which can be used to estimate the real refractive index and absorption coefficient of the investigated material. The quality factor was also used to relate the changes in the properties with loading conditions collectively. The dielectric constant extracted from the terahertz time-domain analysis was found to be in reasonable agreement with previous research [47,48]. To increase the utility of the collected data, the frequency spectra of the time-domain signals were used to calculate the frequency-dependent refractive index, reporting several spectra peaks associated with the fundamental vibrational modes of the investigated polyurea structure. These spectral peaks were in good agreement with previous investigations [53] and pointed toward the molecular structure change after mechanical loading. The latter was shown as the disappearance of the low-terahertz spectral peaks after large-strain mechanical loading. In all, the results reported here provide additional insights into the residual stress on the behavior of polymers while paving the way for more scientific investigations using terahertz waves for *in situ* and *in operando* testing.

Acknowledgement

Chapter 1, in full, is a reprint of the material as it appears in Journal of Engineering Materials and Technology 2021. Huynh, Nha Uyen; Youssef, George, ASME, 2021. The dissertation author was the primary investigator and author of this paper.

References

1. Barsoum, R. G. *Elastomeric Polymers With High Rate Sensitivity: Applications in Blast, Shockwave, and Penetration Mechanics*. (Elsevier Inc., 2015). doi:10.1016/B978-0-323-35400-4/00011-8.

2. Youssef, G. & Gupta, V. Resonance in Polyurea-Based Multilayer Structures Subjected to Laser-Generated Stress Waves. *Exp. Mech.* **53**, 145–154 (2013).

3. Jain, A., Youssef, G. & Gupta, V. Dynamic tensile strength of polyurea-bonded steel/E-glass composite joints. *J. Adhes. Sci. Technol.* **27**, 403–412 (2013).

4. Youssef, G. & Gupta, V. Dynamic tensile strength of polyurea. *J. Mater. Res.* **27**, 494–499 (2011).

5. Jiao, T., Clifton, R. J. & Grunschel, S. E. Pressure-sensitivity and tensile strength of an elastomer at high strain rates. in *AIP Conference Proceedings* vol. 955 707–710 (2007).

6. Neba Mforsoh, I., LeBlanc, J. & Shukla, A. Constitutive compressive behavior of polyurea with exposure to aggressive marine environments. *Polym. Test.* **85**, 106450 (2020).

7. Jain, A. & Gupta, V. Construction and characterization of stainless steel/polyurea/E-glass composite joints. *Mech. Mater.* **46**, 16–22 (2012).

8. Mohotti, D., Ngo, T., Mendis, P. & Raman, S. N. Polyurea coated composite aluminium plates subjected to high velocity projectile impact. *Mater. Des.* **52**, 1–16 (2013).

9. Amini, M. R., Simon, J. & Nemat-Nasser, S. Numerical modeling of effect of polyurea on response of steel plates to impulsive loads in direct pressure-pulse experiments. *Mech. Mater.* **42**, 615–627 (2010).

10. Gardner, N., Wang, E., Kumar, P. & Shukla, A. Blast Mitigation in a Sandwich Composite Using Graded Core and Polyurea Interlayer. *Exp. Mech.* **52**, 119–133 (2012).

11. Barsoum, R. G. S. & Dudt, P. J. The fascinating behaviors of ordinary materials under dynamic conditions. *Ammtiac Q* **4**, 11–14 (2010).

12. Ramirez, B. J. & Gupta, V. Evaluation of novel temperature-stable viscoelastic polyurea foams as helmet liner materials. *Mater. Des.* **137**, 298–304 (2018).

13. Gao, C. *et al.* Polyurea-functionalized multiwalled carbon nanotubes: Synthesis, morphology, and Raman spectroscopy. *J. Phys. Chem. B* **109**, 11925–11932 (2005).

14. Kirmani, M. H., Arias-Monje, P. J. & Kumar, S. High Interfacial Shear Strain in Polyurea-Carbon Nanotube Composite Sheets. *ACS Appl. Nano Mater.* **2**, 6849–6857 (2019).

15. Qiao, J., Schaaf, K., Amirkhizi, A. V. & Nemat-Nasser, S. Effect of particle size and volume fraction on tensile properties of fly ash/polyurea composites. *Behav. Mech. Multifunct. Mater. Compos. 2010* **7644**, 76441X (2010).

16. Do, S., Stepp, S. & Youssef, G. Quasi-static and dynamic characterization of polyurea microspheres reinforced polyurea matrix composite. *Mater. Today Commun.* **25**, 101464 (2020).

17. Do, S. *et al.* Partially-Perforated Self-Reinforced Polyurea Foams. *Appl. Sci.* **10**, 5869 (2020).

18. Do, S. Synthesis and Characterization of Polyurea-Polyurea Composite. (Masters Thesis, San Diego State University, 2018).

19. Sarva, S. S., Deschanel, S., Boyce, M. C. & Chen, W. Stress-strain behavior of a polyurea and a polyurethane from low to high strain rates. *Polymer (Guildf).* **48**, 2208–2213 (2007).

20. Roland, C. M., Twigg, J. N., Vu, Y. & Mott, P. H. High strain rate mechanical behavior of polyurea. *Polymer (Guildf).* **48**, 574–578 (2007).

21. Raman, S. N., Ngo, T., Lu, J. & Mendis, P. Experimental investigation on the tensile behavior of polyurea at high strain rates. *Mater. Des.* **50**, 124–129 (2013).

22. Yi, J., Boyce, M. C., Lee, G. F. & Balizer, E. Large deformation rate-dependent stress-strain behavior of polyurea and polyurethanes. *Polymer (Guildf).* **47**, 319–329 (2006).

23. Runt, J., Pangon, A., Castagna, A., He, Y. & Grujicic, M. Phase Separated Microstructure and Structure-Property Relationships of High Strain Rate Elastomeric Polyureas. in *Elastomeric Polymers with High Rate Sensitivity: Applications in Blast, Shockwave, and Penetration Mechanics* 5–16 (Elsevier Inc., 2015). doi:10.1016/B978-0-323-35400-4.00002-7.

24. Grujicic, M. *et al.* Experimental characterization and material-model development for microphase-segregated polyurea: An overview. *J. Mater. Eng. Perform.* **21**, 2–16 (2012).

25. Grujicic, M. *et al.* Multi-length scale modeling and analysis of microstructure evolution and mechanical properties in polyurea. *J. Mater. Sci.* **46**, 1767–1779 (2011).

26. Heyden, S., Ortiz, M. & Fortunelli, A. All-atom molecular dynamics simulations of multiphase segregated polyurea under quasistatic, adiabatic, uniaxial compression. *Polymer (Guildf).* **106**, 100–108 (2016).

27. He, Y., Xie, D. & Zhang, X. The structure, microphase-separated morphology, and property of polyurethanes and polyureas. *J. Mater. Sci.* **49**, 7339–7352 (2014).

28. Shahi, V., Alizadeh, V. & Amirkhizi, A. V. Thermo-mechanical characterization of polyurea variants. *Mech. Time-Dependent Mater.* **24**, 1–25 (2020).

29. Gupta, V., Citron, J. K. & Youssef, G. H. Patent Application Publication Pub. No.: US 2013/0312287 A1. vol. 1 (2013).

30. Youssef, G., Reed, N., Huynh, N. U., Rosenow, B. & Manlulu, K. Experimentally-validated predictions of impact response of polyurea foams using viscoelasticity based on bulk properties. *Mech. Mater.* **148**, (2020).

31. Koohbor, B., Blourchian, A., Uddin, K. Z. & Youssef, G. Characterization of Energy Absorption and Strain Rate Sensitivity of a Novel Elastomeric Polyurea Foam. *Adv. Eng. Mater.* **2000797**, 1–11 (2020).

32. Ramirez, B. J. & Gupta, V. Energy Absorption and Low Velocity Impact Response of Open-Cell Polyurea Foams. *J. Dyn. Behav. Mater.* **5**, 132–142 (2019).

33. Reed, N., Huynh, N. U., Rosenow, B., Manlulu, K. & Youssef, G. Synthesis and characterization of elastomeric polyurea foam. *J. Appl. Polym. Sci.* **48839**, 1–8 (2019).

34. Amirkhizi, A. V., Isaacs, J., McGee, J. & Nemat-Nasser, S. An experimentally-based viscoelastic constitutive model for polyurea, including pressure and temperature effects. *Philos. Mag.* **86**, 5847–5866 (2006).

35. Zhao, J., Knauss, W. G. & Ravichandran, G. Applicability of the time – temperature

superposition principle in modeling dynamic response of a polyurea. *Mech. Time Depend. Mater.* **11**, 289–308 (2008).

36. Whitten, I. & Youssef, G. The effect of ultraviolet radiation on ultrasonic properties of polyurea. *Polym. Degrad. Stab.* **123**, 88–93 (2016).

37. Youssef, G. & Whitten, I. Dynamic properties of ultraviolet-exposed polyurea. *Mech. Time-Dependent Mater.* **21**, 351–363 (2017).

38. Youssef, G., Brinson, J. & Whitten, I. The Effect of Ultraviolet Radiation on the Hyperelastic Behavior of Polyurea. *J. Polym. Environ.* **26**, 183–190 (2018).

39. Shaik, A. M., Huynh, N. U. & Youssef, G. Micromechanical behavior of ultraviolet-exposed polyurea. *Mech. Mater.* **140**, 103244 (2020).

40. Joshi, V. S. & Milby, C. L. High strain rate behavior of polyurea compositions. *AIP Conf. Proc.* **1426**, 167–170 (2012).

41. Shim, J. & Mohr, D. Using split Hopkinson pressure bars to perform large strain compression tests on polyurea at low, intermediate and high strain rates. *Int. J. Impact Eng.* **36**, 1116–1127 (2009).

42. Che, K., Lyu, P., Wan, F. & Ma, M. Investigations on aging behavior and mechanism of polyurea coating in marine atmosphere. *Materials (Basel).* **12**, (2019).

43. Ransom, T. C., Ahart, M., Hemley, R. J. & Roland, C. M. Acoustic properties and density of polyurea at pressure up to 13.5 GPa through Brillouin scattering spectroscopy. *J. Appl. Phys.* **123**, (2018).

44. Balizer, E., Fedderly, J., Lee, G., Bartyczak, S. & Mock, W. Investigation of microstructural changes in impacted polyurea coatings using small angle X-ray scattering (SAXS). *Powder Diffr.* **26**, 149–154 (2011).

45. Huynh, N. U. & Youssef, G. Physical Evidence of Stress-induced Conformational Changes in Polymers. *Exp. Mech.* (2020) doi:10.1007/s11340-020-00673-7.

46. Youssef, G. H. Dynamic Properties of Polyurea. (University of California, Los Angeles, 2011).

47. Wang, Y., Zhou, X., Lin, M. & Zhang, Q. M. High-energy density in aromatic polyurea thin films. *Appl. Phys. Lett.* **94**, (2009).

48. Hattori, T., Takahashi, Y., Iijima, M. & Fukada, E. Piezoelectric and ferroelectric properties of polyurea-5 thin films prepared by vapor deposition polymerization. *J. Appl. Phys.* **79**, 1713–1721 (1996).

49. Wang, X. S., Takahashi, Y., Iijima, M. & Fukada, E. Dielectric relaxation in polyurea thin films prepared by vapor deposition polymerization. *Jpn. J. Appl. Phys.* **33**, 584–587 (1994).

50. Strong, A. B. *Plastics: Materials and Processing*. *Materials and Manufacturing Processes* (Prentice Hall, 1997). doi:10.1080/10426919708935166.

51. Groover, M. P. *Fundamentals of Modern Manufacturing Materials, Processes, and Systems, Fourth Edition 2010.pdf*. (John Wiley & Sons, Inc., 2007).

52. Wietzke, S. *et al.* Terahertz time-domain spectroscopy as a tool to monitor the glass transition in polymers. **17**, 19006–19014 (2009).

53. Zhao, Y. *et al.* Intermolecular vibrational modes and H-bond interactions in crystalline urea investigated by terahertz spectroscopy and theoretical calculation. *Spectrochim. Acta - Part A Mol. Biomol. Spectrosc.* **189**, 528–534 (2018).

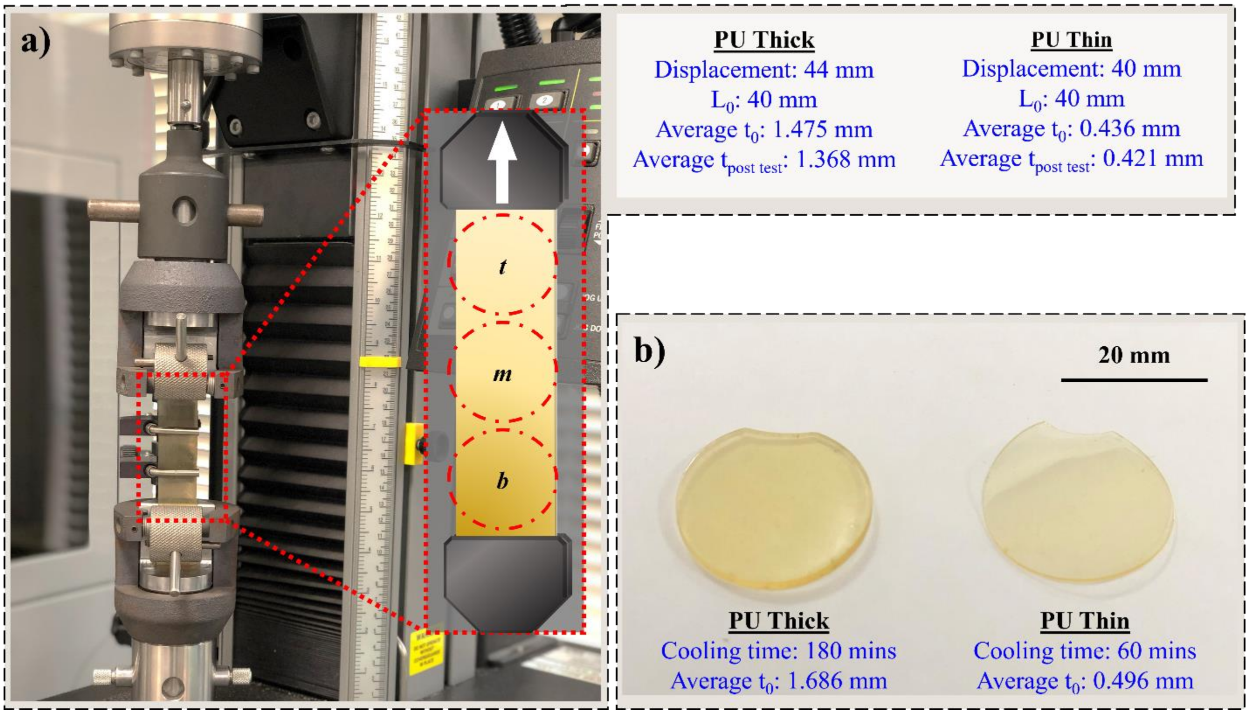

Figure 1.1: (a) Mechanical testing of polyurea strips using Instron 5843 load frame up to 100% strain also showing schematic of extracted discs from the load region, and (b) image of thermal loaded polyurea samples.

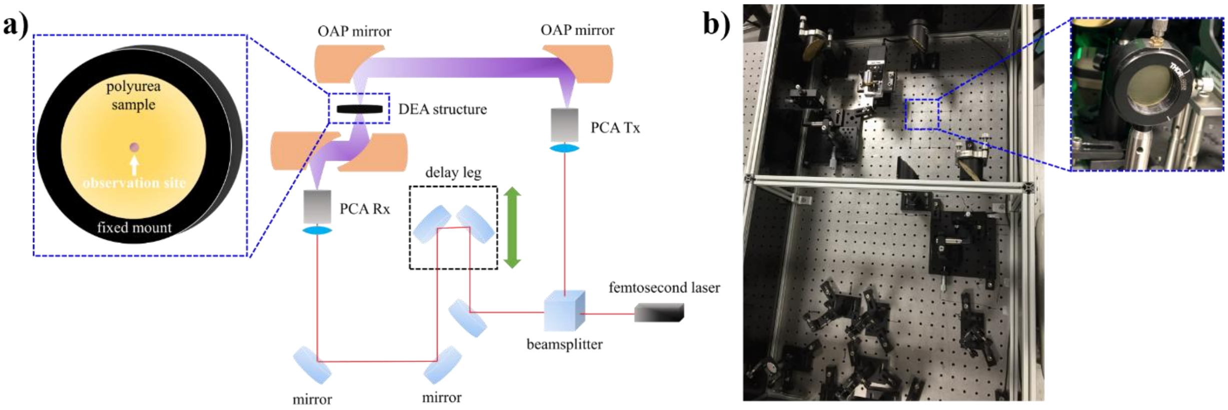

Figure 1.2: (a) Schematic of the polyurea sample mounted at the focal point of THz beam for interrogation of optical properties of virgin, thermally, and mechanically loaded conditions, (b) image of the built-in house THz-TDS system (inset shows a polyurea sample mounted during terahertz testing).

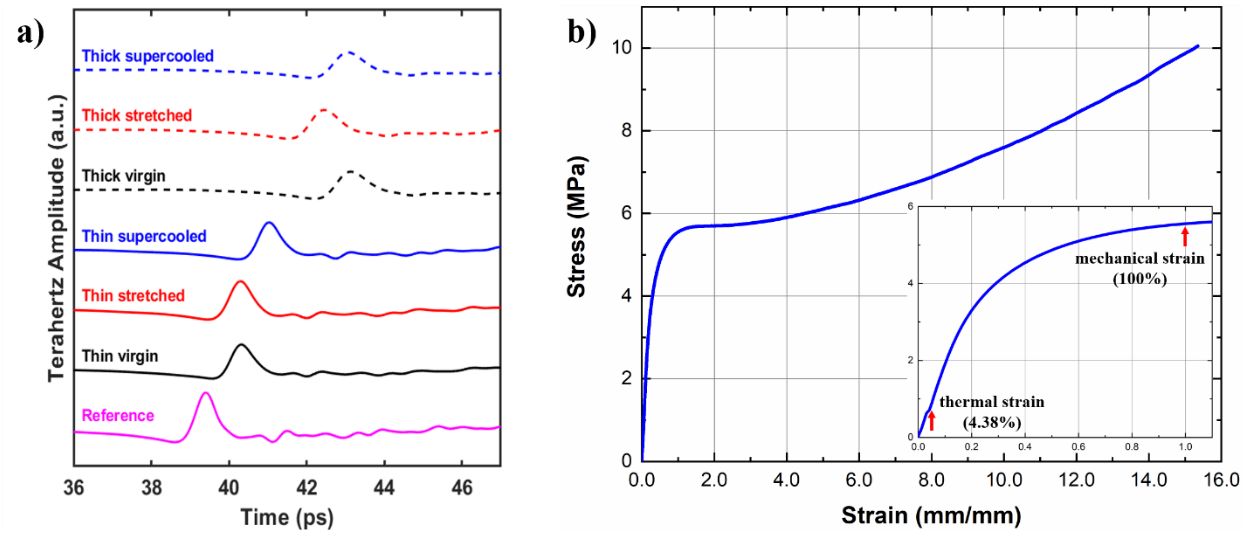

Figure 1.3: (a) THz time-domain signal of sample-free (reference), thick, and thin (virgin, thermally and mechanically loaded), and (b) typical engineering stress-strain curve of polyurea tested at a strain rate of 0.016 s^{-1}.

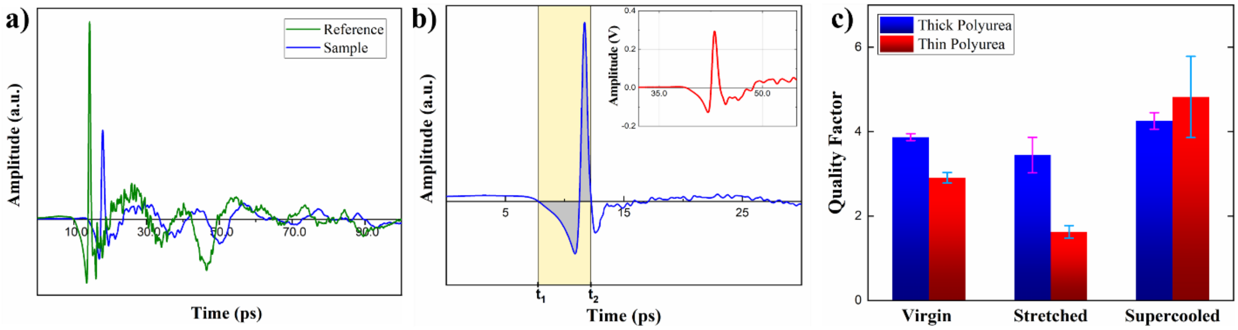

Figure 1.4: (a) An actual entire time-domain signal of a polyurea sample and its corresponding reference signal (b) schematic representation showing the steps to calculate the quality factor from a terahertz pulse (inset is an actual signal), and (c) the $\boldsymbol{Q}$ values of polyurea samples with different thickness and testing conditions.

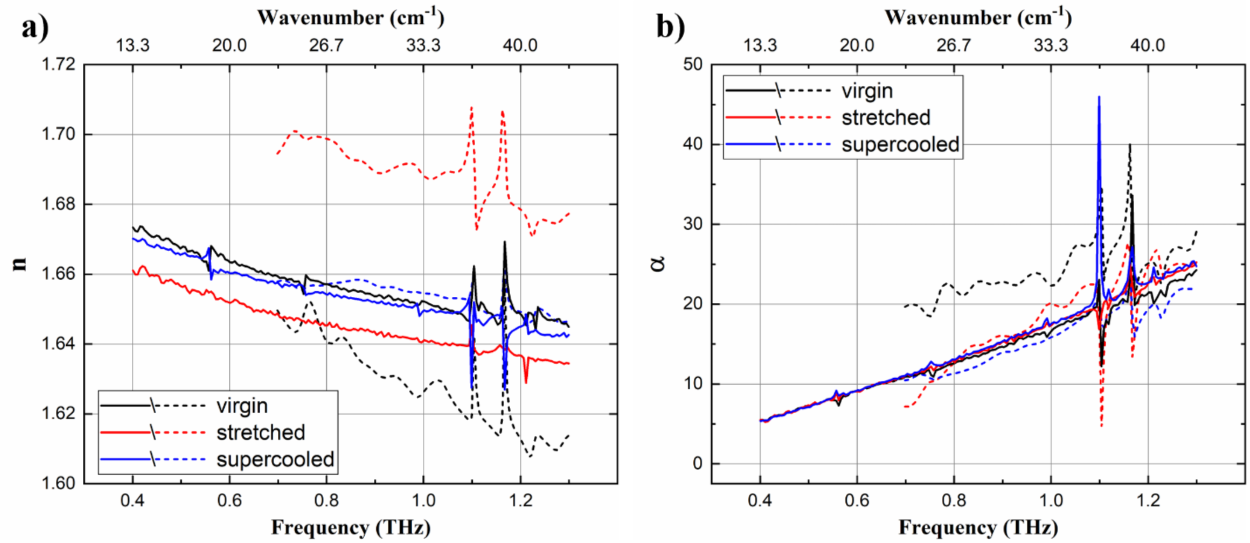

Figure 1.5: Result of (a) real refractive index and (b) absorption coefficient as a function of frequency and wavenumber. The optical properties for the thick (solid lines) and thin (dashed lines) polyurea samples were extracted over a range of 0.4 – 1.3 THz and 0.7 – 1.3 THz, respectively.

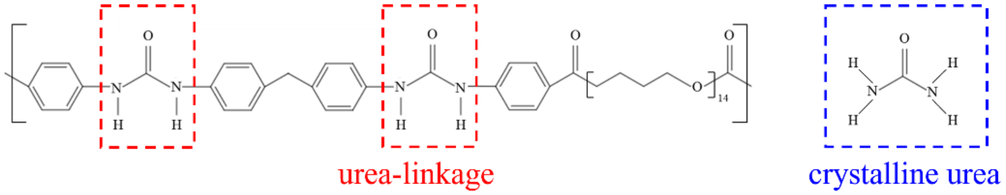

Figure 1.6: Comparison of the chemical structure urea-linkage in cross-linked polyurea used in this study and crystalline urea from [53].

Table 1.1: Summary of the characteristics of the THz time-domain signals extracted from Figure 3a. The thickness of each sample was mechanically measured.

Testing Conditions		**Ave. thickness (μm)**	**Peak amp. (mV)**	**Delay (ps)**	**n**	***κ***	**ε**
Reference		-	634±9	-	-	-	-
Thick PU	Virgin	1686±9	309±3	3.66±0.01	1.65±0.002	0.45±0.03	2.93±0.03
	Supercooled	1674±8	294±1	3.68±0.02	1.66±0.003	0.50±0.01	3.00±0.01
	Stretched	1368±12	336±3	3.06±0.03	1.67±0.01	0.39±0.01	2.95±0.02
Thin PU	Virgin	476±15	445±9	0.83±0.08	1.52±0.05	0.15±0.02	2.34±0.15
	Supercooled	466±29	487±27	1.09±0.03	1.70±0.02	0.003±0.05	2.90±0.06
	Stretched	421±47	510±20	0.92±0.10	1.66±0.07	-0.05±0.02	2.75±0.22

CHAPTER 2

Physical Evidence of Stress-induced Conformational Changes in Polymers

N. Huynh and G. Youssef*

Experimental Mechanics Laboratory, Mechanical Engineering Department, San Diego State University, 5500 Campanile Drive, San Diego, CA 92182-1323, USA

Abstract

Background: Polymer mechanics and characterization is an active area of research where a keen effort is directed towards gaining a predictive and correlative relationship between the applied loads and the specific conformational motions of the macromolecule chains. Objective: Therefore, the objective of this research is to introduce the preliminary results based on a novel technique to *in situ* probe the mechanical properties of polymers using non-invasive, non-destructive, and non-contact terahertz spectroscopy. Methods: A dielectric elastomer actuator (DEA) structure is used as the loading mechanism to avoid obscuring the beam path of transmission terahertz time-domain spectroscopy. In DEAs, the applied voltage results in mechanical stresses under the active electrode area with far-reaching stretching in the passive area. Finite element analysis is used to model and simulate the DEA to quantify the induced stresses at the observation site over a voltage range spanning from 0 V to 3000 V. Additionally, a novel analysis technique is introduced based on the Hilbert-Huang transform to exploit the time-domain signals of the ultrathin elastomeric film and to defy the limits set forth by the current state-of-the-art analysis techniques. Results: The computational result shows a nonlinear relationship between the effective stresses and the applied voltage. Analysis of the terahertz time-domain signals shows a shift in the delay times and a decrease in signal peak amplitudes, whereas these characteristics are implicitly related to the change in the index of refraction. Conclusions**:** In all, the results evidentially signify the interrelationship between the conformational changes and applied mechanical stress.

Keywords: In-situ Characterization, Dielectric Elastic Actuators, Terahertz Spectroscopy, Polymer Response

****Corresponding Author:*** gyoussef@sdsu.edu

2.1 Introduction

Polymers continue to be an important class of materials for a plethora of load and non-load bearing applications, where polymers constitute a large portion of raw materials used in engineered products such as cellular phones, automobiles, and household goods, to name a few examples. The diversity of the sub-classification of polymers mirrors the variety of applications they are used in, including thermosets, thermoplastic, elastomers, biodegradable, and biopolymers. While this classification is not meant to be comprehensive nor exclusive, it is instead a shortlist to elude to the differences in the underlying molecular structure. Typical to any of these subclasses is the sensitivity to applied loads, regardless of the amplitude and directionality, which gives rise to molecular rearrangements that may be reversible or irreversible based on a balance between the strain energy imparted on the sample during loading and the activation energy required for irreversibility. The response of polymers is a scientific problem, extending over multiple time and length scales, that has gained attention from theoretical, experimental (in vitro experiments), and computational (*in silico* experiments) perspectives [1–6]. While the *in silico* experiments using Molecular Dynamics (or the like) approaches have proven to be essential tools polymer science and engineering, continuum modeling remains essential not only to bridge the scale gap but also for practical applications. The reader is referred to the important contribution by Frenkel for a quick, yet insightful, review of the state of *in silico* research [6]. Here, the focus in on *in vitro* experimentation, but at the same time leveraging finite element analysis. The strain energy density is the result of the applied load and the deformed geometry, while the activation energy is an intrinsic property of the macromolecule that is fundamentally connected to the bonds linking the backbone as well as the final arrangements of molecules after polymerization [7]. These quantities should be investigated simultaneously, given the relaxation behavior of polymers that negates the reversible contributions during the load history to reconcile the balance between strain and activation energies. The mechanical loading scenario and characterization methodology must be concurrently performed to capture the stress-induced macromolecule conformational arrangements.

It is well-known that the mechanical response of polymers exhibits a strong dependence on the molecular structure, the loading rate, and temperature such that thermosets, thermoplastics, and elastomers have unique stress-strain behavior that may span over a few hundred percentages of strains [7–9]. Elastomeric materials have a mechanical response with large stretch ratios, indicating a corresponding increase in the mechanical work done on the material. The mechanical work is captured by the strain energy calculated by taking the area under the stress-strain curve [10,11]. There exist numerous ways of measuring strain where the selection of the method depends on (1) the strain percentage, e.g., large strain extensometer, (2) the scale with which optical methods are suitable for microscale measurements, and mechanical methods are feasible for meso and macro scale, and (3) the strain rate where the sampling rate is the deciding factor [12–14]. However, load application overwhelmingly relies on screw-driven or servo-hydraulic mechanisms in a load-frame type structure, but other experimental setups exist to investigate the mechanical response of materials under different strain rates [14]. Nonetheless, much of the strain and stress measurement/application methods are not conducive for integration in analytical chemistry instrumentation (discussed next) to elucidate the interrelationship between conformational changes and mechanical loading. Therefore, there is a need to develop a mechanism allowing the remote control of the state of stress without obscuring the observation site.

Dielectric elastomer actuators (DEAs) have been emerging as a viable actuation mechanism since their initial inception in the mid-1990s [15–18]. At its essence, DEAs leverage the compliant mechanical behavior of elastomers to achieve large deformation via the application of an electric field. When the latter is applied across the thickness of the actuator, it results in a localized compressive stress that affects the area surrounding the electrode region where the electric field was applied. The standard DEAs configuration can be round or diamond geometry such that the electrode area is either circular or rectangular, respectively. While the former is used to generate out-of-plane axial deformation, the latter is used to induce a sizable in-plane displacement. A common shortcoming of such actuator configuration for the purposes of *in situ* characterization of the polymer response is the electrode area, where the entire surface of the insulator is covered with a flexible conductive material. Therefore, the presence of the conductive material impedes the direct propagation of electromagnetic waves used for characterization. Here, an annulus electrode geometry is first investigated since it provides a generous unobstructed portion of the sample surface. It is worth noting that a biaxial state of stress can also be applied using an electric or mechanical camera shutter; however, the leaves of the mechanism may obstruct the propagating electromagnetic wave while posing a challenge in inducing precise, remote control of the deformation. Future research will focus on developing a new sample structure that uses an electrical shutter mechanism for *in situ* loading with spectroscopy.

To elucidate the molecular structure of polymers, scientists and engineers usually resort to *ex-situ* spectroscopy techniques such as microwave, Raman, and Fourier transform infrared spectroscopy (FTIR) operating between wavenumbers of 1 cm^{-1} and 10 cm^{-1} for the former, and 400 cm^{-1} and 14000 cm^{-1} for the latter two [19–21]. The near and mid-infrared spectroscopy techniques are positioned for delineating the vibrational modes in the mid to high terahertz region, thus leaving the frequency vibrational modes associated with dynamic conformational changes in the low terahertz (THz) regime undetected. There is a well-known two-fold limitation of FTIR in the area of experimental and mechano-chemical characterization. First, FTIR is a surface spectroscopy technique with a penetration depth of 0.5 μm limiting the investigation to the first few layers of the material [22,23]. Second, FTIR is unsuitable for integration of *in situ* dynamic mechanical characterizations since the sample must be stationary during the scan. On the other hand, terahertz based spectroscopy techniques are emerging as not only supplementary but also essential tools for probing the fingerprint region of materials with a higher resolution than the current state-of-the-art techniques [24–27]. Advantageous to the study of polymers (including biopolymers) is the safe level of electromagnetic radiation due to the low photon energy of the terahertz waves. That is to say, a propagating terahertz wave will be able to observe the intrinsic properties of matter without imparting any irreversible changes to the microstructure. Terahertz-based spectroscopy can be used to trace certain types of low-frequency vibrational characteristics, such as boson peaks [28,29], and inter- and intramolecular vibrational modes including translational lattice vibrations of C-C bond in methylene groups at 2.2 THz, strong damping in the amorphous region at 1.5 THz, vibrations due to the intermolecular hydrogen bonding of polyhydroxy butyrate (PHB) at 2.49 THz, and vibrations due to the helical structure along fiber axis of PHB at 2.92 THz, to name a few [30–40]. Additionally, some mechanical properties have been investigated using terahertz, where the results are in excellent agreement with the current state-of-the-art (e.g., glass transition temperature using Differential Scanning Calorimetry) [41]. These hallmark characteristics of THz waves signify its suitability for integration in experimental mechanics studies, or *in situ* mechano-chemical experimentation.

The overarching objective of this research is to disseminate a new framework for the behavior of elastomeric polymers by leveraging the advantages of dielectric elastomer actuator structures and terahertz time-domain spectroscopy. The former was used as the sample structure that was subjected to remotely controlled varying levels of stresses, while the latter was concurrently used as a non-invasive, non-contact, non-destructive bulk spectroscopy technique. A novel analysis technique (not reported in the literature before for analysis of spectroscopic data) is presented and discussed.

2.2 Experimental Protocol

The DEA structure was used to apply a varying amplitude mechanical stress remotely by changing the applied voltage across two parallel electrodes, whereas the observation site was characterized using THz-TDS operating in the transmission mode. The following sections delineate the process used to prepare and characterize the sample using the non-invasive, non-contact, and non-destructive THz spectroscopy technique [42]. A finite element simulation was used to quantify the stress in the observation site by replicating the experimental conditions in the solver environment.

2.2.1 Test Sample Structure

The DEA sample consisted of an elastomeric dielectric insulator film with areas covered with a flexible conductive material to apply an electric field across the thickness selectively. A double-sided acrylic tape (3M™ VHB™ Tape 4905) with an as-received thickness of 0.5 mm was manually stretched from an initial diameter of 25.4 mm to a final diameter of 76.2 mm (Figure 2.1a-b), which resulted in a film thickness of 30±6 µm (estimated from the time domain spectroscopy signals). Pre-straining the VHB has two advantages. First, by equi-biaxially stretching the film, the thickness consequently decreases; therefore, a lower applied voltage is required to obtain the same mechanical response. Second, pull-in instability can be avoided by pre-straining the film, which is kept in tension and effectively avoids buckling [43]. The pull-in failure mode occurs when the Maxwell pressure exceeds the third principal compressive stress of the elastomeric film. Plante and Dubowsky experimentally demonstrated that at a low pre-stretch ratio, the dominant failure mode for DEA is pull-in; however, at a high pre-stretch ratio, the dominant mode of failure is the dielectric breakdown [43]. While these two failure modes constitute the dominant mechanisms, material strength remains a concern based on the stretch rate and the pre-stretching percent [43].

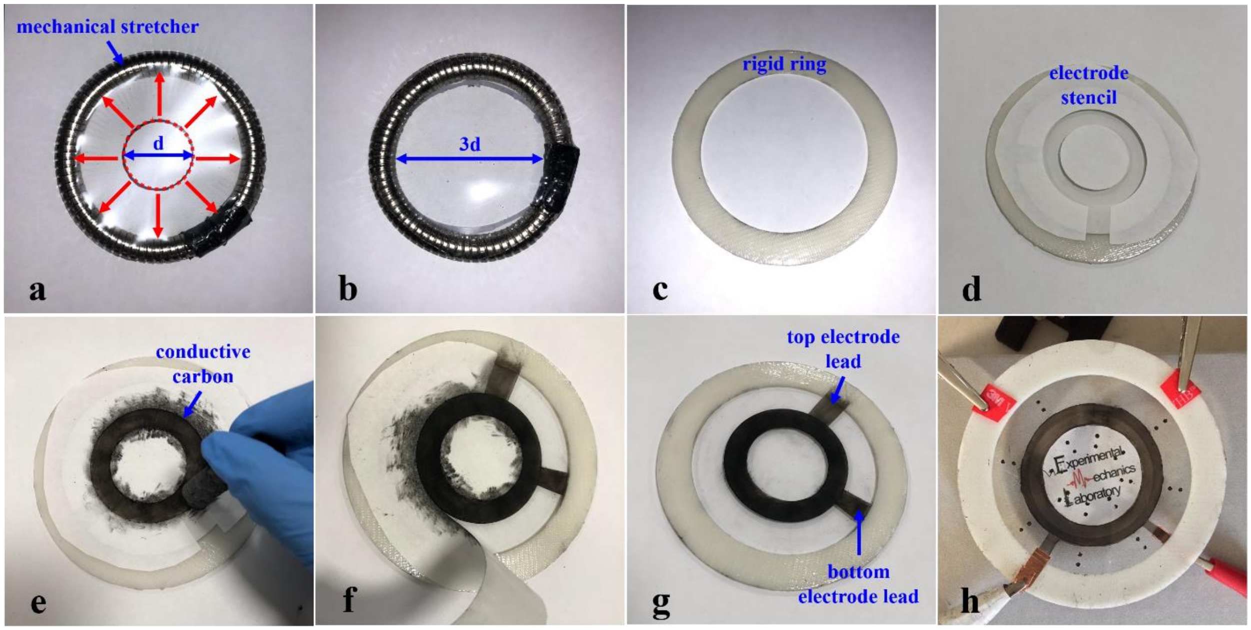

Figure 2.1: Fabrication steps of the DEA samples showing the initial stretching, deposition of the electrode, and the application of the electric field during testing.

After the elastomer film was stretched, it was then attached to a rigid plastic ring (Figure 2.1c) with a 76 mm ID and 102 mm OD to avoid inducing unintended external strains during testing and data collection, while providing the necessary mechanical boundary conditions for proper operation of the actuator as discussed by Plante et al. [43]. Templates of the electrode configuration (Figure 2.1d), including the lead locations, were prepared *a priori* by printing on a single-sided adhesive paper that was used as a mask during the application of the conductive graphene powder (AZ Laboratories, Ultra Conductive Graphene Powder) to both sides of the adhesive elastomer (Figure 2.1e-f). Since the VHB film exhibits intrinsic tackiness, the conductive graphene powder stuck to the surface upon lightly tapping the powder using a foam applicator.

Upon removal of the mask, the conductive electrodes were revealed (Figure 2.1g), and two copper tape strips, which were used as conductive leads to connect the applied field to the active electrode area, were then attached, (Figure 2.1h). To actuate the DEA, a positive DC voltage was applied to one side of the VHB film while the other side was grounded using a DC power supply (Circuit Specialists, CSI3020X) and a high-voltage amplifier (Trek 609B-3). It is worth noting that the spot size of the THz wave is <<3 mm, which was focused at the middle of the sample (as discussed next). At 1 THz, the beam diameter of the terahertz propagating wave is ~300 μm. The remoteness of the THz characterization site with respect to the inner diameter of the electrode (38 mm) excludes the effect of the electric field on the spectroscopy THz wave. Furthermore, the self-boundedness of the electrode geometry indicates that the effect of the electric field is localized and limited to the active electrode area. Future research will focus on determining the bounds of applicability, relating the inner diameter of the electrode to the attributes of the THz wave. The applied voltage ranged from 0 V (used thereafter as the control) up to a voltage where the mechanical failure occurred (exhibited by the tearing of the VHB film due to localized wrinkling around the electrodes). On average, after performing the same testing protocol on seven different DEA samples, the mechanical failure corresponded to approximately 3250 V. Consistent with the previous investigation of Plante et al. and Wissler, this voltage and the pre-stretched ratio construed that the VHB was marginally stable to guard against pull-in failure [43,44]. Moreover, the tearing of the film occurred due to the straightening and unfolding of the polymer chains [43]. It is worth noting that the applied voltage was increased at an increment of 250 V. In all, seven DEA samples were constructed and tested until mechanical failure, leading the results summarized below.

2.2.2 Terahertz Time-Domain Spectroscopy (THz-TDS)

Terahertz time-domain spectroscopy (THz-TDS) was set up in transmission mode to facilitate the objective of *in situ* characterization of the stressed-area in the middle of the DEA sample, referred to as the observation site, where the VHB sample was situated at the focal point of the terahertz beam path with a spot size of 300 μm at 1 THz. It is important to note that the area of observation for the investigation using terahertz was not obstructed by the electrode materials or the leads (Figure 2.1 shows a schematic of the DEA structure). A schematic of the transmission mode of the terahertz time-domain spectroscopy can also be seen in Figure 2.2. Here, a pulsed femtosecond laser with a pulse width of 150 fs was split into two different paths. The first path of the optical beam was focused on a photoconductive antenna transmitter (PCA Tx, TeTechS, T-Era-100A-800) to generate terahertz waves. The transmitter PCA was biased with 45 Vpp square wave of 8000 Hz using a square wave generator (TeTechS Square Wave Generator). Using a series of off-axis parabolic (OAP) mirrors, the emitted terahertz beam was first focused onto the observation site of the sample. The refraction from the sample was then collimated and focused onto a photoconductive receiver antenna (PCA Rx, TeTechS, T-Era-20D40P-800) at the same instant the delayed second half of the optical beam activated the photoconductive receiver to convert the terahertz waves into a measurable electrical signal. The signal was measured using a low-noise amplifier (TeTechS, LNA) and was recorded using a built in-house data acquisition system. The collected data only underwent time-domain signal analysis given the limitation of frequency-domain based analysis [45], noting that the changes in the attributes of the terahertz pulse are implicitly associated with the complex index of refraction [45–58]. In here, the time-domain signals at each level of applied electric field were analyzed to report the amplitude, full-width half maximum (FWHM), the 0-100% rise time, and the time-delay between the arrival of the reference time signal (referring to sample-free, baseline measurement) and the signal of the VHB at the observation site.

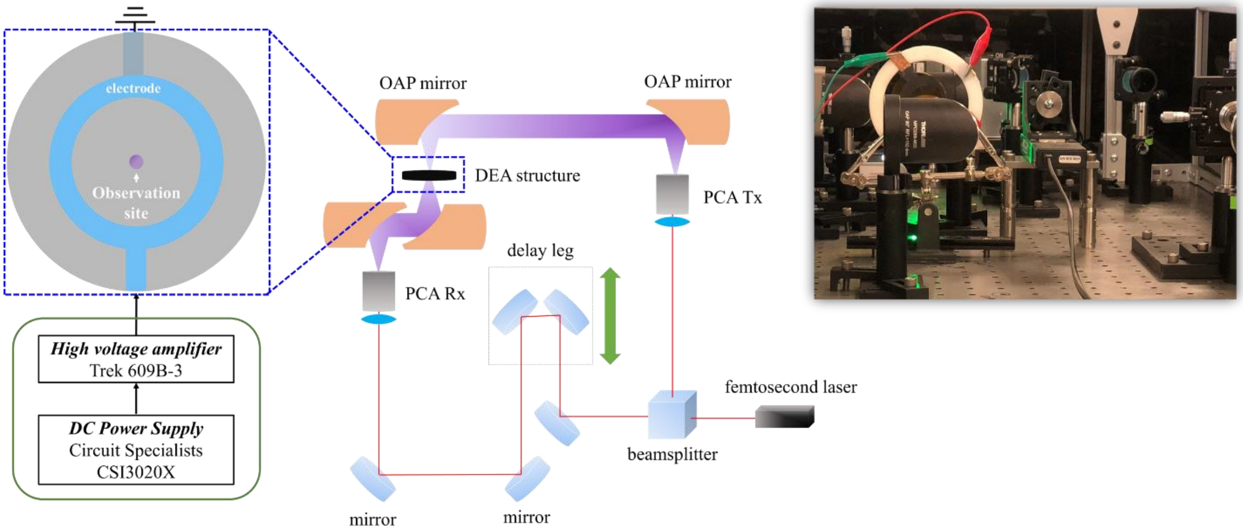

Figure 2.2: Schematic of the non-contact, non-destructive, non-invasive THz-TDS setup operating in the transmission mode to provide evidence on the conformational changes due to the applied stress.

2.2.3 Stress Estimation using Finite Element Simulation

The full-field state of stress at the observation site was estimated using a finite element simulation based on the Maxwell stresses developed under the surfaces of the electrode. That is to say, the application of an electric field across the thickness of the stretched VHB film resulted in the accumulation of opposite polarity charges at the electrode surfaces; hence, it attracted them closer to each other and induced localized compressive stresses that resulted in the reduction of the thickness under the electrode, which in turns causes an increase of the thickness of the middle area of the DEA. At the onset, a geometry analogous to that of the sample used in the physical testing (Figure 2.3) was modeled in the finite element analysis (FEA) environment (Comsol Multi-Physics$^{®}$) with a fixed constraint boundary condition applied to the most outer perimeter of the DEA sample resembling the rigid plastic ring used in the experiment to prevent rigid-body motion and external deformation. The VHB continuum was spatially discretized using a linear element with an average element size of 3 mm, whereas the thickness direction had at least two scaled elements.

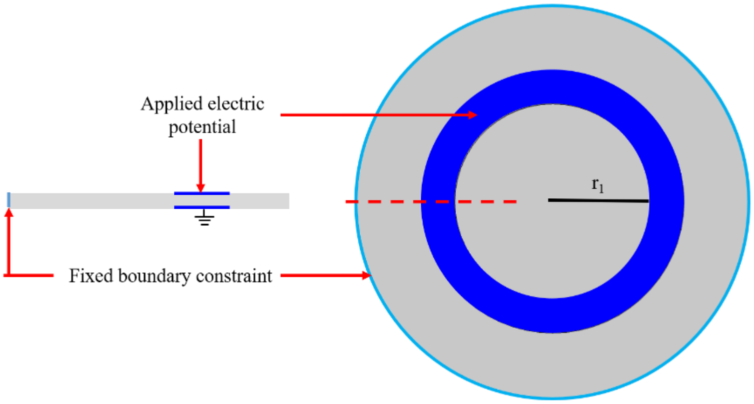

Figure 2.3: Schematic representation of the FEA model showing the boundary conditions.

Following the work of Pelrine [16], the electrostatic pressure (p_{es}) due to the applied electric field was converted *a priori* to an elastic compressive force (p_e) such that

$$p_e = -p_{es} = -\varepsilon_r \varepsilon_o \left({}^{U}\!/_{t} \right)^2 \tag{2.1}$$

where, ε_r is the relative dielectric constant of the VBH material (taken to be 3.2), ε_o is the free-space permittivity (8.85x10^{-12} F/m), *U* is the applied voltage ([0:250:3500] V) at the conductive electrodes across the thickness, and *t* is the thickness of the stretched film. The elastic compressive force (p_e) was then parametrically applied on the electrode area in lieu of the electric field. In short, Equation 2.1 provides two alternative approaches to accomplish the same applied pressure via changing the electric field, namely. reducing the thickness or increasing the applied voltage. The latter approach was adopted herein.

Given the stretchability of the VHB materials, the above FEA model was then resolved by prescribing the material to obey hyperelasticity following the incompressible Yeoh model, whereas the strain energy density function (W) is given by

$$W = C_{10}(I_1 - 3) + C_{20}(I_1 - 3)^2 + C_{30}(I_1 - 3)^3 \quad (2.2)$$

where, I_1 is the first invariant of the left Cauchy-Green deformation tensor, and C_{10}, C_{20}, and C_{30} are material parameters determined by fitting the experimental data of the material to the stress expression derived from the energy potential, which were taken to be 80.3, -0.765, and 9.84×10^{-3} kPa, respectively [44,59]. The third-order dependence on the first invariant is a characteristic advantage of the Yeoh model enabling higher accuracy while avoiding instabilities associated with other hyperelastic models, i.e., Yeoh model is Drucker stable since it has no dependence on the second invariant [7]. The latter is justified since the free energy of elastomers (as it is the case herein) is weakly dependent on the second invariant. In all, the FEA simulation is an uncoupled hyperelastic-electrostatic model, which was previously reported by Pelrine [16] to adequately represent the behavior of the DEA structure.

A final note is warranted about the time-dependent response of the VHB polymer undergoing constant stress over the scanning period. The strains of the VHB were shown experimentally by Wissler to reach a steady-state value of 120 s, which means the viscoelastic effect is negligible within the experimental time frame [44]. This supposition was further explained by Plante et al., explicating the inadequacy of DEAs for long-term actuation [43]. However, it is the objective of future research to systematically (experimentally and computationally) investigate the viscoelastic response of polymers (including VHB) using THz-TDS following the same framework established herein. The extraction of the dynamic mechanical properties of polymers will assist in the construction of a fully coupled, electrostatic, visco-hyperelastic simulation.

2.3 Results and Discussion

While it is well-known that the applied voltage on the electrode area in a DEA structure consequently results in mechanical stresses in both the active and passive areas, it was important to quantify the amplitude of the stresses, as well as its spatial distribution, corresponding to each operating condition based on the results from the FEA simulations. Figure 2.4 shows the results of the computational simulations elucidating the effective Von Mises stresses at two different applied electric fields. The Mises effective stress as a function of radial distance from the observation site towards the edge of the active electrode region at 2000 V and 3000 V are shown in Figure 2.4a and 2.4b, respectively. At the bottom panels of these figures, the Von Mises contour plots elucidate the full-field results of the stress. The effective stresses within the observation site as a function of the entire range of investigated electric field are also shown in Figure 2.4c. The full-field stress contour plots demonstrated nearly a uniform state of stress in the middle of the passive area, where the THz-TDS characterization took place. The Mises stress increased from 0.6 kPa at 1000 V to 2.5 kPa at 2000 V and finally reached a value of 7.3 kPa at 3000 V. However, it corresponded, not surprisingly, to approximately zero out-of-plane stresses regardless of the applied voltages which is due to the incompressibility of the VHB material and the resulting equi-biaxial stretching due to the symmetric geometry of the electrodes. Quantitatively, the plots in Figure 2.4 shows the Mises stresses within the passive area varied between 7.3 kPa at the center to 7.2 kPa at 1.9 mm radially away from the center at 3000 V. This implies that the mechanical response was spatially uniform within the 3 mm maximum THz wave spot size used to interrogate the material. It is worth noting that the results shown in Figure 2.4 omitted the effect of pre-stretching due to the sample fabrication process (Figure 2.1) given the static nature of the simulation, where the time-dependent properties are suppressed. In other words, accounting for the pre-stretch stress would offset the result linearly.

The Maxwell stress under the active electrode region is directly proportional to the square of the applied electric field (Equation 2.1), while the induced stresses at the observation site also exhibited nonlinear dependence on the stretch as described by the expression of the Yeoh

Helmholtz free-energy potential in Equation 2.2. Therefore, the reported Mises stresses showed a nonlinear dependence on the applied voltage. The results signify that the applied voltage can remotely control the amplitude of the stress (however, nonlinearly) in the passive area, as shown in Figure 2.4c. The stress contour plots also explicated the discontinuity behavior at the boundary between the active area where the electric field was applied and the surrounding passive areas, which were found to be in good agreement with the results in [43]. This can be leveraged in future research to concurrently explicate the dependence of the polymer response on the spatial variation of stress by developing novel electrode geometries. In all, as deduced from the contour plots shown in Figure 2.4, the applied voltage in the active area resulted in uniform in-plane stresses that loaded the macromolecule chains in the vicinity of the observation site and effectively resulted in uncoiling and straightening of the chains, as discussed next.

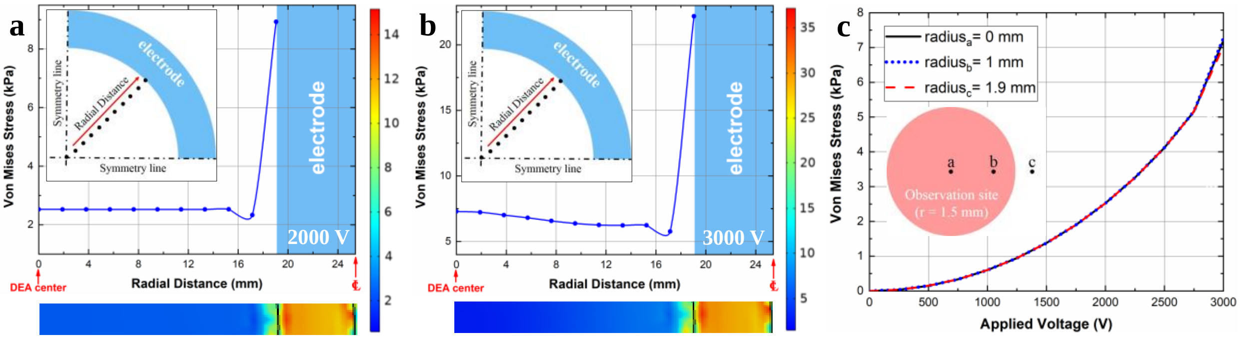

Figure 2.4: Computational results from the DEA finite element simulation showing the (a) contour surface plots of the effective Von Mises stresses at different applied voltages, (b) Von Mises effective stress as function of the radial location from the center of the DEA to the edge of the electrode active area, and (c) Von Mises effective stress in the vicinity of the THz observation site as function of voltage.

Figure 2.5a shows the time-domain signals collected using the THz-TDS setup. The results include the signal without the DEA sample in the terahertz beam path (denoted as ‘Reference’). It also encompasses the signals with the sample in the terahertz beam path while it was being subjected to an increasing voltage from 0 V (referred to as ‘Control’) to 3000 V. On the other hand, Figure 2.5b plots the same time-domain signals but with a focus on the major terahertz peak arriving between 20 ps and 30 ps, clearly showing the drifting locations and changes in the amplitude of the peaks with varying applied voltage. As soon as the applied voltage increased beyond 3000 V, mechanical failure occurred, where the VHB sample was ripped into two pieces starting at the electrode area. That is, the localized induced mechanical stresses under the electrodes due to the applied electric field exceeded the intrinsic mechanical strength of the material, as discussed above. This indicates that mechanical stress is indeed developing and compressing at the observation site as demonstrated based on the FEA simulation results. Additional physical evidence of the generation of mechanical stress under the electrode was the dilation of the electrode surface, where the region between the inner and outer diameter of the electrode annulus widened (Figure 2.6b) to 10.4 mm at 3000 V constituting a 30% increase from the 8.0 mm initial width when no electric potential was applied (Figure 2.6a). The increase in the annulus width changed non-monotonically as a function of the voltage such that the width of the annulus increased to 8.35 mm, 8.48 mm, 8.86 mm, 9.79 mm, and 10.35 mm corresponding to 500 V, 1000 V, 1500 V, 2000 V, and 2500 V, respectively. The nonlinear widening of the electrode surface is consistent with the suppositions set forth by Equation 2.1 and Equation 2.2. Notably, the distance between the markers (black dots on the surface of the DEA sample) located outside and inside the electrode area were also found to decrease, indicating that the external and internal areas were experiencing compressive stress. In all, the dilation of the electrode areas in response to the Maxwell stresses under the surface due to the oppositely poled electrodes coming closer together resulted in a uniform state of stress in the observation site. This points toward the validity of using the DEA framework as a method of applying mechanical stresses to elastomeric polymers without obscuring the observation site. Plante et al. analytically and experimentally demonstrated the development of stresses in the active area (i.e., under the electrode) as well as the passive area surrounding the electrode area [43]. Future research will focus on dynamically loading the sample using an AC electric field, which will result in cyclic mechanical stresses, i.e., giving rise to the viscoelastic response of the material. It is important to reiterate that the focus herein is not on the ability of the DEA to exert mechanical work, nor on investigating the failure, rather the objective is to demonstrate the effect of applied stress on the conformational entropy as discussed later.

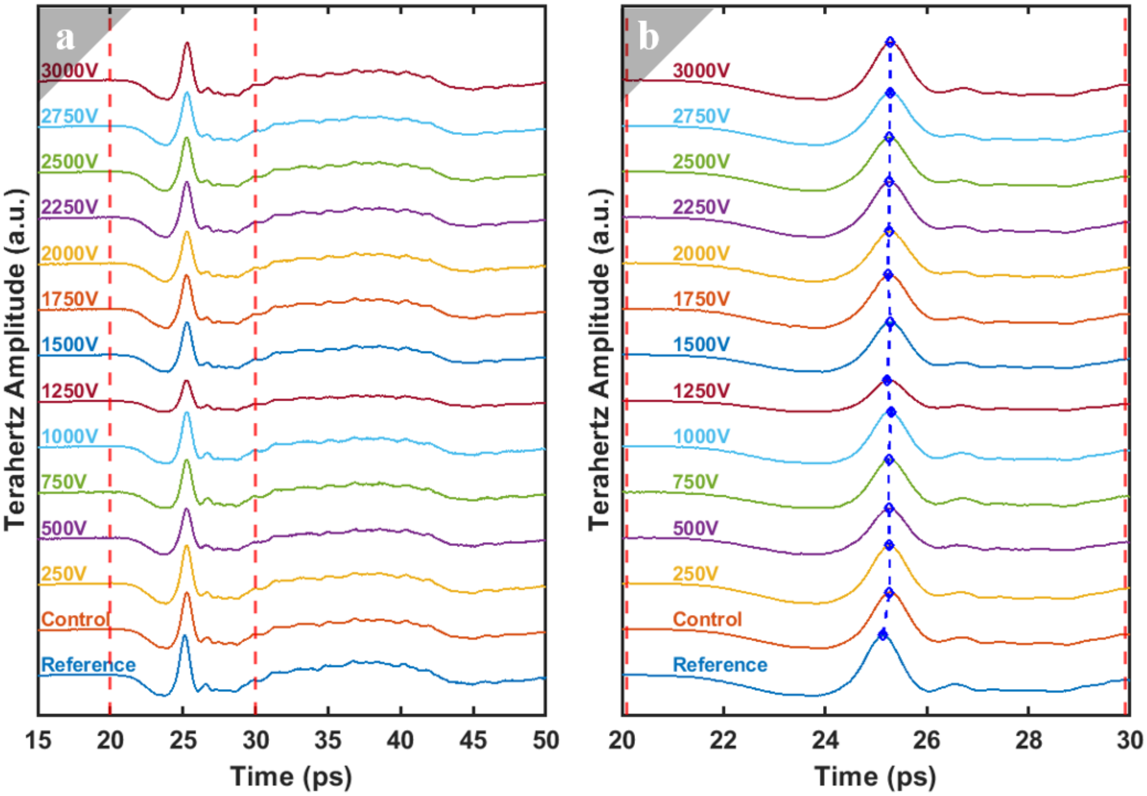

Figure 2.5: Terahertz time-domain signals (a) of sample-free (reference), unbiased-sample (control), and at increasing applied voltage ranging from 250 V to 3000 V at an increment of 250 V with (b) truncated signals between 20 and 30 ps to show the shifting temporal locations of the peaks and changes in the signal characteristics.

The results, shown in Figure 2.5, also point to changes in the signal characteristics based on the interactions between the propagating terahertz waves and the observation site of the DEA structure. Table 2.1 succinctly summarizes the extracted signal attributes as a function of the applied stresses in the electrode area (noting that stress is corresponding to the applied voltage across the thickness). Table 2.1 lists the estimated change in the thickness under the electrode and the estimated change in the thickness of the VHB film at the observation site as well as the amplitude, full-width at half-max (FWHM), rise time, and time delay of signal arrival between the corresponding applied voltage and the reference. First, the terahertz amplitude is found to change slightly (0.81±0.03 a.u.) compared to the reference signal (0.88 a.u.), representing an 8% reduction in the amplitude. The initial reduction in the amplitude between the reference and control conditions is attributed to the change in the imaginary part of the index of refraction (i.e., absorption coefficient) due to the presence of the stretched VHB film. Regardless of the cellular microstructure of VHB, the resulting change in the signal characteristics are associated with the interaction of the propagating terahertz wave with the polymer solid occupying the observation site. As the voltage increases the compression of the thickness under the electrode will induce a stretching of the annular electrode width and consequently compress the area inside the inner diameter of the ring, thus, the thickness of the VHB at the observation site will increase. This can be confirmed by the FEA simulation results seen in Table 2.1. That is to say, the reported further change of the signal amplitude is due to the change in the sample complex index of refraction upon applying the mechanical stress. The compression of the VHB due to the radial stress at the observation site results in an increase in the refractive and the absorption coefficient. As discussed above, the self-boundedness of the annular electrode, the distance between the opposing electrodes, the insulation properties of the VHB polymer, and the remoteness of the observation site from the inner diameter of the electrode indicate the negligible effect of the applied electric field on the THz waves. The change in the amplitudes, whether from the reference sample-free to control (unbiased sample) or from the control to the biased conditions, are implicitly related to the change in the extinction coefficient since the reduction in the amplitude is a measure of damping.

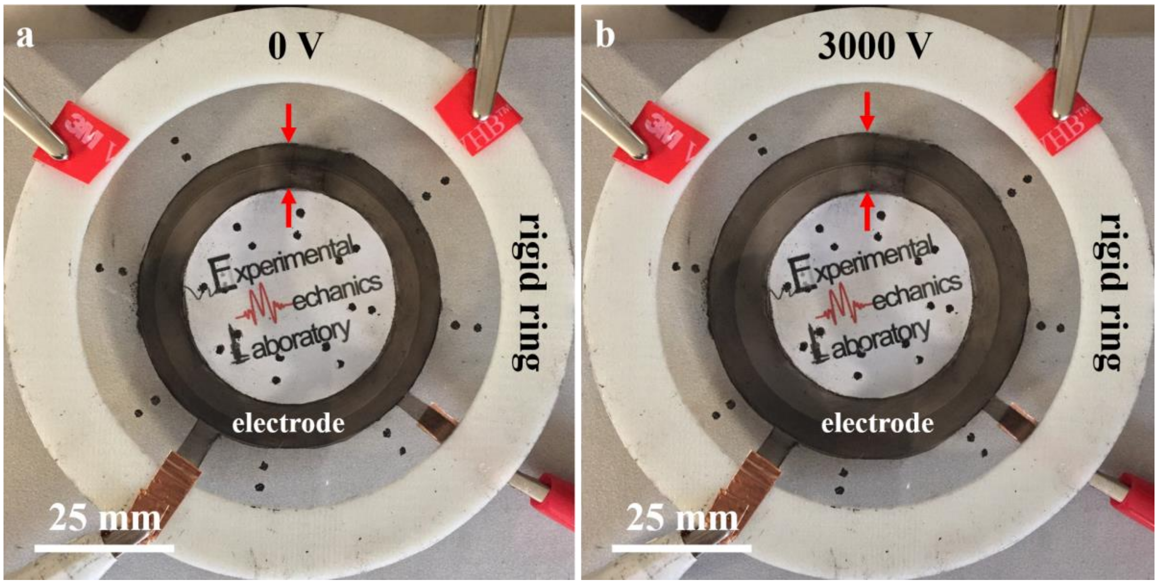

Figure 2.6: (a) starting DEA structure at 0 V showing the electrode configuration and (b) dilated electrode and stressed passive areas at 3000 V.

In addition to the amplitude variations, the temporal characteristics of the waves are also dependent on the applied stresses, which can be connected to changes in the real part of the index of refraction. These temporal attributes include the FWHM, the rise time, and the delay time of arrival, shown graphically in Figures 2.7a, 2.7b, and 2.7c, respectively, based on the data from Table 2.1. A sudden change in the attributes of the time domain signals around 1250 V can be seen, where the FWHM and delay time were found to be 0.5104 ps and 0.08 ps, respectively. This change is thought to be associated with an initiated material instability resulting in a change in the mechanical deformation behavior under the electrode and at the observation site, after which, and once, the DEA structure re-equilibrated, the quasi-linear relationship between the applied voltages and induced stretches commenced. The peak width leading to the loading condition at 1250 V (14.1 kPa) continues to decrease due to an increase in the strains at the observation site, which, in turn, affects the local values of the strain energy. To better elucidate the underlying molecular changes, the FEA analysis should be coupled with molecular modeling and simulation to discern associated entropic evolution from conformational changes. This will be the focus of future *in* *silico* studies. The broadening in the peak width at 14.1 kPa also corresponds to inflection of the delay time, where the difference between the arrival of the reference (sample-free) wave and the arrival of the terahertz wave after passing through the stressed-sample is found to be 0.0833 ps. This suggests a drop in the index of refraction (i.e., getting closer to the index of air). The real part of the index of refraction can be calculated from the delay time (Δt) between the initial arrival of the reference wave and the sample signal such that $n = 1 + (c\Delta t/\delta)$, where c is the speed of light in vacuum and δ is the thickness of the VHB film. Therefore, any changes in the delay time signify a variation in the index of refraction (n). Using the data in Table 2.1, the index of refraction is estimated to be 1.71, which is in good agreement with the published index by the manufacturer by considering the stretching effects on the optical properties of the material.

Due to the limitation of the existing state-of-the-art analysis techniques, terahertz time-domain signals of ultrathin samples, as it is the case herein, are not suitable for transformation to the frequency domain based on the limits set by Scheller et al. as a function of frequency resolution, and bandwidth of the signal [45]. In Fourier Transform based analysis technique, Scheller et al. discussed that the prerequisite for the lower bound for sample thickness using terahertz spectroscopy is defined based on, $\delta_{min} = c/2n\Delta f$, where, the refractive index is taken here to be 1.79 [60] and Δf is the bandwidth (estimated to be 1.5 THz for our setup). That is, the time-domain signal from a sample with a thickness below 56 μm cannot be effectively analyzed in the frequency domain. This is a shortcoming of the post-processing step rather than the spectroscopy technique itself. Therefore, in an attempt to further elucidate the underlying changes in the microstructure, we abandon the Fourier Transform approach and adopt (for the first time in the analysis of spectroscopic data) the Hilbert-Huang transform (HHT) through a sifting process, also known as Empirical Mode Decomposition (EMD) [61,62]. EMD deconvolves the signal into its Intrinsic Mode

Functions (IMF), whereas each IMF is monotonic, including the signal information at a single frequency component but still represented in terms of time. The first three IMFs of each investigated condition are represented in Figure 2.8, where it is essential to note that IMFs pertaining to high-frequency noise were omitted and replaced by the next mode.

Table 2.1: Summary of signal characteristics as a function of the applied voltage (mechanical stress) and estimated thickness (Δd_e is change in the thickness under the active electrode area and Δd_{os} change in the thickness at the observation site).

Applied potential (V)	**% Δd_e**	**pressure (kPa)**	**% Δd_{os}**	**Terahertz Amplitude (a.u.)**	**FWHM (ps)**	**Peak Rise Time (ps)**	**Delay (ps)**
0	0.00	0.00	0.00	0.8060	0.5113	0.3491	0.0700
250	0.04	-0.56	0.00	0.8039	0.5087	0.3460	0.0633
500	0.13	-2.25	0.04	0.8205	0.5071	0.3434	0.0667
750	0.29	-5.07	0.07	0.8249	0.5069	0.3441	0.0750
1000	0.50	-9.01	0.13	0.8279	0.5077	0.3441	0.0875
1250	0.80	-14.07	0.20	0.8272	0.5104	0.3451	0.0833
1500	1.16	-20.26	0.29	0.8310	0.5085	0.3459	0.0667
1750	1.61	-27.58	0.39	0.8331	0.5088	0.3464	0.0767
2000	2.14	-36.02	0.52	0.8325	0.5090	0.3457	0.0733
2250	2.75	-45.59	0.68	0.8361	0.5104	0.3452	0.0800
2500	3.48	-56.28	0.86	0.8365	0.5097	0.3453	0.0867
2750	4.32	-68.10	1.07	0.8380	0.5055	0.3439	0.0750
3000	5.30	-81.05	1.55	0.8511	0.5060	0.3492	0.0667

The resulting intrinsic mode functions shown in Figure 2.8 are the first three oscillation modes embedded in the signals. Generally, the first and second intrinsic mode functions of the THz-TDS signals exhibit distinct behaviors expressed by an individual wave packet centered approximately at 25 ps with notable changes in the attributes of each wave packet. The apparent increase in the amplitude of the wave in the first modes compared to the amplitude of the reference signal is attributed to the change in the index of refraction due to the presence of the VHB samples in the terahertz wave path. The shape and characteristics of the wave packet at 1250 V continue to support the previous observations of an inflection point in the response, where the wave packets at higher levels of stresses (i.e., voltage) are distinctively different from their low stresses counterparts. Finally, the third intrinsic mode function for the reference signal contains higher energy, whereas the 3rd IMFs of the VHB sample appear to represent the trend of the data rather than an oscillation mode. Indeed, the concentration of the energy in the first and second mode functions is in excellent agreement with the association of the conformational orders, as discussed above, given that higher frequencies (higher energy) are linked to lower-order modes. Future research will focus on establishing a strong correlation between the results of the IMFs and the optical and electrical properties of polymers.

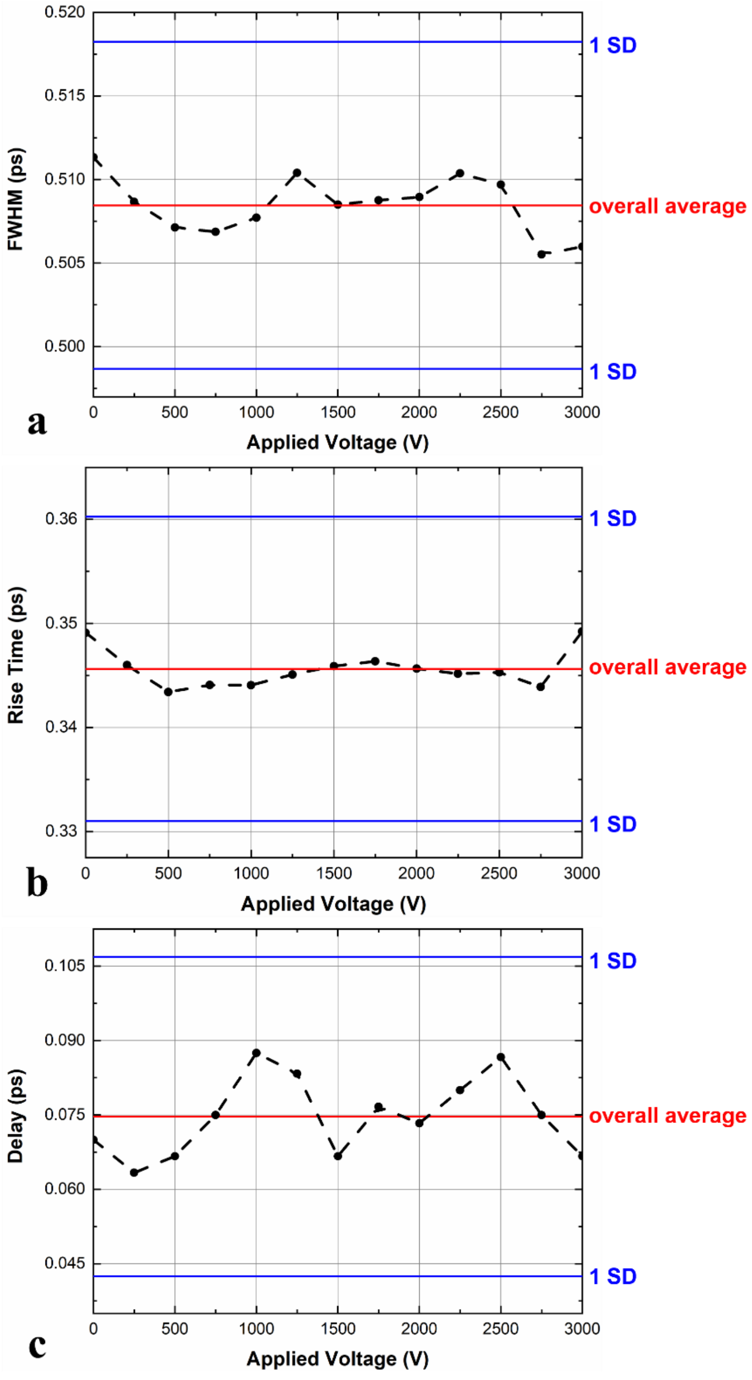

Figure 2.7: The temporal characteristics of the terahertz time-domain signals including (a) full-width at half-max (FWHM), (b) time rise, and (c) delay time of arrival based on data from Table 2.1.

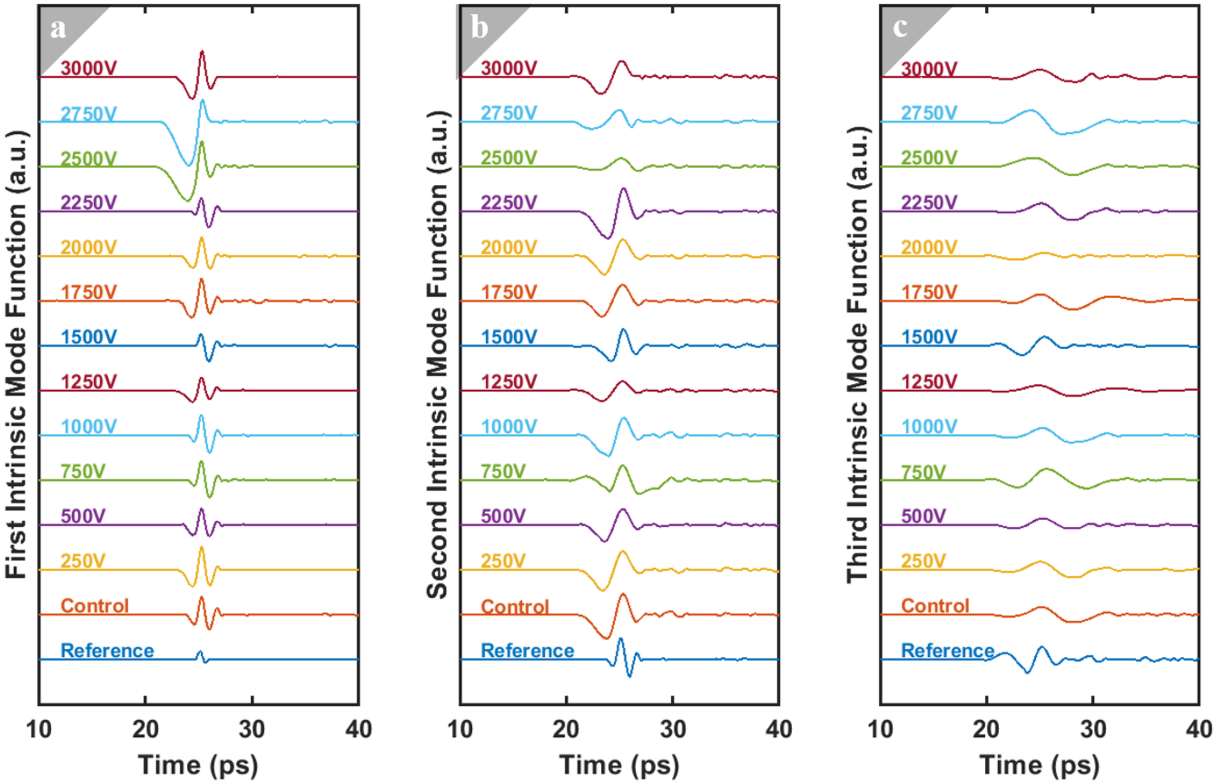

Figure 2.8: First (a), Second (b), and Third (c) intrinsic mode functions (high-frequency noise modes were omitted) of the THz time-domain signal elucidating the difference in the fundamental characteristics of the samples' waveforms as a function of applied voltage in comparison to the sample-free reference and zero-voltage conditions.

At the outset, using the DEA structure was found to be a reliable way to remotely apply a uniform state of stress without obscuring the observation site, hence, providing a pathway to non-invasively and non-destructively interrogate the polymer using non-contact terahertz time-domain spectroscopy technique. All reported loadings thus far were normal stresses due to the configuration of the active electrode area; however, the mechanical response of polymers has been shown to exhibit sensitivity to shear deformation due to the sliding and rearrangement of chains in response to mechanical work. To remedy this shortcoming of our approach, we propose a novel electrode area configuration that selectively gives rise to shear and normal stresses on the same or different locations within the same DEA structure. As discussed before, the actuation performance of the DEA is not the objective here but rather to use the coupling between electrostatic and mechanics to remotely and systemically apply mechanical stresses.

2.4 Conclusion

The eminence of polymers in a plethora of load-bearing engineering applications necessitates the fundamental understanding of the concurrent effect of stress on the conformational changes in the macromolecule. A new experimental mechanics framework was introduced to investigate the mechanical response of polymers using THz-TDS while the sample was under varying levels of stresses that were remotely controlled using an input voltage. A localized Maxwell stress due to the attraction of opposing polarity electrodes resulted in the expansion of the thickness of the unobscured remote observation area that was interrogated by terahertz waves. The results provide physical evidence on the effect of conformational changes of polymers through analyses of time-domain signals that signified changes in the optical properties of the sample (index of refraction). HHT was introduced to decompose the time-domain signals into its fundamental modes, hence, decoying the shortcomings of the current state-of-the-art analysis technique in the frequency domain. Future research will focus on the dynamic response of polymers by subjecting the samples to alternating mechanical stress as well as on establishing the predictive and correlative relationship between the output of the Hilbert-Huang transform and the optical properties of the material.

Acknowledgement

Chapter 2, in full, is a reprint of the material as it appears in Experimental Mechanics 2020. Huynh, Nha Uyen; Youssef, George, Springer, 2020. The dissertation author was the primary investigator and author of this paper.

References

1. Kremer, K. & Müller-Plathe, F. Multiscale simulation in polymer science. *Mol. Simul.* **28**, 729–750 (2002).

2. Gartner, T. E. & Jayaraman, A. Modeling and Simulations of Polymers: A Roadmap. *Macromolecules* **52**, 755–786 (2019).

3. Ngai, K. L. & Plazek, D. J. Identification of different modes of molecular motion in polymers that cause thermorheological complexity. *Rubber Chem. Technol.* **68**, 376–434 (1995).

4. Shenogina, N. B., Tsige, M., Patnaik, S. S. & Mukhopadhyay, S. M. Molecular modeling approach to prediction of thermo-mechanical behavior of thermoset polymer networks. *Macromolecules* **45**, 5307–5315 (2012).

5. Glotzer, S. C. & Paul, W. Molecular and mesoscale simulation methods for polymer materials. *Annu. Rev. Mater. Sci.* **32**, 401–436 (2002).

6. Frenkel, D. Simulations: The dark side. *Eur. Phys. J. Plus* **128**, (2013).

7. Bergstrom, J. *Mechanics of solid polymers theory and computational modeling*. *Elsevier* vol. 84 (Matthew Deans, 2015).

8. Arruda, E. M. & Boyce, M. C. A three-dimensional constitutive model for the large stretch behavior of rubber elastic materials. *J. Mech. Phys. Solids* **41**, 389–412 (1993).

9. Flory, P. J. *Principles of Polymer Chemistry*. *Journal of AOAC INTERNATIONAL* vol. 49 (Cornell Unversity Press, 1953).

10. Bower, A. F. *Applied Mechanics of Solids*. (CRC Press, 2010).

11. Timoshenko, S. & Goodier, J. N. Theory of Elasticity. *The Mathematical Gazette* vol. 51 (1951).

12. Youssef, G. & Gupta, V. Dynamic response of polyurea subjected to nanosecond rise-time stress waves. 317–328 (2012) doi:10.1007/s11043-011-9164-7.

13. Youssef, G. & Gupta, V. Dynamic tensile strength of polyurea. *J. Mater. Res.* **27**, 494–499 (2012).

14. *Springer Handbook of Experimental Solid Mechanics*. (Springer Science+Business Media, 2008).

15. Kornbluh, R. D., Pelrine, R. E. & Joseph, J. Elastomeric dielectric artificial muscle actuators for small robots. *Proc. Mater. Res. Soc. Symp.* **600**, 119–130 (1995).

16. Pelrine, R. E., Kornbluh, R. D. & Joseph, J. P. Electrostriction of polymer dielectrics with compliant electrodes as a means of actuation. *Sensors Actuators, A Phys.* **64**, 77–85 (1998).

17. Kornbluh, R., Pelrine, R., Joseph, J., Pei, Q. & Chiba, S. Ultra-high strain response of elastomeric polymer dielectrics. *Mater. Res. Soc. Symp. - Proc.* **600**, 119–130 (2000).

18. Full, J. & Meijer, K. Artificial muscles versus natural actuators from frogs to flies. **3987**, 2–9 (2000).

19. Harris, D. & Bertolucci, M. *Symmetry and Spectroscopy*. (Oxford University Press,Inc., 1978).

20. Siesler, H. W. & Holland-Moritz, K. *Infrared and Raman Spectroscopy of Polymers*. (Marcel Dekker, Inc., 1980).

21. Koenig, J. L. *Spectroscopy of Polymers-*. (American Chemical Society, 1992).

22. Götz, A., Nikzad-Langerodi, R., Staedler, Y., Bellaire, A. & Saukel, J. Apparent penetration depth in attenuated total reflection Fourier-transform infrared (ATR-FTIR) spectroscopy of Allium cepa L. epidermis and cuticle. *Spectrochim. Acta - Part A Mol. Biomol. Spectrosc.* **224**, 1–6 (2020).

23. Gaigneaux, A. & Goormaghtigh, E. A new dimension for cell identification by FTIR spectroscopy: Depth profiling in attenuated total reflection. *Analyst* **138**, 4070–4075 (2013).

24. Lee, Y. S. *Principles of terahertz science and technology*. *Principles of Terahertz Science and Technology* (2009). doi:10.1007/978-0-387-09540-0.

25. Coutaz, J.-L., Garet, F. & Wallace, V. P. *Principles of Terahertz Time-Domain*

Spectroscopy. (Pan Stanford Publishing Pte. Ltd., 2018).

26. *Handbook of terahertz technology for imaging, sensing and communications*. *Osmania Journal of Social Sciences* (Woodhead Publishing, 2013).

27. *Terahertz Spectroscopy: Principles and Applications*. *Terahertz Spectroscopy* (Taylor & Francis, 2008). doi:10.1201/9781420007701.

28. Terao, W. *et al.* Boson peak dynamics of natural polymer starch investigated by terahertz time-domain spectroscopy and low-frequency Raman scattering. *Spectrochim. Acta - Part A Mol. Biomol. Spectrosc.* **192**, 446–450 (2018).

29. Iijima, Y. *et al.* Terahertz Time-Domain Spectroscopy and Low-Frequency Raman Scattering of Boson Peak Dynamics of Lithium Borate Glasses. *Int. Conf. Infrared, Millimeter, Terahertz Waves, IRMMW-THz* **2018-Septe**, 4–5 (2018).

30. Bank, M. I. & Krimm, S. Lattice studies of cristalline strucure of polyethylene. *Journal of Applied Physics* vol. 39 4951 (1968).

31. Fuse, N. *et al.* Observation and analysis of molecular vibration modes in polylactide at terahertz frequencies. *Jpn. J. Appl. Phys.* **49**, 1024021–1024028 (2010).

32. Podzorov, A. & Gallot, G. Density of states and vibrational modes of PDMS studied by terahertz time-domain spectroscopy. *Chem. Phys. Lett.* **495**, 46–49 (2010).

33. Hoshina, H. *et al.* Higher order conformation of poly(3-hydroxyalkanoates) studied by terahertz time-domain spectroscopy. *Appl. Phys. Lett.* **96**, 3–6 (2010).

34. Hoshina, H. *et al.* Polarization and temperature dependent spectra of poly(3-hydroxyalkanoate)s measured at terahertz frequencies. *Phys. Chem. Chem. Phys.* **13**, 9173–9179 (2011).

35. Neu, J., Nikonow, H. & Schmuttenmaer, C. A. Terahertz Spectroscopy and Density Functional Theory Calculations of dl -Norleucine and dl -Methionine. *J. Phys. Chem. A* **122**, 5978–5982 (2018).

36. Neu, J. *et al.* Terahertz Spectroscopy of Tetrameric Peptides. *J. Phys. Chem. Lett.* **10**, 2624–2628 (2019).

37. Neu, J. & Schmuttenmaer, C. A. Terahertz Spectroscopy and Density Functional Theory Investigation of the Dipeptide L-Carnosine. *J. Infrared, Millimeter, Terahertz Waves* (2020) doi:10.1007/s10762-019-00636-7.

38. Kister, G., Cassanas, G. & Vert, M. Effects of morphology, conformation and configuration on the IR and Raman spectra of various poly(lactic acid)s. *Polymer (Guildf).* **39**, 267–273 (1998).

39. Cunningham, P. D. *et al.* Broadband terahertz characterization of the refractive index and absorption of some important polymeric and organic electro-optic materials. *J. Appl. Phys.* **109**, 0–5 (2011).

40. Zhao, Y. *et al.* Intermolecular vibrational modes and H-bond interactions in crystalline urea investigated by terahertz spectroscopy and theoretical calculation. *Spectrochim. Acta - Part A Mol. Biomol. Spectrosc.* **189**, 528–534 (2018).

41. Wietzke, S. *et al.* Terahertz time-domain spectroscopy as a tool to monitor the glass transition in polymers. **17**, 19006–19014 (2009).

42. Youssef, G. & Huynh, N. U. Integrated Temperature-Controlled, Ultrahigh Strain Rate Loading, and Spectroscopy Apparatus for Dynamic Characterization of Materials.

43. Plante, J. S. & Dubowsky, S. Large-scale failure modes of dielectric elastomer actuators. *Int. J. Solids Struct.* **43**, 7727–7751 (2006).

44. Wissler, M. Modeling Dielectric Elastomer Actuators. (Swiss Federal Institute of Technology in Zurich, 2007).

45. Scheller, M. Data extraction from terahertz time domain spectroscopy measurements. *J. Infrared, Millimeter, Terahertz Waves* **35**, 638–648 (2014).

46. Dhillon, S. S. *et al.* The 2017 terahertz science and technology roadmap. *J. Phys. D. Appl. Phys.* **50**, (2017).

47. Li, X., Hong, Z., He, J. & Chen, Y. Precisely optical material parameter determination by time domain waveform rebuilding with THz time-domain spectroscopy. *Opt. Commun.* **283**, 4701–4706 (2010).

48. Scheller, M. Real-time terahertz material characterization by numerical three-dimensional optimization. *Opt. Express* **19**, 10647 (2011).

49. Bernier, M., Garet, F. & Coutaz, J. L. Precise determination of the refractive index of samples showing low transmission bands by THz time-domain spectroscopy. *IEEE Trans. Terahertz Sci. Technol.* **3**, 295–301 (2013).

50. Duvillaret, L., Garet, F. & Coutaz, J.-L. Highly precise determination of optical constants and sample thickness in terahertz time-domain spectroscopy. *Appl. Opt.* **38**, 409 (1999).

51. Naito, K., Kagawa, Y., Utsuno, S., Naganuma, T. & Kurihara, K. Dielectric properties of woven fabric glass fiber reinforced polymer-matrix composites in the THz frequency range. *Compos. Sci. Technol.* **69**, 2027–2029 (2009).

52. Fischer, B. M. *et al.* Investigating material characteristics and morphology of polymers using terahertz technologies. *IEEE Trans. Terahertz Sci. Technol.* **3**, 259–268 (2013).

53. Fedulova, E. V. *et al.* Studying of dielectric properties of polymers in the terahertz frequency range. *Saratov Fall Meet. 2011 Opt. Technol. Biophys. Med. XIII* **8337**, 83370I (2012).

54. Wietzke, S. *et al.* Terahertz spectroscopy on polymers : A review of morphological studies. *J. Mol. Struct.* **1006**, 41–51 (2011).

55. Jepsen, P. U. & Fischer, B. M. Dynamic range in terahertz time-domain transmission and reflection spectroscopy. *Opt. Lett.* **30**, 29 (2005).

56. Withayachumnankul, W., Fischer, B. M. & Abbott, D. Material thickness optimization for terahertz time-domain spectroscopy. *Opt. Soc. Am.* **16**, 7382–7396 (2008).

57. Withayachumnankul, W., Fischer, B. M., Lin, H. & Abbott, D. Uncertainty in terahertz time-domain spectroscopy measurement. *J. Opt. Soc. Am. B* **25**, (2008).

58. Pupeza, I., Wilk, R. & Koch, M. Highly accurate optical material parameter determination with THz time-domain spectroscopy. **15**, 1598–1609 (2007).

59. Yeoh, O. H. Some forms of the strain energy function for rubber. *Rubber Chemistry and Technology* vol. 66 754–771 (1993).

60. Data, T. VHB ^{TM} Tapes Product Description : (2011).

61. Huang, N. E. *et al.* On instantaneous frequency. *Adv. Adapt. Data Anal.* **1**, 177–229 (2009).

62. Huang, N. E. & Shen, S. *Hibert-Huang Transform and Its Applications*. (World Scientific Publishing Co. Pte. Ltd., 2014).

CHAPTER 3

Spectro-microscopic Characterization of Elastomers Subjected to Laser-induced Shock Waves

Nha Uyen Huynh, Carlos Gamez, and George Youssef*

Experimental Mechanics Laboratory, Mechanical Engineering Department, San Diego State University, 5500 Campanile Drive, San Diego Ca 92182

Abstract

The core of this research study is separated into three domains, the ultrahigh strain rate response of elastomeric polymers, laser-induced shock waves, and terahertz time-domain spectroscopy, which marks a multiscale characterization of the intrinsic mechanical and structural attributes of polymers. Elastomers, e.g., polyurea, constitute a scientific and technological class of materials suitable for many applications, specifically in high impact loading scenarios, where the macromolecule may endure large extensibility under ultrahigh strain rates. Thus, a laser-induced shock wave (LSW) experimental technique was used to investigate the mechanical response. LSW can submit the samples to a strain rate exceeding 10^6 s^{-1} at low strains (<<1%), enabling the determination of the intrinsic failure modes and strength of the material. Moreover, the large deformation induced during shock loading may alter the macromolecule structure, which can only be detected spectroscopically. Therefore, this research incorporated terahertz (THz) bulk spectroscopy to detect and report any molecular conformational changes, even if samples did not catastrophically fail. Finally, microscopy techniques (atomic force microscopy AFM, and scanning electron microscopy, SEM) were used to elucidate changes in the microscale properties, morphology, and topography. The interpretation of the results explicated brittle failure in terms of partial and total spallation, as a function of laser intensity (shock wave), and ductile failure leading to plastic deformation. Remarkably, several failure modes have been documented, including inelastic deformation, plastic bulging, and adiabatic shearing, not previously associated with laser spallation technique. Furthermore, the spectral changes found in the THz regime between the pre- and post-loaded samples substantiated the validity of terahertz spectroscopy in elucidating the underlying mechanism associated with the impact mitigating properties of dynamically loaded polyurea. At the outset, we highlight several fundamental mechanisms responsible for the observed failure modes and propose an approach to further improve the response of elastomers-coated armor.

Keywords: ultrahigh strain loading, terahertz wave, THz-TDS, plastic deformation, adiabatic shearing, impact mitigation, shock waves

***Corresponding Author: gyoussef@sdsu.edu**

3.1 Introduction

Polyurea, a thermoset elastomer, has been persistently investigated for several civilian and military applications over the past two decades, including protection of mobile and fixed military assets from shock loading, civilian infrastructure from weathering conditions, and humans from biomechanical impact loading [1]. Its integration in such applications (only a few examples were given) is attributed to the superior mechanical and physical properties, including impact mitigation, moisture and chemical resistance, and significant tearing elongation [2–6]. In general, the property profile of polyurea situates it as a competitive engineering material candidate. Of specific interest here is the superior impact mitigation properties of polyurea, which draws considerable attention from the materials and mechanics research community. For example, Barsoum *et al.* demonstrated that adding a 2-3 mm thick layer of polyurea on top of a steel armor plate significantly improved its blast resistance in an underwater explosion [4]. Studies with a focus on characterizing the mechanical response over a wide range of loading conditions, with emphasis on strain rate behavior, have flourished since the work of Barsoum [2,7–11].

Generally, projectiles released as a result of an explosion can reach speeds ranging from 2750 $m\cdot s^{-1}$ to 9150 $m\cdot s^{-1}$, and the impact of these projectiles can load a protective armor or biological material in the 10 to 100 ns timeframe [12–15]. The material sustains high peak stresses and small strains during this timeframe; however, the strain rates are extremely high [12]. Multiple techniques have been used to achieve such high strain rate loading conditions to replicate the same loading time in a laboratory environment. For example, Sarva *et al.* used a split-Hopkinson pressure bar (SHBP) test setup to report the mechanical behavior of polyurea when subjected to uniaxial compression loading at strain rates of 0.01 s^{-1} to 7500 s^{-1} [16]. They found a strong dependence of the stress-strain behavior on the strain rate and how the behavior of polyurea changes gradually, changing from rubbery to leathery (low rates ∼0.001 s^{-1}) then to glassy behavior (high rates ∼5000 s^{-1}) with increasing strain rate. Jiao *et al.* studied the pressure dependence of polyurea shearing resistance at a high strain rate ranging from 10^5 to 10^6 s^{-1} using a plate impact experiment [17]. They demonstrated that for pressures ranging from 0.3 GPa to 3 GPa, the shearing resistance of polyurea is quite insensitive to the shearing rate near 10^5 s^{-1} but increases substantially with increasing pressure. Youssef *et al.* used the Laser-induced Shock Wave (LSW) technique to generate the ultrahigh strain rate loading a technique optimized for measuring the tensile strength of thin-film interfaces by Gupta *et al*. and Wang *et al.* [18–20]. The measured dynamic tensile strength of polyurea was found to be 93.1±5 MPa at an ultrahigh strain rate of 1.67×10^7 s^{-1}. Jain *et al.* also used the laser spallation technique to evaluate the dynamic tensile strength at the interfaces in the E-glass composite/polyurea/Al6XN Stainless steel joint structure [21]. They found that the steel/polyurea interface had a dynamic tensile strength of 486±20 MPa compared to 370±20 MPa of the E-glass/polyurea interface. In the same study, Jain *et al*. concluded that the tensile strength of the E-glass/polyurea interface was barely affected after it was exposed for 30 days to a 90%RH and 50 °C environment [21].

A byproduct of the previous studies is the pursuit of explicating the underpinning mechanisms contributing to the superior impact mitigating properties of polyurea undergoing mechanical loading. Different mechanisms have been suggested to explain how the performance of polyurea-coated structures is enhanced in withstanding impacts from hypervelocity projectiles [2,11,22]. The transition of polyurea from the rubbery to the glassy state under high strain rate loading resulted in a brittle failure accompanied by significant energy dissipation, improving the shock performance of elastomer-coated armors [23]. Moreover, the difference in the mechanical properties of polyurea with respect to the under armor plate implies a reduced transmitted wave due to the impedance mismatch, while the viscoelastic properties and the geometrical attributes of the polyurea coating along with its segmental microstructure assist in shock wave dispersion [3,11,24–26]. Nonetheless, there is a lack of fundamental understanding of the underlying energy absorption, attenuation, and divergence mechanisms of polymers with superior shock tolerant properties over a broad range of strain rates. The lack of linking the mechanical behavior of dynamically loaded polyurea and microstructural evolutions is due to the current state-of-the-art postmortem characterization limitations.

The gap in knowledge limits the development of polymer-based, shock-tolerant structures to incremental rather than transformative advances. In the current state-of-the-art, the mechanical properties of polymers undergoing ultrahigh strain rate dynamic response are extracted using postmortem, i.e., after failure, characterization techniques [27,28]. Despite the valuable information the current state-of-the-art can provide, there lacks an experimental technique to elucidate the intrinsic mechanical behavior of impact mitigating polymers, such as polyurea. Here, terahertz spectroscopy is introduced as a possible bulk spectroscopic technique for the characterization of polymeric material systems. Therefore, the results and experimental framework herein lays the groundwork for utilizing this technology in the future to characterize polymer in-situ ultrahigh strain rate loading. Terahertz spectroscopy uses electromagnetic radiation in frequencies ranging from 0.1 to 10 THz to detect and observe changes in the optical properties of organic materials and is suitable for probing collective intra- and intermolecular vibrational modes of solids in the low-frequency regime. In recent studies, terahertz radiation has been implemented in various applications, ranging from the investigation of material properties to quality assurance to biomedical diagnostics [29,30]. Terahertz-based spectroscopy departs from its predecessors in the infrared region, such as Fourier transform infrared spectroscopy, by enabling spectroscopic interrogations of bulk polymers rather than the surface layer, as with FTIR-ATR which is limited to 2 µm [31,32]. Comparison with other spectroscopies has been listed in [33], which is omitted from this paper for brevity. Moreover, Duvillaret *et al.* introduced a reliable novel method in simultaneously extracting the optical properties and geometry of materials using terahertz time-domain spectroscopy (THz-TDS) [34]. The resulting methodology was applicable for real-time parameter extraction of various materials with different thicknesses without simplifying assumptions, undermining the resolved outcomes [34]. Our previous publication observed changes in the terahertz spectra as a function of applied stress, further substantiating the potential of bulk terahertz spectroscopy in delineating stress-induced structural changes [33]. In all, terahertz spectroscopy has many advantages, the prime of which is the transparency of polymers and the capability for nondestructive evaluation in the terahertz region of the electromagnetic spectrum, exemplifying the viability of terahertz spectroscopy for explicating the fundamental intrinsic mechanical behavior of impact mitigating polymers.

This research aims to characterize the dynamical response of polyurea under ultrahigh strain rate loading using spectroscopic and microscopic approaches. Thus, terahertz spectroscopy operated in the transmission mode was used to characterize the spectral changes in thin-film polyurea as a function of laser-induced shock waves with different intensities. In addition, scanning electron and atomic force microscopes were also used to characterize the shock-loaded polyurea.

3.2 Materials and Methods

Thin films of polyurea were prepared using a spin coating process. A 15 mL mixture of oligomeric diamine (EVONIK Versalink® P-1000) and isocyanate (Lupranate® 5143 Isocyanate) with a ratio of 4:1 was first slowly stirred to avoid entrapment of air bubbles. The mixture was then transferred to the top of the casting substrate (polypropylene wafer) and left undisturbed for 7 min before it was spun at 250 RPM to achieve a nominal thickness of 250 μm. The polyurea film was cured at ambient conditions for 24 h before vacuum oven cured for an additional 24 h at 80 °C. It was found that the polyurea film can be easily removed from the polypropylene substrate without the need of a releasing agent. A total of four films were prepared, where five sets of samples were extracted for subsequent loading and characterization. The following subsections detail the experimental protocol, where the laser-induced shock waves technique was used to load the elastomeric samples at ultrahigh strain rate. The structural and morphological of the samples were then investigated using bulk spectroscopy and various microscopies.

3.2.1 Laser-induced Shock Wave Loading

Each polyurea sample was mechanically loaded at eight different locations, where each location was loaded only once with an ultrahigh strain rate stress wave generated using a high-energy laser (Spectra-Physics, Quanta-Ray PRO 350). The typical laser setup, also called the laser spallation technique, was used to generate an input stress-time profile with the highest amplitude and shortest rise time. However, the current research study necessitated the detachment of the sample from the loading structure for post-loading characterization without interrupting the polyurea sample conditions. Therefore, the laser spallation technique was modified (Figure 3.1) to allow the on-demand detachment of the polyurea samples to facilitate subsequent characterizations

(THz-TDS, AFM, nanoindentation, and SEM, discussed next). A 3 mm diameter, high-intensity spot size beam (from the high-energy laser) interacted with a 0.5 μm thick sacrificial aluminum layer (sputtered in-house using Quorum Q150T turbomolecular coater), which underwent a rapid thermal expansion, inducing a compressive stress wave with a few nanoseconds rise-time. On one side of the sacrificial layer, a 1 mm glass slide (incident to the beam) was used to confine the thermal expansion of the aluminum film upon interaction with the high-energy laser beam. In other words, the aluminum sacrificial film was first deposited on the glass slide. A thin (~50-100 μm) stiff layer of waterglass (Science Company) was applied on the opposite side of the sacrificial layer, acting as additional confinement of the aluminum thermal expansion. A secondary confinement layer was necessary due to the on-demand detachment requirement imposed on this experiment to facilitate the post-loading terahertz-based spectroscopic characterization, while maintaining unified stress wave attributes from one measurement to the other. Therefore, the glass slide, the sacrificial layer, and the waterglass layer comprised the stress wave generation sandwich structure (Figures 3.1b and 3.1c). To satisfy the on-demand detachment requirement, a water-soluble, viscous medium was then used to couple the sample with the stress wave generation sandwich structure. Subsequently, a fresh polyurea spot was loaded with a different laser energy level, ranging from 500 mJ to 2250 mJ at an increment of 250 mJ. It is worth noting that the newly introduced stress generation sandwich structure resulted in launching a secondary load trailing the initial high strain rate compressive stress wave, i.e., a byproduct of the modified LSW technique. That is, the glass slide over-constrained the laser-induced plasma, generating a second pressure build-up leading to the sample, discussed later.

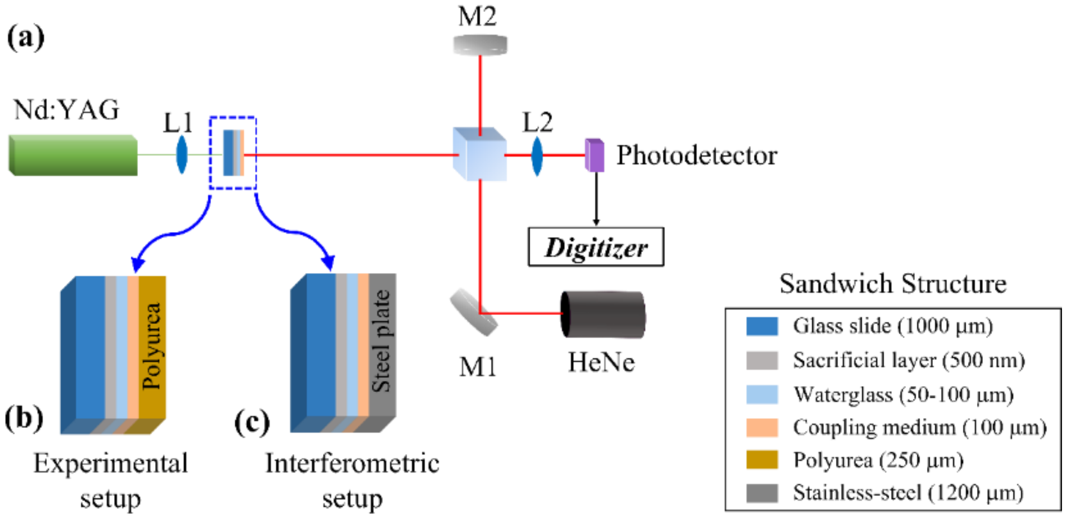

Figure 3.1: Schematic of (a) the laser-induced Shock wave testing apparatus including a Michelson interferometry to measure the free surface displacement, (b) the sandwich structure used in generation of shock waves with a mounted polyurea sample, and (c) stress generation sandwich structure with a reflective stainless-steel plate to facilitate the free surface displacement measurements.

Doppler/Michelson interferometric (Figure 3.1a) measurements were performed at each energy level corresponding to laser energies ranging from 500 mJ to 2250 mJ to quantify the attributes of the input stress wave generated by the interaction between the laser and the aluminum ablation layer. For the interferometric measurements, the polyurea sample was replaced with a ~1.2 mm steel plate to ensure the stimulation of a displacement, but not deformation, on the reflective free surface (Figure 3.1c). Optical fringes corresponding to the free surface displacement with a resolution of 25 ps and 200 ns total duration were recorded in single-shot mode using a signal digitizer (Tektronix DPO 7254). The interferometric data was used to obtain a transient free surface displacement profile, $u_o(t)$, by first deducing the distance traveled by the free surface, $d = m\lambda_0/2$ [35] where m is the number of fringes and λ_0 is the wavelength (632.8 nm) of the stabilized HeNe laser source (Newport, N-STP-912). The fringe-displacement data was then fitted into Eqn. 1 using a nonlinear least square method with multiple start points algorithm utilizing the

Global Optimization Toolbox in MATLAB® to extract the three fitting parameters α, β, and γ that mathematically define Eqn. 3.1.

$$u_o(t) = \gamma\left\{-\alpha\left[e^{-t/\alpha} - 1\right] + \beta\left[e^{-t/\beta} - 1\right]\right\} \tag{3.1}$$

The displacement-time history calculated from Eqn. 1 was used to calculate the free surface velocity by taking the derivative of $u_o(t)$ with respect to time, arriving at

$$v_o(t) = \gamma\left\{e^{-t/\alpha} - e^{-t/\beta}\right\}. \tag{3.2}$$

Equation 3.1 is the integration of Eqn. 3.2, where γ is the maximum velocity while α and β define the rise and decay of the exponential terms that describe the velocity profile phenomenologically [36].

Finally, the transient input stress triggering the measured free surface displacement of the substrate is determined using [19,37–39]

$$\sigma_i = -\tfrac{1}{2}\rho c v_o(t) \tag{3.3}$$

where, ρ and c are the density and the speed of sound in the stainless-steel substrate, respectively, taken to be 7999 $\text{kg}\cdot\text{m}^{-3}$ and 5728 $\text{m}\cdot\text{s}^{-1}$ [40]. Figure 3.2 presents a summary of the interferometric procedure used to obtain the input stress profile (Figure 3.2c) from the fringe record (Figure 3.2a).

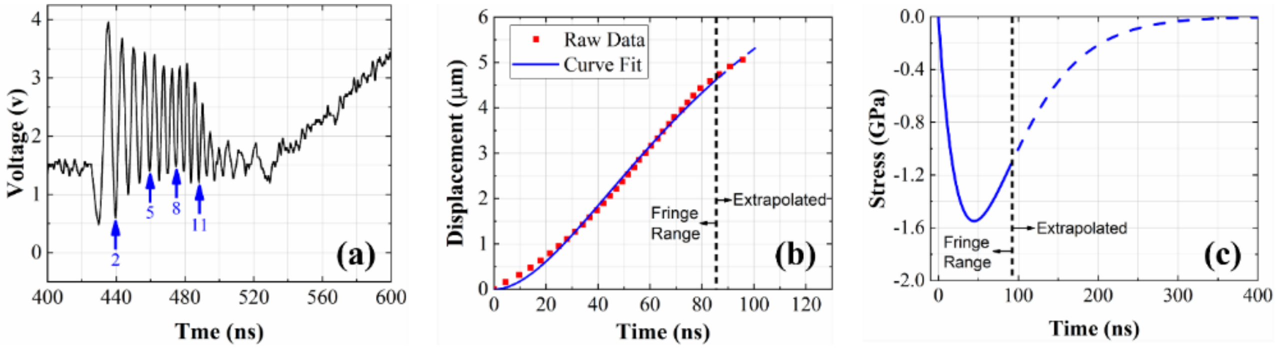

Figure 3.2: Extraction of the input stress from the interferometric data at an energy level of 2250 mJ. (a) The raw fringe record collected by the digitizer using Michelson interferometry and were manually counted (indicated by the blue arrows), (b) the free surface displacement profile resolved from (a) using $d = m\lambda_0/2$ and fitted in Eqn. 1, resulting in γ=1067 m·s^{-1}, α=48.04 ns, and β=40.52 ns, and (c) the input stress profile obtained using Eqn. 3.

Since the free surface of the polyurea sample is optically diffusive and is kept coating-free to facilitate post-loading spectroscopic interrogation, the reported stress profiles (e.g., Figure 3.2c) are based on the interferometric measurements of the steel plate. Therefore, the transmitted input stress to the polyurea samples from the coupling layer was calculated by modifying Eqn. 3.3 by the transmission of an incident stress wave to a different medium [41].

$$T_p = \frac{T_{cm\to p}}{T_{cm\to s}} = \frac{(\rho_p c_p)(\rho_{cm} c_{cm} + \rho_s c_s)}{(\rho_s c_s)(\rho_{cm} c_{cm} + \rho_p c_p)} \tag{3.4}$$

Where, $T_{cm\to p}$ and $T_{cm\to s}$ are the transmission coefficient from the coupling medium (cm) to the polyurea sample (p) and the coupling medium to the steel substrate (s), respectively, ρ_p (1071 kg.m^{-3}) is the density of polyurea, ρ_s is the density of steel, c_p (1750 m·s^{-1}) [42] and $c_s$is the speed of sound in polyurea and steel, respectively. The coupling medium was taken to be a 90% aqueous solution, with ρ_{cm} 1431 kg.m^{-3} and c_{cm} 1974 m.s^{-1} [43]. The frequency of a stress wave traveling through two different media was assumed to be the same to adjust for the wavelength [44]. Therefore, the wave speed ratio, $a = c_s/c_p$, between steel and polyurea was calculated to scale the loading time to obtain the input stress in polyurea using

$$\sigma_p(t) = T_p \sigma_s(a.t) \tag{3.5}$$

where, σ_s is the stress input in steel.

3.2.2 Microscopy Characterization

The propagation of the laser-induced shock waves may lead to different failure modes, depending on the cohesion strength and presence of defects or imperfections compared to the amplitude of the stress wave. A microscopy characterization protocol was used to identify and classify the different failure modes. Atomic force microscope (AFM) and scanning electron microscope (SEM) were used to elucidate the surface topography and morphology of the loaded sites, respectively. A 50×50 µm area was mapped using the AFM (AFM Workshop TT-2) to obtain the topography in the tapping mode and the local modulus using the force-displacement mode. The examined area was located at the center of the loaded region, identified using the sample holder and location template shown in the inset of Figure 3.3. For the nanoindentation measurements, close contact tips (k = 26 N/m, f_0 = 160 kHz, AFM Workshop, ACLA-10) were used to indent the polyurea with a maximum force of 3.5 µN, while simultaneously measuring the indentation depth. That is to say; the measurements were done in force-controlled mode. The data was analyzed according to the Oliver and Pharr model using Eqn. 3.6 [45].

$$E = \frac{0.18 S^2 E_i \ (1-\nu^2)}{(h_{max} S - \varepsilon P_{\max}) E_i - 0.18 S^2 \ (1-\nu_i{}^2)} \tag{3.6}$$

Where, E_i is the modulus and ν_i is the Poisson's ratio of the silicon indenter, taken to be 170 GPa and 0.27, respectively. E is the modulus and ν is the Poisson's ratio of the material under investigation (i.e., polyurea taken to be 0.486 based on [46]), while S is the slope of the load-elastic displacement curve. ε is a geometry-based constant of the indenter (in this case was pyramidal), P_{max} is the maximum load applied, and h_{max} is the maximum indentation depth. The local modulus in the next section is an average of at least 16 different nanoindentation events. Finally, the morphology of the surface and cross section of the samples were captured using an SEM (FEI, Quanta 450). Before placement in the microscope, the polyurea samples were clamped onto a 3D-printed mount and coated with 6 nm of platinum. SEM micrographs were obtained at 10-20 kV and a 10 mm working distance.

3.2.3 Terahertz Time-Domain Spectroscopy (THz-TDS)

The novelty of this research was the pursuit of a suitable material interrogation technique to delineate the correlation between the structural changes and load-induced morphological or mechanical changes in the material. Terahertz time-domain spectroscopy (THz-TDS) was used to examine the polyurea samples, where the measurements were collected within 24 h after laser-induced shock wave loading. Figure 3.3 is a schematic of the THz-TDS in the transmission mode (refer to [33] for experimental setup details). Here, a new sample holder (i.e., mask) was designed to repeatedly interrogate the exact spot on each sample pre- and post-loading; hence, the reported structural changes are only due to the shock loading.

The spectral analysis was performed to detect the frequencies corresponding to the structural peaks of polyurea. The spectral analysis was based on the frequency-domain transfer function, calculated as the ratio of the fast Fourier transform of the sample and reference signals (Eqn. 3.8).

$$H_{meas}(k) = \frac{\sum_{j=1}^{n} S(j) e^{[-2\pi i*(j-1)*(k-1)]/n}}{\sum_{j=1}^{n} R(j) e^{[-2\pi i*(j-1)*(k-1)]/n}} \tag{3.8}$$

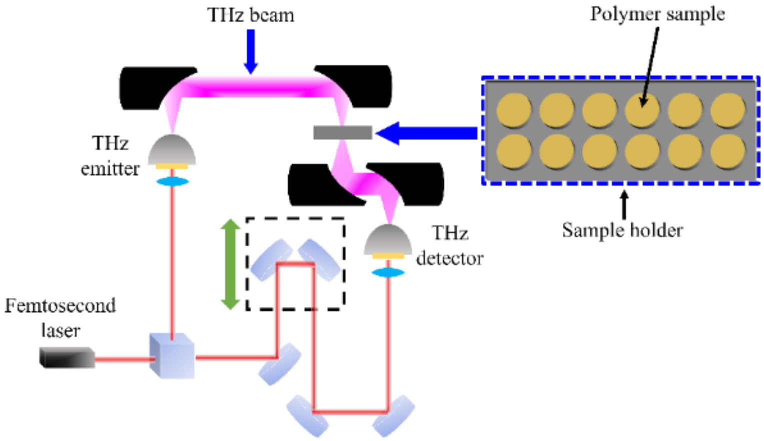

Figure 3.3: In-house developed terahertz time-domain spectroscopy setup, demonstrating the basic transmission mode with elastomer sample placed at the focal point between two parabolic mirrors using a specifically developed sample holder to ensure repeatability.

3.3 Results and Discussion

The following subsections examine the results based on the experimental protocol discussed above. First, the reported input stress wave profile based on the interferometric measurements demonstrated the viability of the modified LSW to induce elongated stress waves with higher peak stress. Second, the microscopic characterizations showed inelastic ductile deformations that have yet to be uncovered in laser-induced shock wave experiments. Finally, terahertz measurements were used to relate intermolecular motions of hydrogen bonds to the failure modes, explicating an interdependence with the increasing laser intensity.

3.3.1 Laser Intensity - Stress Relationship

The experimental setup shown in Figure 3.1 indicates that the attributes of the stress wave, later submitted onto the test material, hinged on the interactions between the laser pulse and the sacrificial and confinement layers. Analysis of the interferometric data yielded the input stress profiles (Eqn. 3.3) at eight different energy levels. These stress wave profiles were resolved from the interferometric data measured off the stainless-steel free surface. The peak of the input stress due to the stress wave propagation in the stainless-steel substrate ranges from ~1.0 GPa to 1.7 GPa, corresponding to laser energies of 500 mJ to 2250 mJ. It is important to note that stainless-steel was used to resolve the stress profiles, given its high reflectivity and stiffness. However, the test setup used in this experiment (Figure 3.1b) relied on mounting the polyurea samples on the test sandwich structure using a coupling medium, requiring the conversion of the steel-based stresses to the polyurea counterpart. Therefore, the input stress wave profiles for the polyurea samples were resolved using Eqn. 3.5 and are plotted in Figure 3.4a, accounting for the transmission coefficient and the wave speed ratio. Consequently, the input stress to the polyurea range between 0.43 GPa to 0.73 GPa, corresponding to the eight different laser intensities. Figure 3.4b is a plot of the average peak stress, also showing the statistical variance of the peak stress based on the analysis of three datasets collected at each energy level. Notably, the peak stress at 2000 mJ is interpolated from the rest of the intensity-stress data due to experimental difficulties in obtaining interferometric data at this energy level. It is thought that such difficulties arose from the potential coincidence of internal resonance within the steel substrate with the frequency content of the laser-induced shock wave, a topic for future investigations.

The stress-energy interrelationship shown in Figure 3.4b can be divided into four regions. At low laser energy levels, ranging between 500 mJ and 750 mJ, the peak stress maintained an average of 0.43 GPa, defining Region I. Subsequently, in Region II, at laser energies between 750 mJ and 1250 mJ, the average peak stress ascended at a rate of 0.47 $\mathrm{MPa \cdot mJ^{-1}}$, leading to another region of energy levels where the peak stress was invariant with respect to increasing laser intensity. This Region III extended between 1250 mJ and 1750 mJ. Finally, the peak stress started to ascend again at a slower rate of 0.14 $\mathrm{MPa \cdot mJ^{-1}}$ in Region IV, up to the maximum energy level of 2250 mJ. In general, the attributes of the stress wave are a function of the type of sacrificial material, the properties of the substrate, the laser wavelength, the pulse width, the laser intensity, and the thicknesses of the different layers within the sandwich structure. Of these parameters, the first four remained unchanged throughout the experiment: the deposited thin-film aluminum, stainless-steel, 1064 nm, and ~10 ns, respectively. Therefore, the spread in the peak stress at each energy level is attributed to the variance in the thicknesses of the aluminum sacrificial layer, waterglass confining layer, or the coupling medium. The absorption of the laser beam by the sacrificial layer ultimately defines the amplitude of the stress wave, where the amount of absorbed light by the aluminum is dependent on the absorptivity of aluminum and the depth of penetration [38]. That is, the current thickness of the aluminum absorbing layer was previously optimized for a specific range of energy levels, well below those used herein [47]. In Region I, the depth of penetration appeared to be independent of the intensity, resulting in nearly the same peak stress. Alternatively, the penetration depth increased with respect to the laser intensity in Region II. Finally, the penetration depth approached the thickness of the sacrificial layer, resulting in a minimal variation in the peak stress in the last two regions. Notably, the onset of Region III in Figure 3.4b represents the threshold, at which all failures are reported, as discussed next.

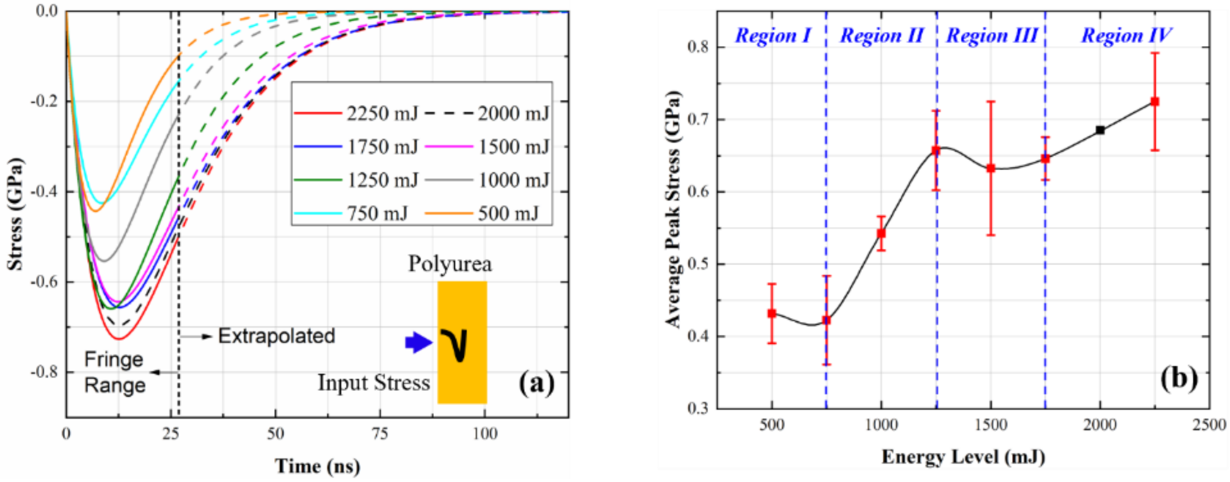

Figure 3.4: (a) The average stress wave profiles transmitted to polyurea for all the energy levels using a glass slide as the main confining layer and waterglass as the secondary confining layer, and (b) the average input peak stress as a function of the laser intensity, delineating four regions based on the interaction of the high energy laser with the energy sacrificial layer.

A byproduct of the modified laser-induced shock wave experimental setup used herein, i.e., the inclusion of the detachable sandwich test structure, is the drastic change in the input stress-time history compared to the conventional setup [19,47]. For example, the duration of the input stress wave in the latter is commonly <100 ns, while the stress profiles reported in Figure 3.5 extend over 175 ns when a 1 mm glass slide is used as a confining layer. Therefore, a tangent experiment was pursued to elucidate the effect of the thickness and the type of the confining layer, compared to the stress-time profile based on the sandwiched test structure shown in Figure 3.4a. In this experiment, an aluminum-coated stainless-steel plate was confined with 100 µm thin layer of waterglass in one test and confined with 1 mm thick glass slide in a different set of measurements. That is, this tangent experiment resorted back to the conventional laser-induced shock wave experiment. Figure 3.5 is a comparison between the stress profile based on the thick glass slide and thin waterglass layer, while all other experimental conditions were kept constant at a laser intensity of 1500 mJ. Regardless of the type of confinement layer, the free surface displacement was measured off the steel plate with a thickness of ~1.2 mm. Figure 3.5 also shows that the confinement using waterglass resulted in lower peak stress (~ 24%) and ~200 ns narrower pulse than that produced when a glass slide was used as a confinement layer. That is to say, the modified laser-induced shock wave technique generated a stronger stress wave profile (i.e., stress wave with higher peak stress), while also broadening the pulse width of the wave profile. The latter affects the experimental strain rate since it is proportional to the slope of the rising peak. The slope of the rising peak for the waterglass and glass slide confining layers are 124 MPa·ns^{-1} and 78 MPa·ns^{-1}, respectively. The confinement layer/strain rate relationship represents a unique opportunity to shape the laser-induced shock wave by adjusting the thickness and material of the confinement layer. This pulse shaper approach is comparable with the methods devised for the split Hopkinson-bar experiment [48]. Notably, Yuan *et al*. reported similar results regarding the thickness of the confining layer [47].

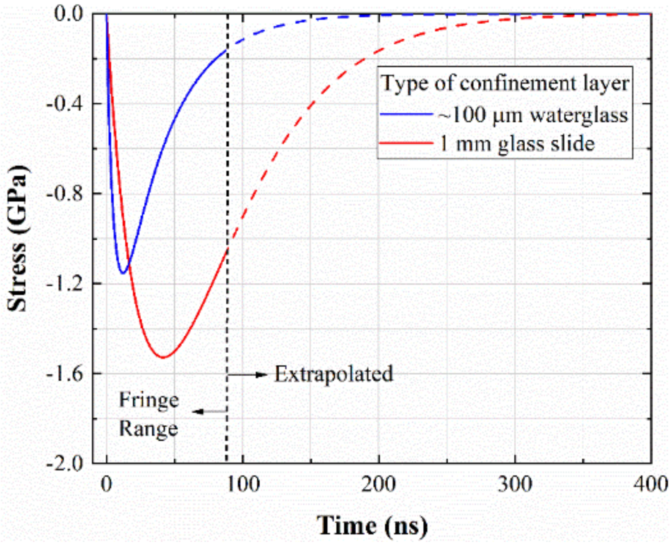

Figure 3.5: Comparison between the characteristics of the stress wave profiles generated under identical conditions, except for the type of confinement layer. Thick glass slide confinement resulted in a stronger but broader shock wave than a waterglass confinement.

3.3.2 Brittle Failure of Shock-loaded Polyurea

The high-peak stresses and high strain rate accompanying laser-induced shock waves result in brittle failure, exemplified in partial or total spallation upon the reflection of the compressive wave from the free surface of the loaded sample. Partial spallation is a byproduct of the interaction of the reflected tensile stress wave with shallow voids or defects, compared to the cohesion strength. Alternatively, total spallation possibly results from through-thickness voids or air bubbles occupying a large region of the sample thickness, motivating a complete removal or tear out of a material plug within the loaded area. In the current work, partial and total spallation failures were observed in several polyurea samples loaded at different laser intensities. In an imperfection-free sample, the stress required to fail a material catastrophically is comparable to the cohesion strength [20]. However, in the presence of defects or voids, the material fails prematurely since the imperfections act as stress risers, locally amplifying the input stress, i.e., failure will occur at lower input stress. Despite the careful attempts to fabricate void-free polyurea, the samples encompassed bubbles with different sizes (some not observed by the naked eye) throughout the thickness. The final location of a bubble is dependent on the ratio between buoyancy and viscosity, indicating the random distribution of a wide range of air bubbles within the loaded areas of the samples.

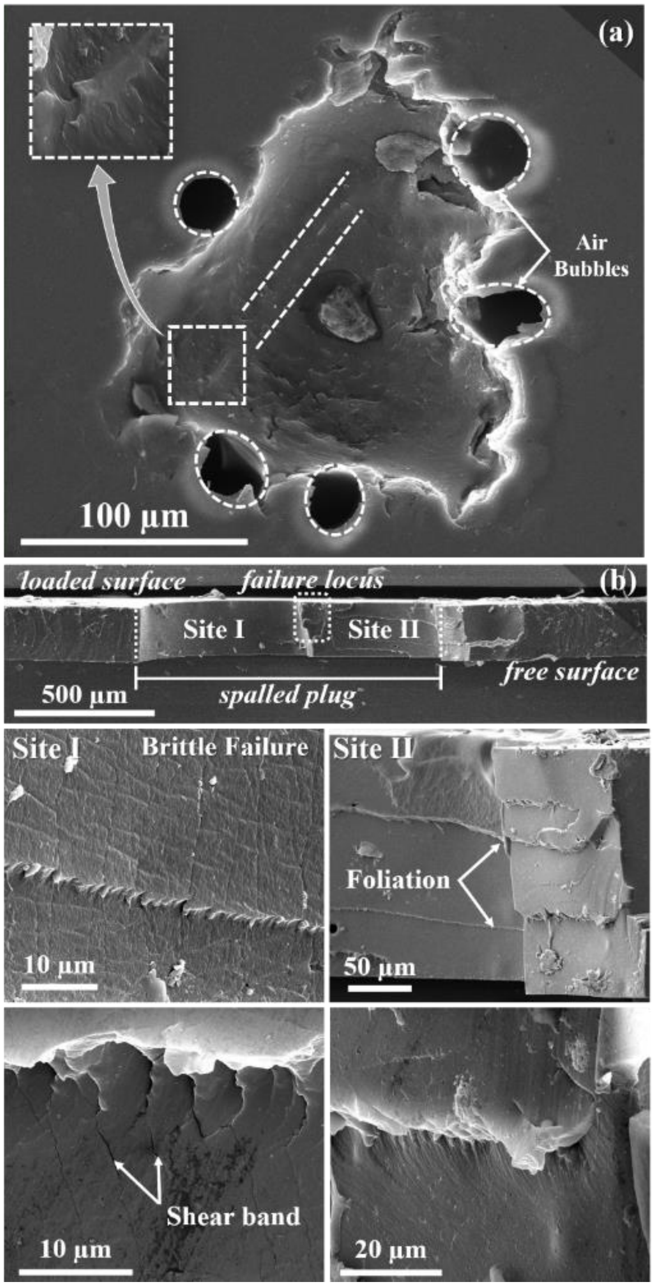

Figure 3.6: (a) SEM micrograph exhibiting the morphology inside a partially spalled area on the free surface. (b) SEM micrographs of the cross section of total spallation with high magnifications on the failed surfaces showing shear bands (middle panel in b) and shear lensing (bottom panel in b).

Figure 3.6a is an example SEM micrograph of partial spallation, where a shallow polyurea fragment spalled at a corresponding energy fluence of ~210 kJ·m^{-2}. Surrounding the partial spallation site is a few entrapped bubbles close to the free surface formed during the fabrication process. These bubbles acted as stress risers, assisting in the cleavage of polyurea by amplifying the stress in the vicinity of the stress riser sites. The morphology of the partial spallation site substantiates the brittle failure supposition, where the material cleaved at a plane deep within the loaded area and bounded by the superficial air bubbles. Moreover, the geometry of the spall site is best described as a conical prism with outwardly slanted sides from the observer's perspective. As the laser-induced shock waves transverse the thickness of the sample, the wavefront broadens while breeding accompanying waves laterally. Our group demonstrated the mode conversion of pressure waves in a recent computational study, generated using laser spallation technique, into a multimode loading, especially close to the free surface [26]. That is to say, the sharp wavefront of the initial pure pressure shock wave becomes wider as it arrives at the surface as multimode loading due to the propagation in a viscoelastic media. Such wave interactions cause the conical geometry at spallation [49]. The inset in Figure 3.6a emphasizes a fault line on the newly exposed fracture surface extending parallel to the edge. The formation of this fault line is attributed to deformation localization during the spallation process, resulting in inelastic deformation as the elastic counterpart gives in to the permanent change. The partial spallation results shown in Figure 6a are in excellent agreement with the previous study reported in [20]. An accompanying finite element simulation based on [26] shows that the strain rate at the wavefront in the vicinity of the free surface is 2.56×10^{6} s^{-1} while is nearly negligible elsewhere.

The harsh mechanical loading conditions associated with laser-induced shock waves may also lead to total spallation, resulting in detachment of a material plug within the laser-illuminated area. Indeed, several polyurea samples studied as part of this research investigation exhibited total spallation. Figure 3.6b is a collage of SEM micrographs, exemplifying total spallation failure (top panel in Figure 3.6b) at an energy level of 2250 mJ. The diameter of the spalled plug was 1.2 mm, or 16% of the loaded area. Other samples also exhibited similar failure characteristics, where the diameter of the spalled plug ranged between 1 mm and 1.5 mm. The difference between the diameter of the laser-illuminated area (i.e., 3 mm) and the diameter of the spalled plug can be explicated in light of the Gaussian profile of the laser pulse, which is demonstrated by the failure locus that corresponded with the central axis of the laser beam. The cross-sectional micrograph in Figure 3.6b of the failure site exemplifies two distinct regions, namely with un-textured (Site I) and textured (Site II) surfaces. The separation between the textured and un-textured region appears to start from the incipient crack on the loaded surface (denoted as the failure locus in Fig. 3.6b) due to the Gaussian profile of the laser beam. To the left of the failure locus, the un-textured region, with an apparent smooth fracture surface, is an additional characteristic of brittle failure expected from loading the material with ultrahigh strain rate shock waves. Remarkably, the textured region also provides evidence of brittle failure. This region is divided into several sub-regions delineated by a lineation or foliation attributed to brittle failure at low strains. The latter is a hallmark characteristic of laser-induced shock waves [6,19]. As the failure progress towards the free surface to catastrophically remove the polyurea plug from the rest of the sample, shear bands start to develop, leading to foliation. The bottom panel in Figure 3.6b is a higher magnification SEM micrograph showing evidence of localized shear lensing, linking foliation, shear bands, and brittle failure. The shear failure characterized by the slightly slanted foliations is indicative of an in-plane shear failure in compression, i.e., occurred during the forward trip of the laser-induced shock wave. A close examination of the thickness of the cross-sectional micrograph in Figure 3.6b indicates that the thickness remained constant at 193.0±1.5 μm when measuring the thickness of the plug in the loaded and unloaded area. The unchanged thickness in the shear zones surrounding the shear bands (foliation) points to simple shear deformation with no evidence of volume change, which is consistent with the findings in previous reports regarding the entire relaxation behavior of polyurea being captured by the shear modulus while the bulk modulus remains elastic [12,50].

The failure modes discussed above potentially give rise to structural changes in the polyurea macromolecule, which can be detected using a bulk spectroscopy technique, e.g., THz-TDS, in the form of spectral changes. The vibrational modes of different bonds within the macromolecule are marked in the THz spectra as peaks, the amplitude and the spread of which exemplify the mechanically induced structural changes. Therefore, the identification of such spectral changes could lead to an interrelationship between spectral alterations and precursor stress. Figure 3.7 is the THz power spectra of polyurea samples exhibiting total spallation failure, demonstrating two noteworthy changes when comparing the spectra of the pre- and post-loaded samples. First, a new spectral peak sprung into existence when focusing on the power spectra around the 1.1 THz region for both samples, which were loaded at different laser intensities. Specifically, the spectral peak at 1.17 THz is only present in the post-loaded frequency response but is completely absent from the spectra of the same sample (and the same location within the sample, as guaranteed by the sample holder design) in the pristine condition. The second spectral change corresponds to a peak at 1.42 THz when the sample was loaded at a laser intensity of 1250 mJ. In this case, the FWHM is 15.2 GHz in the spectrum of the unloaded sample changing to 6.6 GHz in the loaded counterpart. Generally, spectral changes in infrared spectroscopy, new peaks or broadening of existing ones are indicative of intermolecular vibrational modes [51]. For example, Zhao *et al*. observed a spectral peak at 1.47 THz in crystalline urea, which is comparable to the

1.42 THz in the case reported above [52]. This is thought to be associated with torsional motion between the hydrogen bonds linking $O_{13}\cdots H_{43}$—N_{44} and $O_{13}\cdots H_{19}$—N_{20} [52]. The torsional motion may position the connecting hydrogen bond away from the propagation path of the THz wave; hence, it is less apparent in the spectra of the loaded sample and indicating that such rotation is due to the ultrahigh strain rate loading. A final comment is warranted here about the permanent mark the shock wave left on the polyurea structure, which is attributed to the high shear stress state that is initially responsible for the spallation failure mode previously discussed. Future research aim to pinpoint the source of the spectral changes in relation to the ultrahigh strain loading scenario using molecular dynamics, following the recent work of [53].

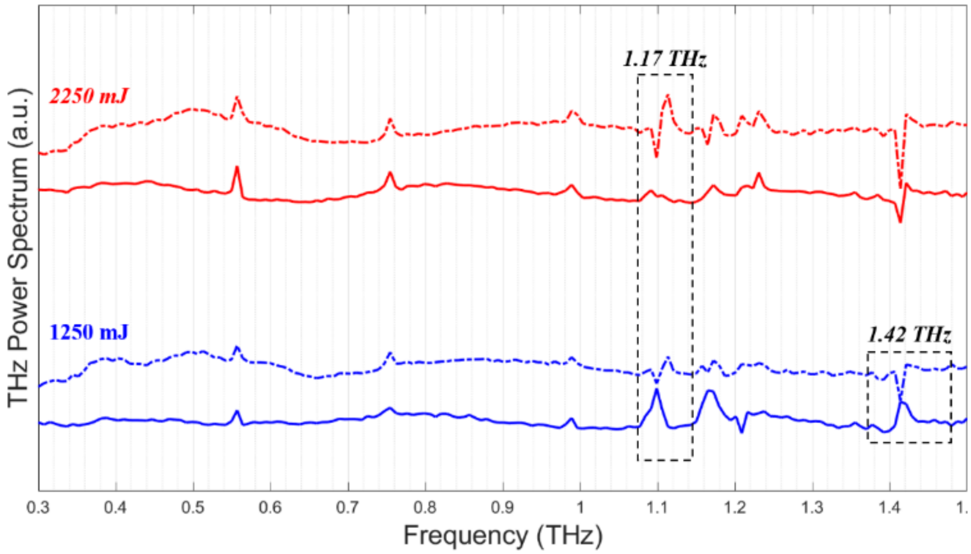

Figure 3.7: Spectral features of THz signal for pre- (solid line) and post-loaded (dashed line) polyurea samples that underwent total spallation.

3.3.3 Ductile Failure of Shock-loaded Polyurea

In addition to the brittle failure discussed in the previous section, signs of permanent plastic deformation associated with ductile failure were also noted in samples that remained intact after shock loading. Such signs of permanent deformation are commonly not observed in ultrahigh strain rate loading scenarios, with low strain levels (in the order of 10^{-2} based on finite element analysis [26]), since the materials undergo ductile to brittle transition, specifically in the case of polymers. The presence of the viscous coupling medium between the sandwich structure and the sample introduced a confined space for the shock wave to build up pressure due to the rapid thermal expansion of the aluminum sacrificial layer (Figure 3.1b). The pressure build-up is then confined on one side by the polyurea sample and the other side by the glass slide. It is worth reiterating that the shock wave was created on the far surface of the confining glass layer (from the laser beam perspective), which then transverse through the waterglass layer towards the sample, passing through the coupling layer. The reflected portion of the shock wave within the viscous medium resulted in a secondary loading condition at a lower strain rate. However, it maintained significant energy, resulting in an additional pressure build-up that plastically deformed the polyurea sample and catastrophically destroyed the glass confining layer. The plastic deformation in polyurea is categorized as plastic bulging and adiabatic shearing.

The pressure build-up between the confining glass layer and the polyurea sample resulted in plastic bulging due to different laser intensities, corresponding to different stress levels, as can be deduced from Figure 3.8. The flow stress of polyurea has been shown to be in the order of 10 MPa when tested at low strain rate conditions, which is expected to increase as the strain rate increases. Wang *et al.* reported the flow stress of polyurea to range between 10 MPa and 43 MPa as the strain rate changes from 10^{-3} to 10^{4} s^{-1}, respectively [54]. The upper bound of the flow stress leads to partial or total spallation without leaving evidence of plastic deformation. In the optical micrographs shown in Figure 3.8 (note that polyurea films were removed from the test structure and were placed on a mounting substrate for optical microscopy), the plastic bulging indicates another mechanism must have been at play given the forecasted pressure build-up due to the generation of the shock wave based on the interaction of the laser illumination and the localized energy sacrificial layer. It appears that the plastic flow compromised the shearing resistance of polyurea, exaggerating the permanent deformation to the levels shown in Figure 3.8. For example, the plastic bulge height was 268.52 μm when polyurea was loaded at 1250 mJ, which has increased to 333.33 μm at a laser intensity of 1500 mJ. Surprisingly, at energy levels above the latter, the bulge height has decreased to levels compared to those reported at lower laser intensities. Such a reversal in the values of the bulge height gives rise to the combined mechanism of plastic flow and lower shearing resistance. It is also related to the failure of the testing sandwich structure (i.e., glass slide) relieving the pressure quicker (discussed next) and limiting the permanent deformation in polyurea. This is further justified since the pressure build-up is expected to be at a lower strain rate than that transmitted towards the polyurea sample and eventually created the partial and total spallation discussed in the previous section. This is significant. In impact mitigation applications, where polyurea is prominent, it is then beneficial to intentionally compromise the bonding interface between the polyurea protective layer and the asset it seeks to protect. Weakening the bonding interface will result in the manifestation of the secondary pressure build-up, resulting in a plastic deformation that dissipates a more significant portion of the incoming impact, evidential from the non-catastrophic plastic deformation of the bulging. Remarkably, Gamez independently showed that constraining polyurea sheets onto a substrate resulted in catastrophic failure, supporting the notion of strategically weakening the bonding interface [55].

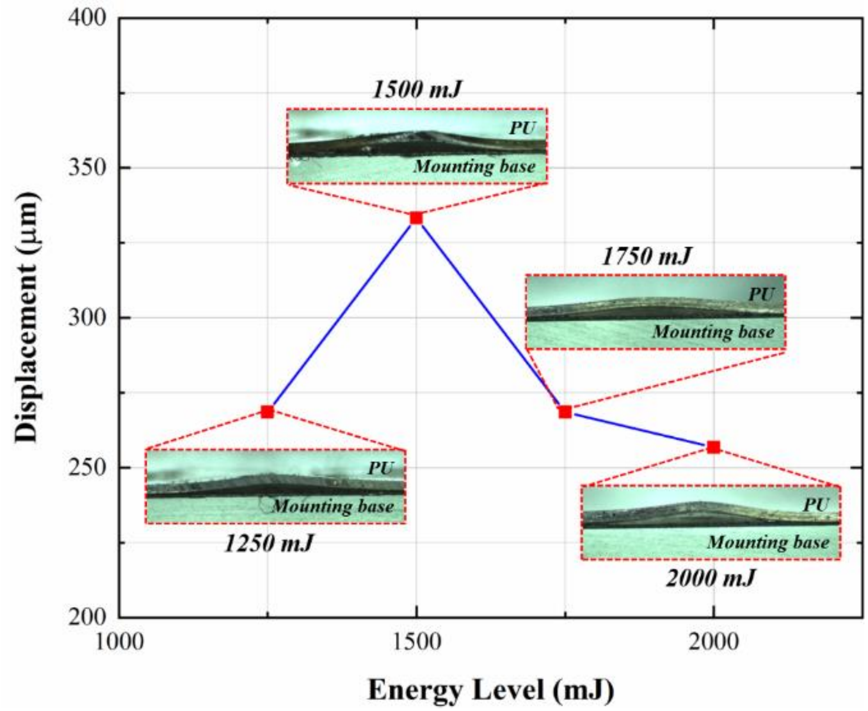

Figure 3.8: Plastic bulge deformation as a function of different energy levels (mounting base was not part of the experiment but was added to facilitate optical microscopy).

To confirm the source of the pressure build-up that led to plastic bulging, the confining glass layer was further examined since it constrained the pressure on one side of the structure. The accumulated pressure acts as an indentation source at energy levels exceeding 750 mJ, leading to the development of a complete Hertzian crack in the 1 mm glass slide. The Hertzian crack resulted in the fracturing of the glass slide due to the release of energy as the edge of the crack reached the free surface, at which point a further increase in the illumination energy translated to negligible effect on the deformation of the tested elastomeric material. The onset of glass fracture can be estimated by using the classical Hertzian model (Eqn. 3.9) as a failure criterion, where the tensile strength (S_{ut}) of soda-lime glass of 41 MPa is compared to load ($\mathcal{P}$) [56].

$$\mathcal{P} = \frac{2\pi r^2 S_{ut}}{(1-2\nu_{gs})} \tag{3.9}$$

Here, ν_{gs} is the Poisson's ratio of the glass slide (taken to be 0.23) [57] and r is the radius of the illuminated area (3 mm), allowing the estimation of the load $\mathcal{P}$. The latter loads the polyurea sample and generates a hoop stress (σ_r) that can be estimated by assuming the pressure cavity between the polyurea sample and the glass substrate is a thin wall spherical pressure vessel (e.g., $\sigma_\theta = \frac{Pr}{2t}$, where, P is the build-up pressure acting on polyurea, r is the radius of curvature of the bulge area (measured optically and taken to be 6.2 mm), and t is the thickness of the polyurea film. The resulting hoop stress developed in the polyurea film is estimated to be 32.80 MPa, pointing to a flow strength of 30 MPa at strain rate of 10^3 s^{-1} based on the work of Wang *et al.* [54].

The excessive plastic bulging deformation discussed above was associated with high mechanical work done on the material, resulting in a localized shear deformation due to the conversion of the mechanical work to heat [58,59]. The localized shear deformation is associated with the high compressive stress wave due to shock loading. In other words, a material instability arises due to thermal softening that overpower the effect of strain hardening [58,59]. However, the heat stayed local to the loading site at the location of maximum deformation (high plastic work) due to the poor thermal conductivity of elastomeric polymers such as polyurea. The exchange of plastic mechanical work to localized heat has been associated with adiabatic shearing exemplified as microcracks on the surface. That is, the generated heat caused localized softening of the material, thus, leading to localized shearing. It is important to separate between the heat generated from the impingement of the aluminum sacrificial layer with the high energy laser from the localized heating due to the work done. The former happens at a much large time scale than the shock event, since it is attributed to the heat transfer process, where the effect remains localized and far from the polyurea sample (separated by the aqueous coupling and the secondary confinement layers). Therefore, the dynamic deformation of polyurea due to the localized adiabatic heating can be described by a balance between the mechanical stress and the heat transfer due to the heat capacity of the material within the plastic deformation (ε_p) regime while suppressing the thermoelastic effect [58,60]

$$\rho_p c_p \Delta T = \int \sigma d\varepsilon_p \qquad (3.10)$$

where, ρ_p is the density of polyurea (1071 kg·m^{-3}), c is the specific heat capacity (1150-1400 J·kg^{-1}·K^{-1} for temperatures ranging from -40 °C to 40 °C [61]), and ΔT is the adiabatic temperature rise. The latter was estimated based on the plastic strain deduced from the bulging height shown in Figure 8 ($\varepsilon_p \approx 0.9$, translating to ~20 K change). The rise in temperature due to adiabatic shearing was then used to model the constitutive response of polyurea through thermal softening (due to work done) and strain hardening equation, Cowper-Symonds rate dependent function [62], such that

$$\sigma = A\left(1 - B\varepsilon_p^l + C\varepsilon_p\right)\left[1 + \left(\frac{\dot{\varepsilon}}{D}\right)^{1/w}\right]\left[1 - q(\Delta T)\right] \qquad (3.11)$$

where, A, B, C, and D are model fitting parameters, l is the strain hardening parameter, q is a thermal softening parameter, w is the strain rate parameter, and ΔT is the difference between the current temperature and reference temperature. This thermal viscoelastic model exemplifies that the temperature due to adiabatic shearing results in reduction of the strain rate due to thermal softening.

The thermal softening leading to adiabatic shearing can also be detected as changes in the local material properties, embodied as changes in the microscale local modulus in the samples interrogated with the laser-induced shock wave. Figure 3.9 is a collection of optical and AFM micrographs of the post-loaded samples, showing the microcracks and shear bands (since it lack the periodicity, pre-stretching, and energy required for wrinkling [63]) at the loaded surface of the polyurea samples as a function of laser intensity. The localized heat due to the plastic deformation resulted in embrittlement of the surface layer, given the thermoset nature of polyurea, due to the spontaneous increase in temperature. The surface embrittlement translated into an increase in the local elastic modulus, as demonstrated by the force-displacement results from the AFM nanoindentation measurements. The local modulus increased from 297±4 MPa to 333±2 MPa when the laser intensity increased from 1250 mJ to 1750 mJ. However, at energy levels greater than 1750 mJ, the average modulus no longer increases, which is similar to the pattern seen in the laser-energy and stress relationship plotted in Figure 3.4.

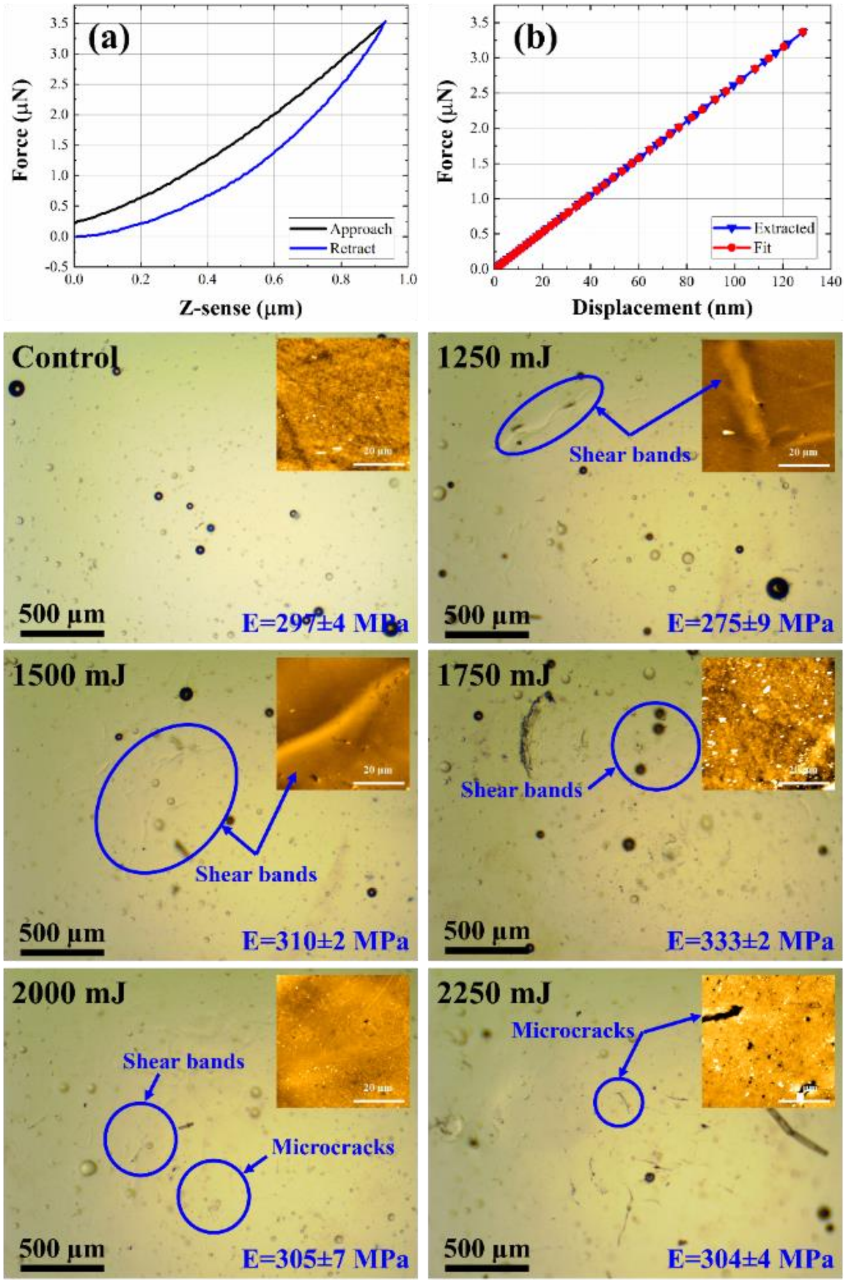

Figure 3.9: Optical and AFM topographical micrographs of polyurea after loading at different energy level using LSW and the corresponding average local modulus, which were calculated from (a) the force-displacement curves collected using nanoindentation and (b) fitted to the Oliver and Pharr model.

The permanent plastic deformation after shock loading due to the pressure build-up exaggerated the spectral changes discussed in the previous section, where a spectral evolution was detected at 1.17 THz. Figure 3.10 culminates the terahertz spectra corresponding to samples with plastic deformation but remained spall-free. The 1.17 THz peak started to appear in the spectra upon shock loading at higher intensities exceeding 1750 mJ, which is in good agreement with the results discussed previously. This possibly points to the same source of energy (i.e., mechanical to chemical energy conversion) based on the torsional motion of the hydrogen bonds between urea linkages. The total spallation failure corresponds to jettisoning the chains, whereas plastic deformation corresponds to sliding and rotation while the chains are still intact. Remarkably, a peak at the 1.1 THz region disappeared from the spectra associated with loading at a laser intensity of 2250 mJ. This peak observed in the polyurea spectra is in reasonable agreement with the 1.08 THz peak found in crystalline urea, as reported by Zhao *et al*. [52]. Thus, the spectral change at 1.1 THz indicates the extinction or restriction of the torsional motion of hydrogen bonds between the urea molecules, resembling the torsional motion of the bonds found at the 1.08 THz peak of crystalline urea. Therefore, the results of the THz measurements ascertain that plastic bulging and adiabatic shearing (observed in the AFM micrographs) dampens or eliminates the torsional motion of the hydrogen bonds corresponding to 1.1 THz, while also activating or exciting intermolecular motion of a bond requiring 4.8 meV found in aromatic amorphous polyurea. In all, the terahertz analysis is suitable for nondestructively revealing failure in elastomeric polymer. Future research aims to provide further evidence for the utility of THz-TDS in experimental solid mechanics.

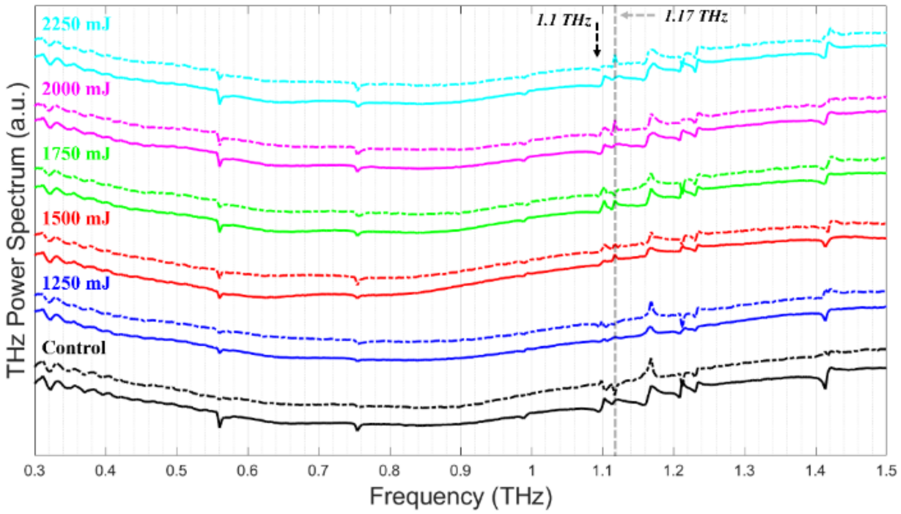

Figure 3.10: THz transfer function of the pre- (solid) and post-loaded (dashed) polyurea samples exhibiting crazing or adiabatic shear bands.

3.4 Conclusion

In closing, laser-induced shock wave experimental technique was coupled with spectroscopy and microscopy to elucidate the mechanical and structural response of polyurea, a thermoset elastomer, used in impact mitigation applications. The LSW setup loaded the material under ultrahigh strain rate conditions but with limited deformation, leading to explicating the intrinsic behavior of the material. Bulk terahertz time-domain spectroscopy nondestructively interrogated the material, detecting structural changes in the macromolecule induced by the ultrahigh rate mechanical loading. Brittle and ductile failures were reported in the response of polyurea due to shock loading. The former encompassed partial and total spallation, where a portion or a plug of the sample was removed. The latter included plastic deformation (in the form of plastic bulging) and adiabatic shearing. While not expected in this loading regime, the ductile failure exemplifies a unique opportunity to study ductile failure at low strains and high strain rates to explicate the fundamental attenuation mechanisms. Remarkably, terahertz-based spectroscopy detected and reported structural changes in the polyurea macromolecule. These spectral features in the resulting terahertz measurements after shock loading demonstrated the validity of terahertz spectroscopy in noninvasively detecting the underpinning failure mechanisms of polyurea undergoing dynamic loading. The armor-development community can benefit from the results by strategically tuning the interface between the armor plate and the protective coating to achieve excessive plastic deformation, hence, enhanced impact mitigation. Finally, the results and experimental framework will guide future work towards:

1- Seeking further investigations into the spectroscopic and mechanical performances of polymeric materials using hybrid, multiscale experimental and computational approaches;
2- Amending existing polymer viscoplasticity and damage models to account for the results reported above; and
3- Developing an experimental setup and procedure for material characterization in-situ ultrahigh strain rate loading.

Acknowledgement

Chapter 3, in part, is a reprint of the material as it appears in Macromolecular Materials and Engineering 2021. Huynh, Nha Uyen; Gamez, Carlos; Youssef, George, Wiley, 2021. The dissertation author was the primary investigator and author of this paper.

References

1. Youssef, G. & Whitten, I. Dynamic properties of ultraviolet-exposed polyurea. *Mech. Time-Dependent Mater.* **21**, 351–363 (2017).

2. Bahei-El-Din, Y. a., Dvorak, G. J. & Fredricksen, O. J. A blast-tolerant sandwich plate design with a polyurea interlayer. *Int. J. Solids Struct.* **43**, 7644–7658 (2006).

3. Grujicic, M. *et al.* Computational investigation of impact energy absorption capability of polyurea coatings via deformation-induced glass transition. *Mater. Sci. Eng. A* **527**, 7741–7751 (2010).

4. Barsoum, R. G. S. & Dudt, P. J. The fascinating behaviors of ordinary materials under dynamic conditions. *Ammtiac Q* **4**, 11–14 (2010).

5. Jain, A. Strength/moisture relationship for interfaces and joints for robust prediction of reliability. (University of California, Los Angeles, 2007).

6. Youssef, G. H. Dynamic Properties of Polyurea. (University of California, Los Angeles, 2010).

7. Walsh, S. M., Scott, B. R. & Spagnuolo, D. M. The Development of a Hybrid Thermoplastic Ballistic Material With Application to Helmets. *Int'l Ballist. Symp.* 37 (2005).

8. Tekalur, S. A., Shukla, A. & Shivakumar, K. Blast resistance of polyurea based layered composite materials. *Compos. Struct.* **84**, 271–281 (2008).

9. Yi, J., Boyce, M. C., Lee, G. F. & Balizer, E. Large deformation rate-dependent stress-strain behavior of polyurea and polyurethanes. *Polymer (Guildf).* **47**, 319–329 (2006).

10. Cho, H. & Boyce, M. C. *Constitutive Modeling of High Strain-Rate Elastomeric Polymers: Mechanics of Large Deformation Behavior of Elastomeric Copolymers: Resilience, Dissipation, and Constitutive Modeling*. *Elastomeric Polymers with High Rate Sensitivity: Applications in Blast, Shockwave, and Penetration Mechanics* vol. 9 (2015).

11. Rinaldi, R. G., Boyce, M. C., Weigand, S. J., Londono, D. J. & Guise, M. W. Microstructure evolution during tensile loading histories of a polyurea. *J. Polym. Sci. Part B Polym. Phys.* **49**, 1660–1671 (2011).

12. Youssef, G. & Gupta, V. Dynamic response of polyurea subjected to nanosecond rise-time stress waves. 317–328 (2012) doi:10.1007/s11043-011-9164-7.

13. Rice, M. C., Arruda, E. M. & Thouless, M. D. The use of visco-elastic materials for the design of helmets and packaging. *J. Mech. Phys. Solids* **141**, 103966 (2020).

14. Liao, Y. *et al.* Shock wave impact on the viability of MDA-MB-231 cells. *PLoS One* **15**, 1–18 (2020).

15. Breedlove, K. M., Breedlove, E. L., Bowman, T. G., Arruda, E. M. & Nauman, E. A. The effect of football helmet facemasks on impact behavior during linear drop tests. *J. Biomech.* **79**, 227–231 (2018).

16. Sarva, S. S., Deschanel, S., Boyce, M. C. & Chen, W. Stress-strain behavior of a polyurea and a polyurethane from low to high strain rates. *Polymer (Guildf).* **48**, 2208–2213 (2007).

17. Jiao, T., Clifton, R. J. & Grunschel, S. E. Pressure-sensitivity and constitutive modeling of an elastomer at high strain rates. *AIP Conf. Proc.* **1195**, 1229–1232 (2009).

18. Gupta, V., Argon, A., Cornie, J. & Parks, D. Measurement of interface strength by laser-pulse-induced spallation. *Mater. Sci.* (1990).

19. Wang, J., Weaver, R. L. & Sottos, N. R. A parametric study of laser induced thin film spallation. *Exp. Mech.* **42**, 74–83 (2002).

20. Youssef, G. & Gupta, V. Dynamic tensile strength of polyurea. *J. Mater. Res.* **27**, 494–499 (2011).

21. Jain, A., Youssef, G. & Gupta, V. Dynamic tensile strength of polyurea-bonded steel/E-glass composite joints. *J. Adhes. Sci. Technol.* **27**, 403–412 (2013).

22. Grujicic, M., He, T. & Pandurangan, B. Development and parameterization of an equilibrium material model for segmented polyurea. *Multidiscip. Model. Mater. Struct.* **7**, 96–114 (2011).

23. Bogoslovov, R. B., Roland, C. M. & Gamache, R. M. Impact-induced glass transition in elastomeric coatings. *Appl. Phys. Lett.* **90**, (2007).

24. Grujicic, M. *et al.* Concept-level analysis and design of polyurea for enhanced blast-mitigation performance. *J. Mater. Eng. Perform.* **21**, 2024–2037 (2012).

25. Amini, M. R., Isaacs, J. B. & Nemat-Nasser, S. Experimental investigation of response of monolithic and bilayer plates to impulsive loads. *Int. J. Impact Eng.* **37**, 82–89 (2010).

26. Gamez, C., Huynh, N. U. & Youssef, G. In-silico experimentations of multimode shock response of polyurea. *Int. J. Mech. Sci.* **204**, 106542 (2021).

27. Sun, Y., Kooi, S. E., Nelson, K. A., Hsieh, A. J. & Veysset, D. Impact-induced glass-to-rubber transition of polyurea under high-velocity temperature-controlled microparticle impact. *Appl. Phys. Lett.* **117**, (2020).

28. Shaik, A. M., Huynh, N. U. & Youssef, G. Micromechanical behavior of ultraviolet-exposed polyurea. *Mech. Mater.* **140**, 103244 (2020).

29. Sun, Q. *et al.* Recent advances in terahertz technology for biomedical applications. *Quant. Imaging Med. Surg.* **7**, 345–355 (2017).

30. Zhong, S. Progress in terahertz nondestructive testing: A review. *Front. Mech. Eng.* **14**, 273–281 (2019).

31. Yang, R. *Analytical Methods for Polymer Characterization*. *Analytical Methods for Polymer Characterization* (2018). doi:10.1201/9781351213158.

32. Mirabella, F. M. *Internal Reflection Spectroscopy. Theory and applications*. *Analytica Chimica Acta* vol. 276 (1993).

33. Huynh, N. & Youssef, G. Physical Evidence of Stress-Induced Conformational Changes in Polymers. *Exp. Mech.* **61**, 469–481 (2021).

34. Duvillaret, L., Garet, F. & Coutaz, J. L. A reliable method for extraction of material parameters in terahertz time-domain spectroscopy. *IEEE J. Sel. Top. Quantum Electron.* **2**, 739–745 (1996).

35. Barker, L. M. Laser interferometry in shock-wave research. *Exp. Mech.* **12**, 209–215 (1972).

36. Youssef, G. *et al.* Inter-wafer bonding strength characterization by laser-induced shock

waves. **094902**, 1–5 (2012).

37. Shim, J. & Mohr, D. Using split Hopkinson pressure bars to perform large strain compression tests on polyurea at low, intermediate and high strain rates. *Int. J. Impact Eng.* **36**, 1116–1127 (2009).

38. Ehsani, H., Boyd, J., Wang, J. & Grady, M. Evolution of the Laser-Induced Spallation Technique in Film Adhesion Measurement. *Appl. Mech. Rev.* **73**, (2021).

39. Kandula, S. S. V., Hartfield, C. D., Geubelle, P. H. & Sottos, N. R. Adhesion strength measurement of polymer dielectric interfaces using laser spallation technique. *Thin Solid Films* **516**, 7627–7635 (2008).

40. Ginzel, E. & Turnbull, B. Determining approximate acoustic properties of materials. *NDT.net* 1–10 (2016).

41. Achenbach, J. D. Wave Propagation in Elastic Solids. *Wave Propag. Elastic Solids* (1975) doi:10.1016/c2009-0-08707-8.

42. Qiao, J., Amirkhizi, A. V., Schaaf, K., Nemat-Nasser, S. & Wu, G. Dynamic mechanical and ultrasonic properties of polyurea. *Mech. Mater.* **43**, 598–607 (2011).

43. Pryor, A. W. & Roscoe, R. The velocity and absorption of sound in aqueous sugar solutions. *Proc. Phys. Soc. Sect. B* **67**, 70–81 (1954).

44. Kryjevskaia, M., Stetzer, M. R. & Heron, P. R. L. Student understanding of wave behavior at a boundary: The relationships among wavelength, propagation speed, and frequency. *Am. J. Phys.* **80**, 339–347 (2012).

45. Oliver, W. & Pharr, G. An improved technique for determining hardness and elastic modulus using load and displacement sensing indentation experiments. *J. Mater. Res.* **7**, 1564–1583 (1992).

46. Amirkhizi, A. V., Isaacs, J., McGee, J. & Nemat-Nasser, S. An experimentally-based viscoelastic constitutive model for polyurea, including pressure and temperature effects. *Philos. Mag.* **86**, 5847–5866 (2006).

47. Yuan, J., Gupta, V. & Pronin, A. Measurement of interface strength by the modified laser

spallation technique. III. Experimental optimization of the stress pulse. *J. Appl. Phys.* **74**, 2405–2410 (1993).

48. Zou, G. P., Shen, X. H., Chang, Z. L., Wang, Y. W. & Wang, P. A Method of Restraining the Geometric Dispersion Effect on Split-Hopkinson Pressure Bar by the Modified Striker Bar. *Exp. Tech.* **40**, 1249–1261 (2016).

49. Meyers, M. A. *Dynamic Behavior of Materials*. (John Wiley and Sons, 1994).

50. Knauss, W. G. & Zhao, J. Improved relaxation time coverage in ramp-strain histories. *Mech. Time-Dependent Mater.* **11**, 199–216 (2007).

51. Hamilton, L. F. & Simpson, S. G. *Quantitative Chemical Analysis*. (Macmillan, 1952).

52. Zhao, Y. *et al.* Intermolecular vibrational modes and H-bond interactions in crystalline urea investigated by terahertz spectroscopy and theoretical calculation. *Spectrochim. Acta - Part A Mol. Biomol. Spectrosc.* **189**, 528–534 (2018).

53. Heyden, S., Ortiz, M. & Fortunelli, A. All-atom molecular dynamics simulations of multiphase segregated polyurea under quasistatic, adiabatic, uniaxial compression. *Polymer (Guildf).* **106**, 100–108 (2016).

54. Wang, H. *et al.* Investigating the dynamic mechanical behaviors of polyurea through experimentation and modeling. *Def. Technol.* **15**, 875–884 (2019).

55. Gamez, C. Failure mechanisms of polyurea under high strain-rate. vol. 1 (University of California Los Angeles, 2017).

56. Fischer-Cripps, A. C. The Hertzian contact surface. *J. Mater. Sci.* **34**, 129–137 (1999).

57. Soda-Lime Glass. *MakeItFrom* (2020).

58. Fleck, N. A. Adiabatic Shear Instability: Theory. in *Mechanical Properties and Testing of Polymers* 15–19 (Springer, Dordrecht, 1999). doi:10.1007/978-94-015-9231-4_4.

59. Dodd, B. & Bai, Y. *Adiabatic Shear Localization*. *Adiabatic Shear Localization* (2012). doi:10.1016/C2011-0-06979-X.

60. Zhang, L., Pellegrino, A., Townsend, D. & Petrinic, N. Temperature Dependent Dynamic Strain Localization and Failure of Ductile Polymeric Rods under Large Deformation. *Int. J. Mech. Sci.* 106563 (2021) doi:10.1016/j.ijmecsci.2021.106563.

61. Shahi, V., Alizadeh, V. & Amirkhizi, A. V. Thermo-mechanical characterization of polyurea variants. *Mech. Time-Dependent Mater.* **24**, 1–25 (2020).

62. Cowper, G. & Symonds, P. *Strain hardening and strain-rate effects in the impact loading of cantilever beam*. *Brown University Division of Applied Mathematics* (Brown University Division of Applied Mathematics, 1957).

63. Jin, L., Takei, A. & Hutchinson, J. W. Mechanics of wrinkle/ridge transitions in thin film/substrate systems. *J. Mech. Phys. Solids* **81**, 22–40 (2015).

CHAPTER 4

In-silico experimentations of multimode shock response of polyurea

Carlos Gamez, Nha Uyen Huynh, and George Youssef*

Experimental Mechanics Laboratory, Mechanical Engineering Department, San Diego State University, 5500 Campanile Drive, San Diego, Ca 92182-1323

Abstract

Computational studies can supplement existing ultrahigh strain rate experimental techniques in the absence of invasive full-field measurement and visualization. In this study, a computational model is employed to elucidate various phenomena accompanying the generation, propagation, and interaction of multimode shock waves in viscoelastic material. Specifically, a 4 mm diameter polyurea plug with a thickness of 0.5 mm was modeled as a linear viscoelastic solid, where the relaxation behavior of the shear modulus was described using a Prony series while the Bulk modulus was assumed to be linear elastic based on the Poisson's ratio of polyurea. The results are presented in three case studies, where a different type of shock wave was emphasized in each case while focusing on the regions at the leading and trailing edges of the shock wavefront. Generally, the wavefront interacted with the accompanying and reflected waves, resulting in compromising the purity of the sought-after loading condition, especially during the return trip of the wave upon approaching the free surface. In Case Study I, the propagation of laser-induced pressure wave remained pure during the forward trip towards the free surface but was compromised by the accompanying shear wave and side spherical patterned pressure waves. Case Study II simulated the generation of surface waves by incorporating a ring-shaped loading site, where the release of a surface displacement was found to be focused and amplified at the central point. In the final case study, Case Study III, the applied shear wave at ultrahigh strain rate generated secondary pressure and horizontal shear waves at the edges of the loading site, which complicated the loading scenario but provided new insight into the interaction of laser-generated shock waves with the solid. The results can be used to improve the analysis of experimental data to quantify the accompanying deformation and failure mechanisms of polymers subjected to hypervelocity impacts.

Keywords: Polyurea, multimode shock waves, in-silico, ultra-high strain rate.

***Corresponding author:** gyoussef@sdsu.edu

4.1 Introduction

The continuous emergence of shock-tolerant and shock-resistant structures and materials requires rigorous methods to evaluate its structural and mechanical integrity in response to shock loading from hypervelocity projectiles. Several experimental methods have been used for decades to advance the state of knowledge but have some debilitating limitations, such as not reporting the full-field stress and strain states as a function of relatively short loading times. Recent experimental research pursued high-speed digital image correlation methods, with some reported and foreseen roadblocks in terms of the available frame grabbing capabilities related to the loading rate. Most shock loading material testing mechanisms are suitable for a single shock event, following an elaborate and expensive experimental setup preparation. After the single shock event, a prolonged downtime is needed to extract the tested structure and reload a new virgin sample for subsequent testing. In addition to these experimental methods, computational analyses have been either an integral or supplementary part of the shock testing methods. For example, in laser-induced shock waves, discussed in detail later, a two-dimensional finite element solution is sought in tandem with the experiment to explicate the stress at the corresponding depth of spallation. In some instances, e.g., purely elastic response of time-independent materials, the finite element simulation can be replaced by one-dimensional elastodynamic solutions, similar to what has been reported in [1–3]. This current study aims to accelerate the study of shock loading material by providing insight into the mechanical response at the leading and trailing edges of the shock wavefront using an in-silico approach. The shock event emphasized in this study replicates multimode stress waves based on laser-induced shock wave testing apparatus.

In-silico methods have significantly impacted several disciplines, including materials science and engineering and mechanical sciences [4]. Computer-based models can simulate how a material mechanically responds under different geometrical configurations and external stimuli over a broad range of temporal and spatial scales. However, only a representative finite element model that accurately captures the details of the problem at hand can reduce the amount of experimentation by simulating mechanical responses. In the past, computer-based models have been used to simulate nanosecond shock wave-induced surface acoustic waves [5], attenuation of shock waves in geometrically complicated metal plates [6], and propagation of seismic waves from earthquakes [7]. Zhang *et al.* experimentally and numerically studied the propagation of spherical laser-induced shock waves, leading to confirmation of the stress state corresponding to fracture failure [5]. They investigated a relatively low range of stress amplitudes (up to ~10 MPa) and rates (impulse pressure within the microsecond rise time range). Zhang *et al.* found that the direction of the principal stress in a circular pattern coincided with the trajectory of crack initiation, hypothesizing the utility of their finding in the generation of high loading rate applications, e.g., reducing the likelihood of a concussion [5]. Furthermore, they ascertained the utility of finite element simulations for identifying and visualizing the propagated shock waves at the boundary between the two adjacent media used in the study. Kumar *et al.* leveraged computational analysis to investigate the effectiveness of perforation and porosity in armor plates on mitigating the bluntness of shock events [6]. They simulated a shock tube condition up to 1.3 MPa at a Mach number ranging from 1.2 to 1.6. Kumar *et al.* concluded that the shock waves lose its momentum as well as the peak pressure as it passes through these attenuated, perforated plates, based on the results of the computational analysis, [6]. Moreover, computational analyses are effective in studying large-scale problems, including the propagation of seismic waves surrounding vital infrastructures such as dams and bridges, which are otherwise prohibitively expensive to study [7].

A vital aspect of computational analyses is a well-defined constitutive behavior model of the material and representative boundary conditions congruent to those present during experimentation or field deployment. Materials behave differently depending on the strain rate, i.e., rate of deformation. When the strain rate is above 10^2 s^{-1}, it is considered a high strain rate, and the load is classified as dynamic. Generally, the strain rate regimes are $10^2 < \dot{\varepsilon} < 10^4$ s^{-1} for high strain rate, $10^4 < \dot{\varepsilon} < 10^6$ s^{-1} for very high strain rate, and $\dot{\varepsilon} > 10^6$ s^{-1} for ultrahigh strain rate [8,9]. The latter is used to investigate fundamental material attributes such as flow stress, wave propagation, and failure processes. Different experimental techniques are used to accomplish a specific strain rate regime. Plate impact [10], laser-induced particle impact test (LIPIT) [11], and laser-induced stress wave [12–16] techniques can load materials at ultrahigh strain rate, i.e., $\dot{\varepsilon} > 10^6$ s^{-1}. The laser-induced shock waves (LSW) rely on focusing a high-energy pulsed laser on an energy absorbent sacrificial layer. This layer absorbs the energy and undergoes rapid thermal expansion that launches a high amplitude shock wave into the test structure. The compressive stress wave travels through the sample and reflects due to an acoustic impedance mismatch at the interface between different materials or at the free surface. When the amplitude of the reflected tensile wave exceeds the tensile strength of the sample, debonding of adjacent layers or spalling occurs, respectively. By changing the planar substrate into a triangular prism and allowing the originally generated longitudinal wave to mode-convert into a shear wave, Wang *et al.* successfully extended laser spallation to mixed-mode and pure-shear loading [15]. The application of the LSW technique has been extended from the adhesion of blanket thin films [15–17] to patterned thin films [18,19] and adhesion between biological cells and inorganic substrates [20,21] as well as the interfacial strength of directly bonded wafers. Recently, laser-induced shock waves have been used in microstructural material characterization to study nucleation, propagation, coalescence, dislocation mobility, and annihilation [22,23]. Overall, the laser-induced shock wave technique is unique since the time for creep or post-loading annealing is negligible based on the ultrahigh strain loading and is limited to the elastic strain regime.

A prominent example of shock-tolerant and shock-resistant material is elastomeric polyurea, which has been afforded a great deal of research in the past two decades, leading to a culmination of significant advancements by Barsoum [24]. Polyurea is a thermoset elastomer synthesized by an amine and an isocyanate polymerization, resulting in a domain-segregated microstructure consisting of hard and soft segments [25]. The segregated microstructure has been credited for its superior properties, including moisture-, chemical-, and abrasion-resistant, large extensibility before tearing, and hyperelastic attributes [26]. Additionally, polyurea has been investigated under a wide range of temperatures, environmental conditions, and strain rates [27], prompting its integration as a protective coating in civilian and military applications [28]. Plate impact experiments have been performed to evaluate the dynamic properties by Mock *et al.* [29]. Roland *et al.* used a drop weight test to investigate the uniaxial tensile response of polyurea at intermediate strain rates (0.06–573 s^{-1}) [30]. Sarva *et al.* [31], Shim and Mohr [32] conducted uniaxial quasi-static and split-Hopkinson-pressure-bar (SHPB) compression studies on polyurea over a range of strain rates (10^{-3}–10^{4} s^{-1}). Youssef *et al.* have studied the polymer at ultrahigh strain rate (10^{6} s^{-1}) using laser-generated pressure stress waves, reporting the overall mechanical response and the dynamic mechanical strength of 93.1±5 MPa [3,33–36]. The latter was found to be in excellent agreement with the results of the plate impact experiment performed by Jiao *et al.* [26]. Subsequently, Gamez *et al.* investigated the shear response of polyurea also using laser-induced shock waves [37]. The overarching outcome of these experimental studies substantiates the technical importance of polyurea and exposes a gap in understanding the interaction between single or multimode shock loadings and the bulk material.

This research study aims to establish a computational analysis framework to elucidate the interaction of multimode laser-induced shock waves while emphasizing the regions at the leading and trailing edges of the shock front. This aim motivated the pursuit to answer some fundamental questions, including:

1) What is the evolution of the wavefront (temporally and spatially) as a function of propagation direction while accounting for the viscoelastic response of the material?
2) What are the byproduct waves birthing from the initial stress wave, and how do they affect the purity of the initial wave?

The present study includes the time-dependence response of polyurea using linear viscoelasticity in response to pressure, shear, and surface waves at ultrahigh strain rates (with nanoscale rise time). The outcomes can be used to enhance the future analysis of experimental data and motivate new in-situ or in-operando characterization techniques to quantify the accompanying deformation and failure mechanisms.

4.2 Computational Model

Several researchers have previously documented the elastodynamic solution; however, there are two overarching shortcomings of the current state-of-the-art [1–3]. First, the integration of time-dependent and nonlinear material behaviors increases the computational expense of the solutions since they require coupled temporal and spatial discretization. Second, the results are usually visualized in a minimalist approach, leaving crucial details about the interaction of the propagating stress wave with the solid at the wavefront obscured. The latter has created a gap in the fundamental understanding of the evolution in stress as the wave advances through the solid. To remedy these shortcomings, a computational model based on the finite element method was established in COMSOL Multiphysics (version 5.4) as part of this research study, enabling concurrent temporal and spatial discretization, thus, resulting in ease of visualization of the propagating stress wave in time and space. The time-dependent analysis solves the equation of motion

$$\rho \frac{\partial \boldsymbol{u}}{\partial t^2} = \nabla \cdot S + \boldsymbol{F}_v \tag{4.1}$$

where ρ is the density, $\boldsymbol{u}$ is the displacement field, S is the second Piola-Kirchhoff stress tensor, and $\boldsymbol{F}_v$ is the volume force [38]. The model also uses the following constitutive relations

$$S = S_0 + S_{ext} + S_q + C : \epsilon_{el} \tag{4.2}$$

$$S_q = \sum_i 2G_i(\tau_i \dot{\epsilon}_i) \tag{4.3}$$

$$\tau_i \rightarrow a_T \tau_i \tag{4.4}$$

where S_0, S_{ext}, and $S_q$are the initial, external, and viscoelastic second Piola-Kirchhoff stress tensor, respectively, C is the elasticity tensor, ϵ_{el} is the elastic strain, G_i is the shear modulus, τ_i is the relaxation time, and a_T is the shift function [38]. The variables G_i, τ_i, and a_T are discussed later.

The spatial dimensionality of the computational model was adjusted depending on the waveforms, e.g., pressure vs. shear waves. The reduced models are discussed in the corresponding case studies. In what follows, the common aspects of the computational model are delineated, including the material model, discretization schema, and the mathematical representation of the input waveforms.

As discussed in the introduction, polyurea is an elastomeric thermoset with time-dependent properties and a nonlinear response. However, laser-induced shock waves load the samples at small strains under ultrahigh strain rate conditions, suppressing the inelastic deformation mechanisms, e.g., creep and plasticity, where the failure is commonly reported in the elastic region since the material has insufficient time to fail otherwise. Such a loading scenario has a twofold implication. First, the strain is limited to small deformation in the linear region of the stress-strain regime. Second, the time-dependent response plays a crucial role in the behavior. In short, the response of polyurea (or polymeric materials in general) to laser-induced shock waves can be sufficiently described by linear viscoelasticity, as shown in the recent literature [19,34–36]. Moreover, it was confirmed that the Time-Temperature Superposition Principle is valid for polyurea even at the high strain rates congruent with those used in the present virtual experiments (>10^5 s^{-1}) [36], extending the thesis first advanced by Zhao *et al.* [39]. We adopt the same approach here, which is succinctly summarized next.

Polyurea was modeled as a linear viscoelastic solid with a density of 1071 $kg{\cdot}m^{-3}$, pressure wave speed of 1750 $m{\cdot}s^{-1}$, and shear wave speed of 415 $m{\cdot}s^{-1}$ [40]. The Poisson's ratio was taken to be 0.486 [3,34,36,39,41], marking polyurea as a nearly incompressible material. The latter implies that the entire relaxation behavior of polyurea can be captured by the shear modulus, while the volumetric deformation can be represented with linear elasticity, i.e., volumetric deformation is time independent. The Bulk modulus was then taken to be 4.54 GPa [33]. The shear relaxation modulus, *G*, of the polyurea was based on the quasi-statically derived master curve and implemented using the Prony series with constants identical to those provided in Knauss and Zhao [39]. The Prony representation of the shear modulus is

$$G(t) = G_0\left[\alpha_\infty + \sum_{i=1}^{n} \alpha_i exp\left(-\frac{t}{\tau_i}\right)\right] \tag{4.5}$$

where, *G(t)* is the relaxation shear modulus as a function of the relative moduli

$$\alpha_\infty = \frac{G_\infty}{G_0}, \qquad \alpha_i = \frac{G_i}{G_0} \tag{4.6}$$

and

$$G_0 = G_\infty + \sum_{i=1}^{n} G_i \tag{4.7}$$

with G_i representing the stiffness of the spring in the i^{th} branch and τ_i is the corresponding relaxation time constant of the same spring-dashpot pair. G_∞ is the long term shear modulus or steady state stiffness, derived from the material properties [38]. The value of the relative moduli and their associated time constants are given in Table 4.1.

Table 4.1: Relative shear moduli and corresponding time constant (s) for polyurea.

	1	2	3	4	5	6	7	8	9
τ_i	10^{-13}	$5X10^{-13}$	10^{-12}	10^{-11}	10^{-10}	10^{-9}	10^{-8}	10^{-7}	10^{-6}
α_i	0.036	0.036	0.036	$4.09X10^{-17}$	0.222	0.176	0.116	0.092	0.063

	10	11	12	13	14	15	16	17	18
τ_i	10^{-5}	10^{-4}	10^{-3}	10^{-2}	10^{-1}	1	10	10^{2}	10^{3}
α_i	0.042	0.037	0.019	0.016	0.010	0.008	0.005	0.005	0.009

The data provided in Table 4.1 was based on a master curve with reference temperature of 0°C, since laser-induced shock wave experiment is commonly done at room temperature, hence the time-temperature shift factor (a_T) according to the WLF equation was used [33].

$$log(a_T) = \frac{-C_1(T-T_r)}{C_2+(T-T_r)} \tag{4.8}$$

Where, T is the test temperature (herein was taken to be room temperature), C_1=8.86 and C_2=101.6.

Generally, unless otherwise noted in each of the following case study, the finite element model was spatially discretized with a uniform mesh and an element size of 15 µm, which was chosen to avoid internal wave reflection artifacts known to arise from non-uniform meshing. The non-dimensional quantity of the Courant-Friedrichs-Levy condition was used to calculate the time step to satisfy the standard numerical stability requirements based on the relationship between the element size (Δx), the wave speed of polyurea (c), and the time step (Δt), such that

$$CFL = \frac{c\Delta t}{\Delta \mathrm{x}}, \quad CFL \leq 1 \tag{4.9}$$

resulting in a time step of 2 ns at the expected strain rate of 10^6 s^{-1} [34,42–44].

The attributes of the stress profile resulting from the interaction of the high-energy pulsed laser with the sacrificial layer depend on the characteristics of the laser itself (e.g., energy, rise time, pulse duration, and wavelength) as described by Lindl's equation [45,46]. However, during the physical experiment, the stress profile is determined based on an interferometrically-measured free surface displacement [34]. Given the long history of the laser-induced shock wave experiment, e.g., [47], an idealized stress wave profile was used based on the previous experimental reports by Gupta *et al.* [33], regardless of the loading mode. The idealized input stress wave profile (σ_i), shown in Figure 4.1, can be described by

$$\sigma_i = -\frac{\rho c}{2}\left\{\gamma\left[exp^{\left(-\frac{t}{\alpha}\right)} - exp^{\left(-\frac{t}{\beta}\right)}\right]\right\} \tag{4.10}$$

where, ρ is the density of the substrate and c is the speed of sound of the material, while α, β, and γ are fitting parameters determined based on the interferometric displacement data. Here, γ=333 m·s^{-1}, α=16.5 ns, and β=6.7 ns were selected to generate the input wave shown in Figure 4.1.

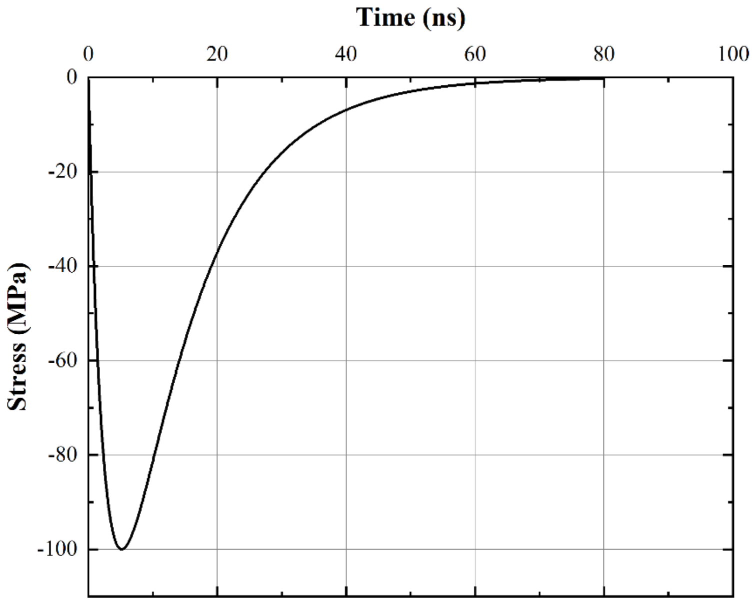

Figure 4.1: A general profile of the idealized input stress wave (Eqn. 10) with an amplitude of 100 MPa, rise time of 2.88 ns, and duration of 80 ns. This idealized profile is used as the input load due to laser-induced shock waves, simulating the propagation of pressure, surface, and shear waves independently.

Before embarking on the mechanical response of polyurea due to the propagation of different modes of stress waves, it is warranted to comment on the thermal effect due to the high-energy laser interaction with the sacrificial layer to create the stress wave. This is a common concern of novice investigators of this experimental protocol, given that the sacrificial layer undergoes rapid thermal expansion before exfoliating to launch the stress wave. Zhang *et al.* [48] recently performed a one-dimensional heat conduction analysis to elucidate the local increase in temperature in the sacrificial layer, and according to their results, the ablation layer surface can reach up to 5500 K. However, the poor thermal conductivity of polymers and the large time constant of the heat transfer process limit the effect of this increase in temperature to the surface of the test structure adjacent to the sacrificial layer.

Three case studies are reported below to explicate the separate and concurrent effect of pressure, shear, and surface waves on a 4 mm diameter plug of polyurea with a thickness of 0.5 mm. The first two case studies (propagation of pressure and surface waves, separately) employed a 2D axisymmetric model, where the corresponding boundary and loading conditions are shown in Figure 4.2. Two arbitrary points were fixed in all directions ($\boldsymbol{u} = 0$) to prevent rigid body motion during the simulation due to the imparting stress wave. The lateral sides of the polyurea plug were ascribed with low-reflecting boundary conditions to avoid reflection of the wave disturbance from these boundaries throughout the simulation; hence, the results discussed next are due to the propagation of the stress wave. The low-reflecting boundary condition tries to create a perfect acoustic impedance match by considering the material data from the adjacent domain so that

$$\boldsymbol{\sigma} \cdot n = -\rho c_p \left(\frac{\partial u}{\partial t} \cdot n \right) n - \rho c_s \left(\frac{\partial u}{\partial t} \cdot t \right) t \tag{4.11}$$

where, n and t are the unit normal and tangential vectors at the boundary, respectively, and c_p is the speed of the pressure wave while c_s is the speed of the shear wave [38]. For Case Study I, the input pressure wave was prescribed on the bottom surface (see Figure 4.2) using the stress wave profile shown in Figure 4.1 while the top surface was left traction-free. For the second Case Study (i.e., the propagation of surface waves), the stress wave was applied to the top surface in a ring-shaped spot while the bottom side was left traction-free in this scenario. The dimensions of the ring area are 800 μm in mean diameter and 100 μm thick.

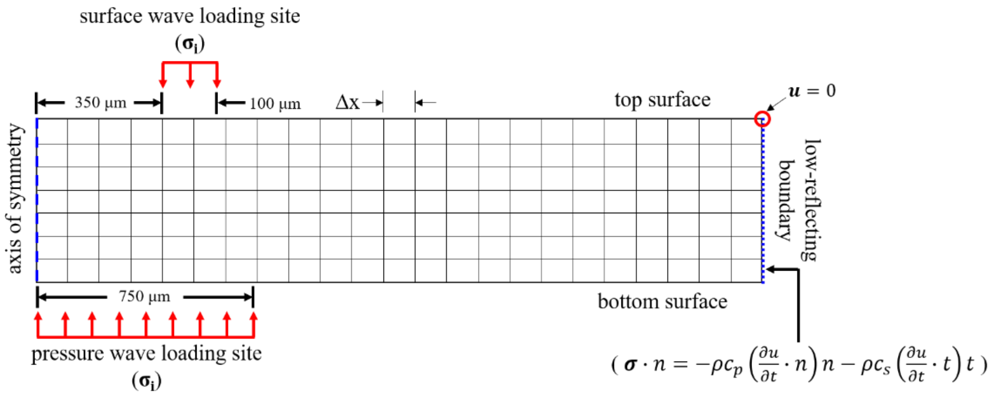

Figure 4.2: Schematic representation of the 2D axisymmetric model with the corresponding boundary conditions used in simulating the propagation of the pressure and surface waves in elastomeric polyurea due to laser-induced shock waves.

The final case study (propagation of shear waves) was performed using a 2D plane strain model. This modeling approach was taken due to the asymmetric propagation of the shear wave into the thickness of the simulated polyurea plug. The shear wave was applied at the bottom surface, with a spot size of 1.5 mm. The ratio of the loading site diameter to the thickness of the disc was consistent with previous studies [34]. The general details of the model and the material properties remain faithful to the description above, regardless of dimensionality or type of the propagating wave.

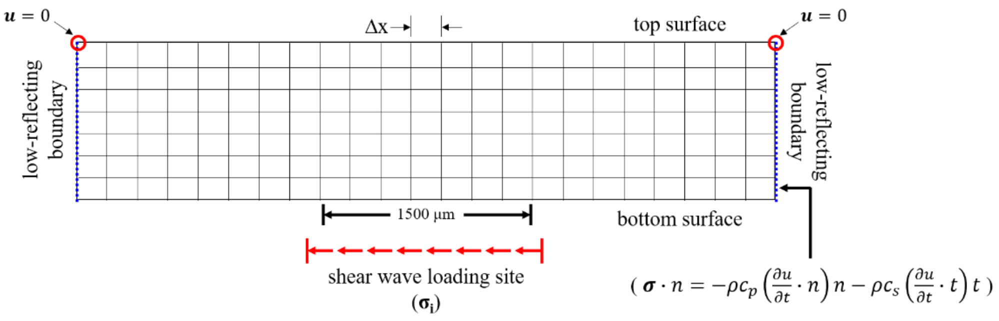

Figure 4.3: Schematic representation of the 2D model with the corresponding boundary conditions used in simulating the propagation of the shear waves in elastomeric polyurea.

The mapped mesh (displayed schematically in Figures 4.2 and 4.3) was selected to avoid nonlinear convergence behavior. A fully coupled iterative finite element solution with a fully coupled iterative solver was implemented while the displacement fields were calculated with the MUMPS linear system solver. Each successive solution step included an error estimate check to ensure solution convergence and accuracy.

4.3 Case Study I: Propagation of Pressure Waves

Figure 4.4 is a composite figure of the contour plots of the effective stress at different simulation times, ranging from 0 ns to 600 ns, and the corresponding line plots of the normal stress component as a function of time at different locations along the propagation path. The extracted initial amplitude of the pressure stress wave was 138.04 MPa, arriving at the free surface in 291 ns, which is in good agreement with the prediction based on the wave speed. The free surface reflection is a tensile wave moving at the same speed, still exhibiting some of the characteristics of the original wave while plowing through the solid during the forward trip. While the width-at-half-maximum (FWHM) and rise time of the original wave were 8.06 ns and 4.35 ns, respectively, the same attributes of the reflected wave were found to be 22.94 ns and 13.97 ns. The FWHM, rise time, and the amplitude of the wave as a function of travel distance are plotted in Figure 4.5, where the reflection off the free surface occurred after 300 ns.

The line plot results (Figure 4.4) and the corresponding wave attributes seen in Figure 4.5 indicate that the initial ~130 ns of the wave propagation exhibited an asymmetric response analogous to the initial wave profile, shown in Figure 4.1 as a rapid rise and slow decay. The steady reduction in the amplitude is attributed to the material dispersive nature, also exemplified in the broadening of the wavefront in the accompanying contour plot. The narrow and sharp wavefront continues to widen as the wave propagates forward. This broadening effect is also exhibited in the reflected wave as it travels towards the bottom surface. As the wave crosses the ~130 ns temporal milestone, it experiences a conversion from an asymmetric to symmetric wave, as depicted in the wave profiles shown in Figure 4.4. The conversion is marked by a sudden change in the wave attributes, including the amplitude, rise time, and FWHM, as exhibited in Figure 4.5. Similar to the pre-conversion stage, the amplitude appears to decrease at nearly the same rate again due to the dispersive behavior of the material.

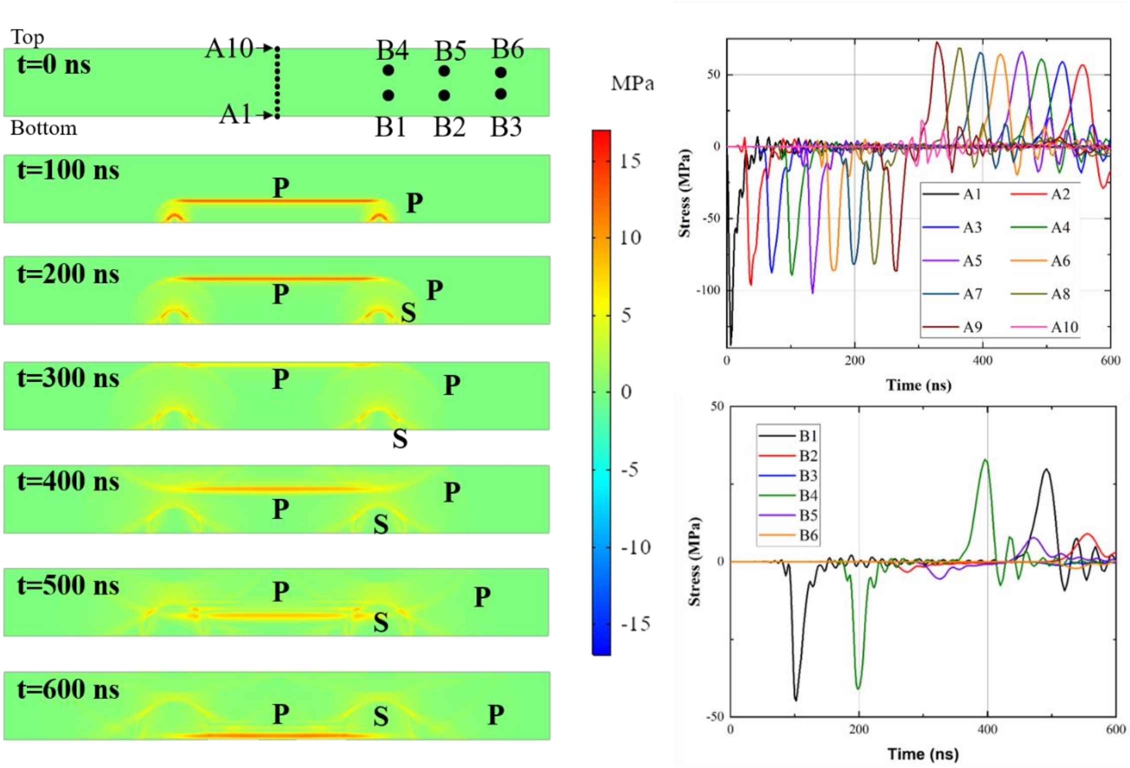

Figure 4.4: (left panel) contour plots of the effective stress due to the propagation of the pressure wave in elastomeric polyurea due to laser-induced shock waves, showing the flat pressure wavefront and the accompanying spherical wavefronts. (right panel) Line plots of the normal stresses extracted at different axial and lateral locations to demonstrate the dispersion and attenuation of the wave as it traverses the thickness of the plug.

The results in Figure 4.4 manifest two additional observations. First, the reflected wave, as expected, has a tensile sense after encountering the top free surface. This tensile wave loads the sample in a uniaxial state of stress, resulting in spallation if the amplitude exceeds the cohesion strength of the material. The amplitude of the reflected tensile wave in this case study was found to be 65.55 MPa, which is below the limit set before in [34] for the dynamic strength of polyurea. If such behavior is of interest, contrary to the objective of the current study, the amplitude of the input wave needs to increase, so the reflected tensile wave has enough momentum to fail the material catastrophically incrementally. It is worth noting that the cohesion limit is set experimentally by increasing the laser energy fluence while monitoring the free surface displacement interferometrically to deduce the input stress profile. Second, the contour plots show that the wavefront edges start to radiate away in spherical patterns at the same speed as the main wave. After a significantly delayed time, a trailing shear wave starts to nucleate at the edges of the original input location and radiates into the bulk of the solid in spherical patterns. The effect of the shear waves on the roundtrip of the pressure wave can be deduced from Figure 4.4, where the amplitude of the detected wave from the lateral direction is comparable to the wave originating from the interaction of the laser with the sacrificial layer. The spherical waves, at a propagation time between 400 ns and 500 ns, and the reflected tensile wave start to interact with the trailing shear waves, hence, loading this region of the sample multiaxially. The reflected tensile wave will first encounter its wake, or the trailing spherical waves originating from the edges still carrying the original compressive sense. Such interaction results in interference that will modify the purity of the tensile wave and reduce its amplitude. Subsequently, the reflected tensile wave will encounter the shear waves with the spherical front that had started from the edges of the loading site.

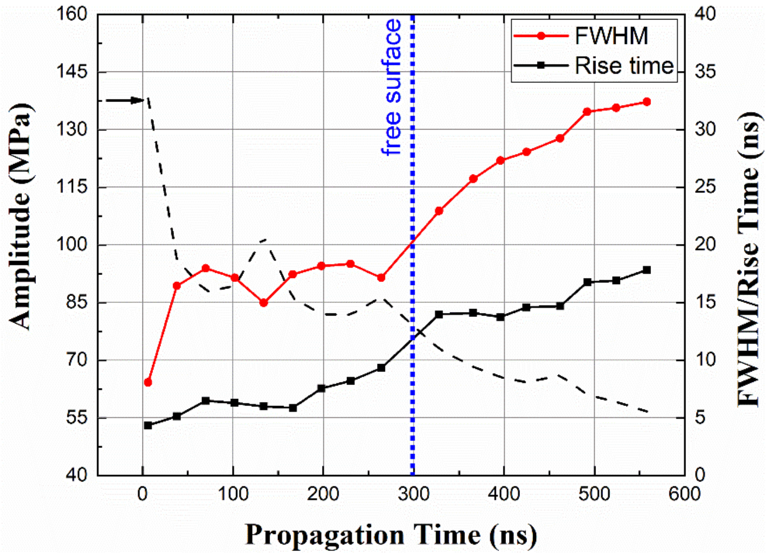

Figure 4.5: Wave attributes as a function of the propagation time of the pressure wave, including the amplitude in MPa, the full-width-at-half-maximum in ns, and the rise time in ns.

<u>4.4 Case Study II:</u> Propagation of Surface Waves

Figure 4.6 presents a series of contour plots of the shear (left panel) and normal (right panel) stress components, extracted from the simulation of the propagation of surface waves up to 600 ns at 200 ns increments. Veysset *et al.* recently showed that the high energy laser spot could be reshaped into a ring, which upon the interaction with a blanket gold film, resulted in the propagation of surface waves along the free surface, causing failure at the center of the ring due to the focusing of the inwardly propagating surface waves [49]. Notably, the illumination of the laser on the metallic film also launches pressure and shear waves that travel into the bulk of the substrate towards the bottom surface. The slower shear wave can be seen (Figure 4.6a) propagating in the same direction as the initial pressure wave after ~100 ns in a spherical pattern. The pressure wave travels at a speed of 1750 $m\cdot s^{-1}$, while the shear wave moves at a slower speed of 415 $m\cdot s^{-1}$. The Rayleigh (c_R) surface wave speed is $c_R = c_s(0.87 + 1.12\nu)/(1 + \nu)$ or ~95% of the shear wave speed based on the Poisson's ratio listed in the previous section [50]. The interaction between the high-energy laser and the sacrificial layer results in a Rayleigh wave, and bulk pressure and shear waves.

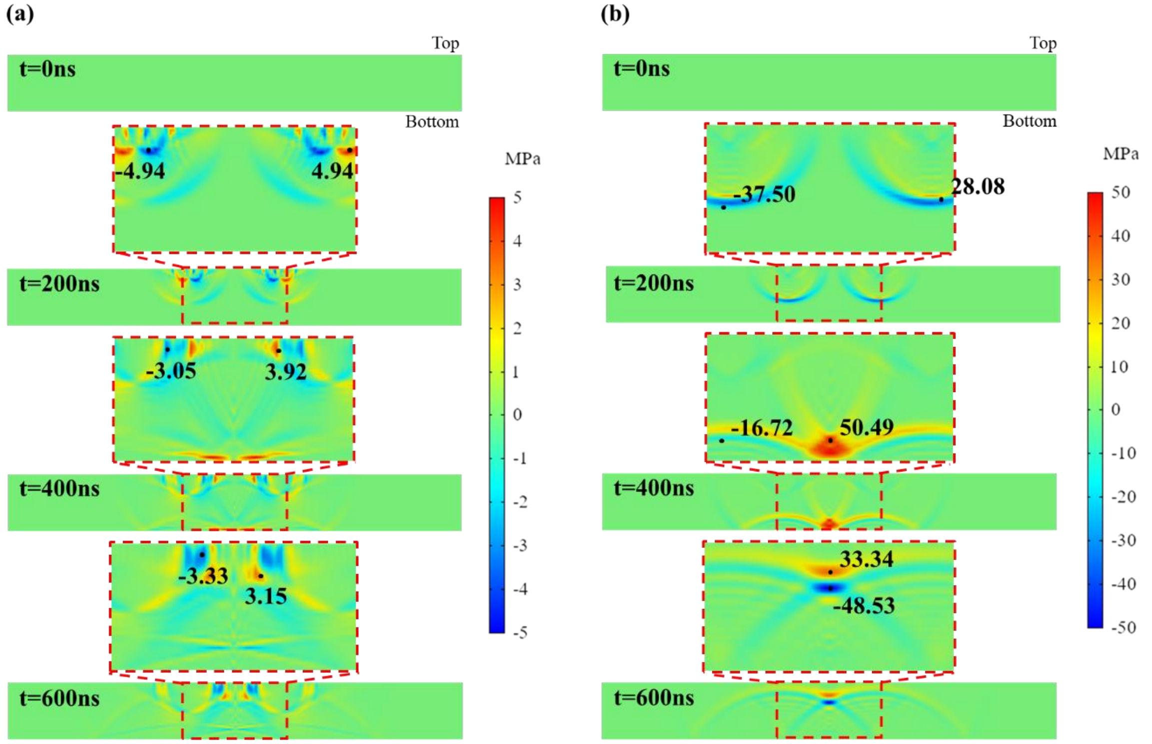

Figure 4.6: Contour plots of the (a) shear and (b) normal stress components due to the propagation of the surface wave (all listed stress numbers are in MPa) at different propagation times ranging from the onset of the simulation (top panel) to 600 ns (bottom panel). The central region at each simulation time is emphasized to better visualize the wave-to-wave interactions.

Two noteworthy observations can be discussed based on the contour plots in Figure 4.6. First is the propagation pattern of the Rayleigh waves. As seen from the 200 ns contour plot of Figure 4.6a, the shearing at the edges of the inner and outer diameter of the ring are initialized in the opposite directions. Over time, the waves develop into circular patterns that are entrapped on the surface, thus creating a propagation of Rayleigh waves radiating from the inner and outer diameters. The waves emanating from the inner diameter converge, where the surface wave stresses combine, creating a concentrated value at the center (site of interest, e.g., the experimental work of Veysset *et al.* [49]). The waves radiating from the outer diameter travel away from the center and towards the low-reflective boundaries, where the roundtrip of any remnant reflections is beyond the simulation time and is not of interest in the current study. It is worth noting that while emphasis was given to the waves sourcing from the inner and outer edges of the ring towards the center or the low-reflective boundaries, respectively, the waves also travel laterally in the other directions. Second is the pressure wave interactions (Figure 4.6b) with the shear waves (Figure 4.6a) propagating through the bulk of the material. In this case, the wave propagation scenario discussed in Case Study I is recovered since focusing the laser on the surface of the ring launches a compressive wave into the bulk underneath the illuminated surface, similar to the traditional loading scenario laser-induced shock wave experiment.

Here, the utility of the current computational study is illustrated for the future design of experiment studies through two unique loading conditions. If a pure surface loading is desirable due to the propagation of Rayleigh waves, one must set the mean diameter of the ring and the thickness of the plug symbiotically, where the mean diameter dictates the time required for the arrival of the Raleigh waves to the center (i.e., site of pure loading) while the thickness of the plug sufficiently delays the roundtrip of the pressure waves. On the other hand, a combined loading can also be guaranteed by strategically violating the abovementioned symbiotic relationship between the mean diameter and plug thickness. A secondary byproduct of the results presented in Figures 4.6a and b is the clear visualization of the interactions between the bulk waves. Contrary to Case Study I, the illumination of a ring-shaped geometry generates stress waves with a torus shape wavefront instead of a flat wave; thus, two areas of initial pressure wave propagations were created. The pressure waves originating from the loaded site start to interact with one another at

~300 ns, at which time the tensile wave at the axial center of the polyurea plug continues to travel towards the bottom free surface, reflecting as a compressive wave at the free surface. This reflected compressive wave traveling towards the top surface encounters the sequential shear wave, starting from the loading site at >400 ns. The rendezvous location may be of experimental interest since it is positioned within the bulk of the material while under the influence of a multiaxial loading scenario. The amplitude of the pressure wave can be amplified by concurrently combining the loading scenarios from Case Studies I and II, which can strategically be done by delaying the release of the pressure wave to coincide with the arrival surface wave. Example results of the latter are included in Appendix 4A.

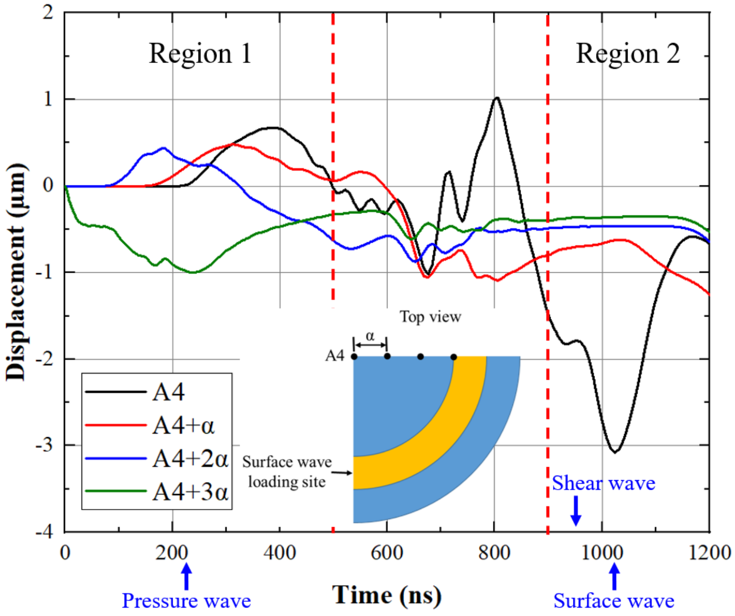

Figure 4.7: Displacement as a function of time at different locations on the top surface where α = 116.7 μm. The inset shows the location of the four points with respect to the laser-illuminated ring.

Figure 4.7 is a plot of the out-of-plane, normal displacement component corresponding to four points on the top surface (see inset in Figure 4.7) as a function of time. These four points were selected to range between the inner diameter and the center of the laser-illuminated ring. The displacement-time history in Figure 4.7 can be divided into two regions, where region one covers up to 500 ns while region two extends beyond 900 ns. The compressive nature of the induced shock wave produces a negative displacement, i.e., a displacement into the bulk of the material at the inner rim of the ring, whereas the remaining points undergo a positive displacement due to volume conservation. With an emphasis on the displacement-time history of the point coinciding with the inner diameter of the ring (A4+3α point shown in the inset in Figure 4.7), the response starts to increase at a rate of 23 $m \cdot s^{-1}$ until it reaches a displacement of 0.45 μm within 20 ns, at which point it reaches a plateau that persists for ~60 ns. At the outset of the plateau region at 80 ns, the displacement commences to increase once more, but at a slower rate of 5 $m \cdot s^{-1}$. It is believed that the initial increase in the displacement at the beginning of the simulation time is attributed to the release of the pressure waves into the solid, while the subsequent increase is associated with the arrival of the accompanying shear waves. This observation can be substantiated by the temporal duration of the plateau, where the outset was fourfold of the inset and the rate of increase was maintained the same proportion, i.e., the same as the ratio between the pressure and shear wave speeds. The simulation was able to capture another behavior of the displacement-time history on the surface, which is the increase in the amplitude of the displacement as a function of the radial position. The increase in the amplitude is also accompanied by the peaks broadening, consistent with the response of the structure to plane waves due to an impulse loading and the focusing due to the convergence of the wave towards the center [51]. Similar to the response at point A4+3α, the onset of the peaks at the remaining points away from the inner diameter at 76 ns, 152 ns, and 216 ns, respectively, are due to the propagation of the pressure wave traveling at a speed of 1750 $m \cdot s^{-1}$. As previously noted, the Rayleigh surface wave travels at speed slower than the bulk waves (i.e., pressure and shear), ~394 $m.s^{-1}$; hence, the deformation observed at the region centered at 1050 ns corresponds to the propagation of the Rayleigh wave reaching the center of the loaded site.

4.5 Case Study III: Propagation of Shear Waves

The contour plots in Figure 4.8 are based on the application of ultrahigh rate shear traction at the bottom surface (see Figure 4.3) with the characteristics of the idealized stress profile shown in Figure 4.1 and described by Equation 4.10. The release of the initial shear wave quickly evolves into three different wave types occupying the simulated plug: namely, a shear wave progressing vertically towards the top surface (S_V), another shear wave (S_H) orthogonal to the S_V wave moving towards the side boundaries, and a pressure wave (P) ahead of the S_V wave. The primary S_V wave and secondary S_H wave travel at the same shear wave speed, while the P wave moves faster. The latter can reverberate several times within the solid during the same time window the S_V wave makes a complete one-way trip towards the top surface. Hence, the reflected P wave interferes with the S_V wave first, followed by a subsequent interference with the S_H wave as it approaches the bottom surface. Since the P wave originates from the edges of the loading site, it propagates at only a fraction of the shear stress amplitude at 45° while developing into a spherical wavefront, as shown in Figure 4.8b. It is worth noting that the sense of the P wave is asymmetric about the central axis of the plug, where it has a positive tensile amplitude on the left (i.e., red color wavefront) and a negative compressive amplitude on the right (i.e., blue color wavefront) during the forward trip towards the top surface. Upon reflection from the free, top surface, the tensile and compressive waves interact (shown in the panel corresponding to t=600 ns in Figure 4.8b), resulting in interference patterns at 45° angle from the propagation direction, which may develop in physical samples as shear bands. While the interference patterns are dramatized in the contour plots in Figure 4.8b (observe the denoted amplitudes at maximum red and blue areas), they appear to be inferior to the amplitude of the S_V and S_H waves. The shear stresses due to the propagation of the shear waves dominate the response. The more the P wave reverberates between the top and bottom surfaces and interacts with the shear waves, the less apparent its effects become due to the destructive nature of the interference.

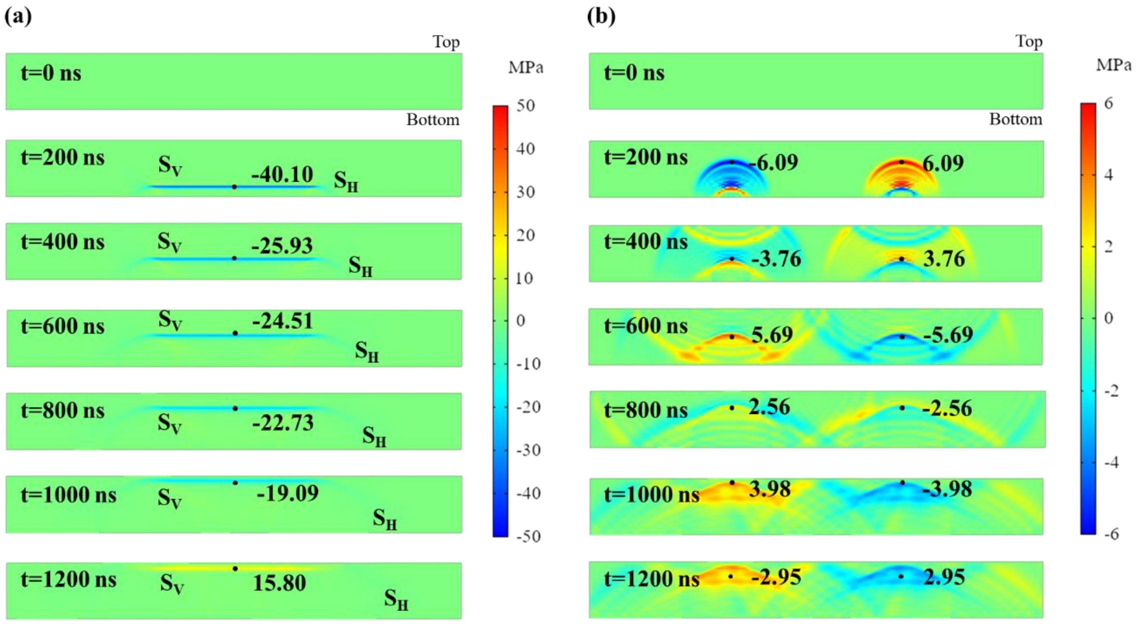

Figure 4.8: Contour plots of the (a) shear and (b) normal stress components as a result of the propagation of the shear wave, starting from the bottom surface, due to laser-induced shock waves with idealized profile described in Eqn. 4.10. The results are based on the model with the boundary conditions shown in Figure 4.3, where the stress numbers are in MPa.

Two final comments are warranted based on the contour plots in Figures 4.8a and b. First, the color alternations in the spherical propagation patterns of the P wave are associated with the areas in the sample under tensile stress adjacent to areas in compression (i.e., alternating blue and red regions along the wavefront). This alternation is evident at later simulation times upon the S_V wave interference, as the returning P wave is locally equilibrating the slowly propagating S_V wave. Second, the wavefront of the S_V wave appears to be broader than its counterpart from the pressure wave discussed in Case Study I, a result of the slow rate of propagation of the shear wave into the viscoelastic polyurea. As the shear wave plows through the thickness of the polyurea plug at a rate of 415 $m \cdot s^{-1}$, it activates additional and slower Prony elements that correspond to a compliant mechanical response, e.g., the relative shear modulus at a short-time Prony element is higher than a later and longer time element (see Table 4.1). In effect, the slow shearing rate extends the presence of the response and, in turn, broadens the peak. Such peak broadening can be clearly observed by comparing the FWHM values in Figure 4.9 based on analysis of the results from the current case study with those in Figure 4.5 from Case Study I. The FWHM of the shear waves slowly increased as a function of propagation time and axial location, changing from 14.96 ns for the initial wave to 67.64 ns in the shear wave approaching the top surface. The peak broadening was also associated with a steady decrease in the amplitude, where it changed from 128.23 MPa for the input wave to 19.79 MPa for the wave near the top surface. The significant reduction in the amplitude over the 0.5 mm thickness is attributed to the quality factor of wave propagation in viscoelastic media, highlighting the impact mitigating properties of polyurea as reported in [33]. The destructive interferences between the fast and reverberating P wave and the S_V also reduces the amplitude.

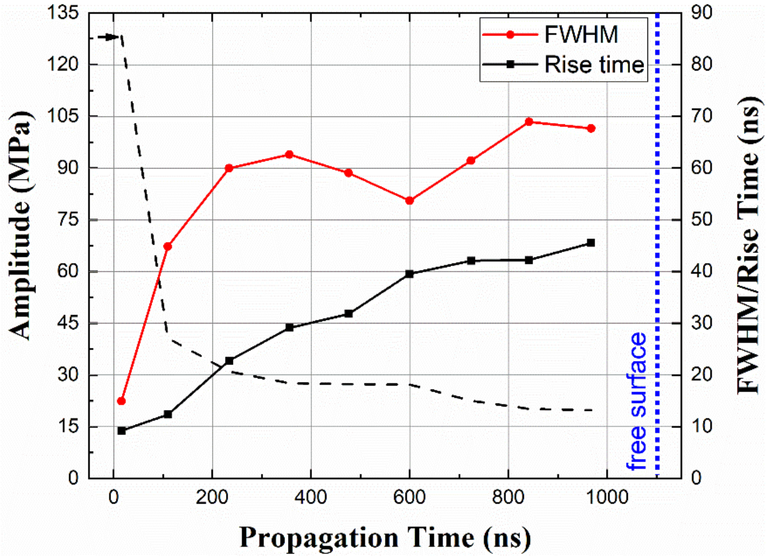

Figure 4.9: Wave attributes as a function of the propagation time of the shear wave, including the amplitude in MPa, the full-width-at-half-maximum in ns, and the rise time in ns.

4.6 Conclusion

A computational model was constructed and solved to explicate the full-field response of viscoelastic solid, e.g., polyurea, with laser-induced shock waves, emphasizing on the shock front. Three case studies were considered, elucidating the response of polyurea to pressure, shear, and surface waves when applied separately. The results indicate that the actual loading due to these ultrahigh strain waves is far more complicated than accurately captured by analytical elastodynamic solution. The results also provided an insight into the duration when the shock wave travels alone with a distinct wavefront and when the waves start interacting, leading to multimode loading, even if the objective was otherwise. Several strategies are discussed to tune the time of arrival of different wave types, which can be very beneficial to an experimentalist work in this area during the design process. Overall, the computational results demonstrated that the purity of the loading type would depend on the geometrical configuration and delay of concurrent input waves. Despite the application of a pure pressure, surface and shear wave, the interference of the accompanying waves alters the characteristics such as amplitude, pulse width, and rise time of the initial stress profile. In general, in-silico experimentation of multimode shock waves can be done prior to or in tandem with the physical experiment to determine parameters such as geometrical dimensions, loading type, etc., depending on the targeted failure mechanism or stress state.

Acknowledgement

Chapter 4, in full, is a reprint of the material as it appears in International Journal of Mechanical Sciences 2021. Gamez, Carlos; Huynh, Nha Uyen; Youssef, George, Science Direct, 2021. The dissertation author was the secondary investigator and author of this paper.

References

1. Mal, A. K., Banerjee, S. & Gupta, V. Measurement of thin film interfacial properties using nanosecond laser source. *Heal. Monit. Smart Nondestruct. Eval. Struct. Biol. Syst. V* **6177**, 61770Y (2006).

2. Youssef, G., Moulet, C., Goorsky, M. S. & Gupta, V. Inter-wafer bonding strength characterization by laser-induced shock waves. *J. Appl. Phys.* **111**, (2012).

3. Youssef, G. & Gupta, V. Resonance in Polyurea-Based Multilayer Structures Subjected to Laser-Generated Stress Waves. *Exp. Mech.* **53**, 145–154 (2013).

4. Mumy, K. L. *Encyclopedia of Toxicology, 3rd Edition*. *Encyclopedia of Toxicology, 3rd Edition* (Academic Press, 2014).

5. Zhang, Y., Yang, C., Qiang, H. & Zhong, P. Nanosecond shock wave-induced surface acoustic waves and dynamic fracture at fluid-solid boundaries. *Phys. Rev. Res.* **1**, 33068 (2019).

6. Fan, Y. & Wang, J. Attenuation of Shock Waves using Perforated Plates Attenuation of Shock Waves using Perforated Plates. (2017) doi:10.1088/1757-899X/225/1/012059.

7. Tadese, B. D. Finite Element Modeling of Seismic Wave Propagation in Earthen Embankments. (University of Mississippi, 2012).

8. Ramesh, K. T. High Rates and Impact Experiments. in *Springer Handbook of Experimental Solid Mechanics* 929–960 (Springer US, 2008). doi:10.1007/978-0-387-30877-7_33.

9. Field, J., Walley, S., Proud, W. & Goldrein, H. Review of experimental techniques for high rate deformation and shock studies. *Int. J.* (2004).

10. Jiao, T., Clifton, R. J. & Grunschel, S. E. High strain rate response of an elastomer. *AIP Conf Proc* **845 II**, 809–812 (2006).

11. Sun, Y., Kooi, S. E., Nelson, K. A., Hsieh, A. J. & Veysset, D. Impact-induced glass-to-rubber transition of polyurea under high-velocity temperature-controlled microparticle impact. *Appl. Phys. Lett.* **117**, (2020).

12. Yuan, J., Gupta, V. & Pronin, A. Measurement of interface strength by the modified laser

spallation technique. III. Experimental optimization of the stress pulse. *J. Appl. Phys.* **74**, 2405–2410 (1993).

13. Pronin, A. N. N. & Gupta, V. Measurement of thin film interface toughness by using laser-generated stress pulses. *J. Mech. Phys. Solids* **46**, 389–410 (1998).

14. Gupta, V., Yuan, J. & Pronin, A. Recent developments in the laser spallation technique to measure the interface strength and its relationship to interface toughness with applications to metal/ceramic, ceramic/ceramic and ceramic/polymer interfaces. *J. Adhes. Sci. Technol.* **8**, 713–747 (1994).

15. Wang, J., Weaver, R. L. & Sottos, N. R. A parametric study of laser induced thin film spallation. *Exp. Mech.* **42**, 74–83 (2002).

16. Gupta, V., Argon, A., Cornie, J. & Parks, D. Measurement of interface strength by laser-pulse-induced spallation. *Mater. Sci.* (1990).

17. Vossen, J. L. Measurements of Film-Substrate Bond Strength By Laser Spallation. *ASTM Spec. Tech. Publ.* 122–133 (1978) doi:10.1520/stp38629s.

18. Raman, S. N., Ngo, T., Lu, J. & Mendis, P. Experimental investigation on the tensile behavior of polyurea at high strain rates. *Mater. Des.* **50**, 124–129 (2013).

19. Kim, H., Citron, J., Youssef, G., Navarro, A. & Gupta, V. Dynamic fracture energy of polyurea-bonded steel/E-glass composite joints. *Mech. Mater.* **45**, 10–19 (2012).

20. Hu, L. *et al.* Cell adhesion measurement by laser-induced stress waves. *J. Appl. Phys.* **100**, (2006).

21. Miller, P., Hu, L. & Wang, J. Finite element simulation of cell-substrate decohesion by laser-induced stress waves. *J. Mech. Behav. Biomed. Mater.* **3**, 268–277 (2010).

22. Youssef, G. *et al.* The influence of laser-induced nanosecond rise-time stress waves on the microstructure and surface chemical activity of single crystal Cu nanopillars. *J. Appl. Phys.* **113**, (2013).

23. Colorado, H. A. *et al.* Ultrahigh strain-rate bending of copper nanopillars with laser-generated shock waves. *J. Appl. Phys.* **114**, (2013).

24. Barsoum, R. G. S. & Dudt, P. J. The fascinating behaviors of ordinary materials under dynamic conditions. *Ammtiac Q* **4**, 11–14 (2010).

25. Grujicic, M. *et al.* Experimental and Computational Study of the Shearing Resistance of Polyurea at High Pressures and High Strain Rates. *J. Mater. Eng. Perform.* **24**, 778–798 (2015).

26. Jiao, T., Clifton, R. J. & Grunschel, S. E. Pressure-sensitivity and constitutive modeling of an elastomer at high strain rates. *AIP Conf. Proc.* **1195**, 1229–1232 (2009).

27. Youssef, G. & Whitten, I. Dynamic properties of ultraviolet-exposed polyurea. *Mech. Time-Dependent Mater.* **21**, 351–363 (2017).

28. Youssef, G. & Reed, N. Scalable Manufacturing Method of Property-Tailorable Polyurea Foam. (2017).

29. Mock, W., Bartyczak, S., Lee, G., Fedderly, J. & Jordan, K. Dynamic properties of polyurea 1000. *AIP Conf. Proc.* **1195**, 1241–1244 (2009).

30. Roland, C. M., Twigg, J. N., Vu, Y. & Mott, P. H. High strain rate mechanical behavior of polyurea. *Polymer (Guildf).* **48**, 574–578 (2007).

31. Sarva, S. S., Deschanel, S., Boyce, M. C. & Chen, W. Stress-strain behavior of a polyurea and a polyurethane from low to high strain rates. *Polymer (Guildf).* **48**, 2208–2213 (2007).

32. Shim, J. & Mohr, D. Using split Hopkinson pressure bars to perform large strain compression tests on polyurea at low, intermediate and high strain rates. *Int. J. Impact Eng.* **36**, 1116–1127 (2009).

33. Youssef, G. H. Dynamic Properties of Polyurea. (University of California, Los Angeles, 2010).

34. Youssef, G. & Gupta, V. Dynamic tensile strength of polyurea. *J. Mater. Res.* **27**, 494–499 (2011).

35. Gupta, V. Adhesive and ultrahigh strain rate properties of polyurea under tension, tension/shear, and pressure/shear loadings with applications to multilayer armors. in *Elastomeric Polymers with High Rate Sensitivity: Applications in Blast, Shockwave, and*

Penetration Mechanics 1–411 (2015). doi:10.1016/C2013-0-19258-6.

36. Youssef, G. & Gupta, V. Dynamic response of polyurea subjected to nanosecond rise-time stress waves. 317–328 (2012) doi:10.1007/s11043-011-9164-7.

37. Gamez, C. Failure mechanisms of polyurea under high strain-rate. vol. 1 (University of California Los Angeles, 2017).

38. COMSOL Multiphysics. COMSOL Documentation. *Comsol Software.* (2014).

39. Knauss, W. G. & Zhao, J. Improved relaxation time coverage in ramp-strain histories. *Mech. Time-Dependent Mater.* **11**, 199–216 (2007).

40. Qiao, J., Amirkhizi, A. V., Schaaf, K., Nemat-Nasser, S. & Wu, G. Dynamic mechanical and ultrasonic properties of polyurea. *Mech. Mater.* **43**, 598–607 (2011).

41. Whitten, I. & Youssef, G. The effect of ultraviolet radiation on ultrasonic properties of polyurea. *Polym. Degrad. Stab.* **123**, 88–93 (2016).

42. Stampfli, R., Newacheck, S. & Youssef, G. Fully-coupled Computational Modeling of the Dynamic Response of 1-3 Multiferroic Composite Structures. *Int. J. Mech. Sci.* **191**, (2021).

43. Massachusetts Institute of Technology. Stability of Finite Difference Methods. *Numer. Fluid Mech. Lect. Notes* 75–81 (2009).

44. Kinsler, L. E., Frey, A. R. & Bennett, G. S. *Fundamentals of Acoustics*. (Wiley, 1982).

45. Ready, J. F. Effects due to absorption of laser radiation. *J. Appl. Phys.* **36**, 462–468 (1965).

46. Ready, J. Industrial applications of lasers. in (1997).

47. Gupta, V., Argon, A. S., Parks, D. M. & Cornie, J. A. Measurement of interface strength by a laser spallation technique. *J. Mech. Phys. Solids* **40**, 141–180 (1992).

48. Zhang, Y., Zhang, D., Wu, J., He, Z. & Deng, X. A thermal model for nanosecond pulsed laser ablation of aluminum. *AIP Adv.* **7**, (2017).

49. Veysset, D. *et al.* Acoustical breakdown of materials by focusing of laser-generated Rayleigh surface waves. *Appl. Phys. Lett.* **111**, (2017).

50. Graff, K. F. *Wave motion in elastic solids*. (Dover Publications, 1975). doi:10.1016/0003-682x(77)90009-3.

51. Medick, M. A. On classical plate theory and wave propagation. *J. Appl. Mech.* **28**, 223–8 (1961).

Appendix 4A: Propagation of Surface and Pressure Wave

For the surface and pressure wave case, the same boundary conditions of the 2D axisymmetric finite element model apply (see Figure 4.2). In addition to that, the stress wave that was applied to the bottom surface was delayed by 500 ns with respect to the stress wave applied on the top surface. The delay was introduced to ensure simultaneous arrival of the pressure and surface waves at the top surface. A composition of the contour plots of the effective stress at different simulation times and the corresponding line plot of the normal stress component as a function of time is shown in Figure 4.A1.

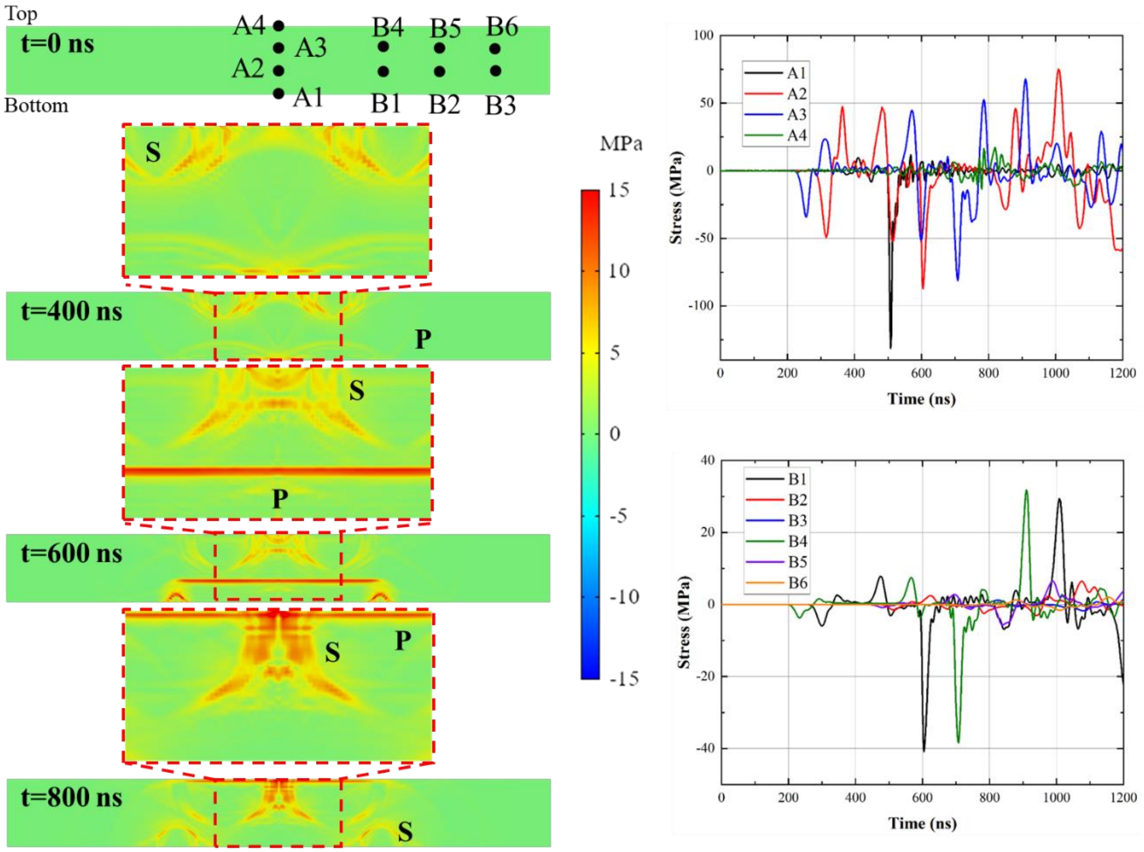

Figure 4.A1: Concurrent propagation of the surface and pressure wave in elastomeric polyurea due to delayed release of pressure and surface waves to guarantee arrival at the site of interaction simultaneously. The loading and boundary conditions are shown in Figure 4.2.

Appendix 4B: Propagation of Pressure and Shear Wave

The propagation of pressure and shear waves were also studied, where the boundary conditions are shown in Figure 4.3. The stress wave was applied at the bottom of the plug while the release of the pressure wave at the same loading site was delayed by ~800 ns. Figure 4.B1 is a composite figure of the contour plots of the effective stress at different simulation times, ranging from 0 ns to 1200 ns, and the corresponding line plot of the normal stress component as a function of time at different locations along the propagation path.

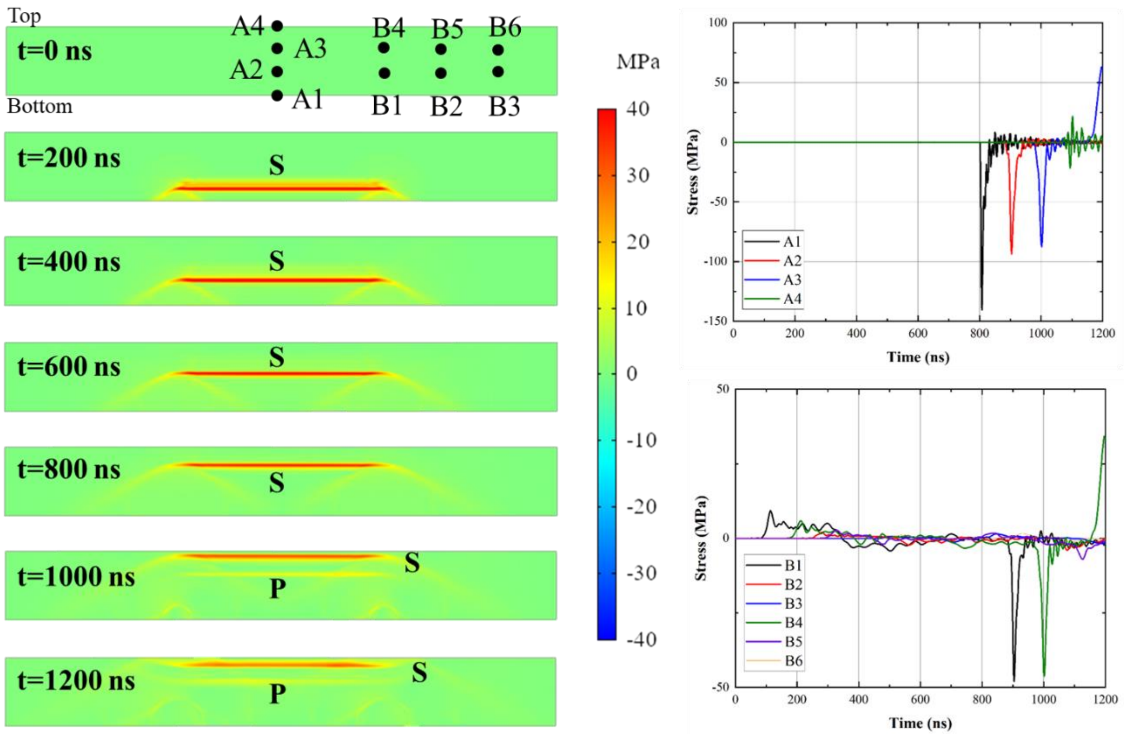

Figure 4.B1: Concurrent propagation of the pressure and shear wave in elastomeric polyurea plug due to ultrahigh strain rate laser-induced shock waves based on the release of delayed pressure and shear waves to ensure simulations arrival at the top surface.

CHAPTER 5

Light-matter interactions revealing load-induced phase mobility in elastomers

Nha Uyen Huynh[1], Behrad Koohbor[2], and George Youssef[1,*]

[1]Experimental Mechanics Laboratory, Mechanical Engineering Department, San Diego State University, San Diego, CA 92182, USA

[2]Department of Mechanical Engineering, Rowan University, 201 Mullica Hill Rd., Glassboro, NJ 08028, USA

Abstract

Elastomers with segmental microstructure have been a fascinating class of shock-tolerant and impact-resistant materials, but the technological potential remains untapped due to an ambiguous understanding of the molecular contributions to their superior mechanical behavior. Here, we leverage *in-situ* light-matter interactions to reveal the extent of microstructural mobility by temporally exploiting molecular processes during creep response. The segmental microstructure comprises aliphatic hard domains embedded within an aromatic soft matrix. High-resolution digital image correlation revealed the development of strain striations, mild-anisotropy, and the mechanisms responsible for domain mobilities, where the rate of hard segment mobility was found to be 60% slower than that of the soft segment. Terahertz spectral analyses pinpointed the contributions of interchain hydrogen bonding of the hard segments and the significant conformational changes to the soft segments at ~1.2THz and ~1.67THz, respectively. Moreover, the domain mobility was examined using experimental and computational light scattering approaches, uncovering dynamic scattering and elucidating the difference in the complex refractive index of the soft and hard segments. Our study unlocks the pathway for quantitative measurements of elusive molecular mobility and conformational changes during mechanical loading and sheds the light on the origin of the shock tolerance in some elastomeric polymers with segmental microstructure.

Keywords: terahertz-based characterization, creep response, elastomers, diffraction, polyurea

***Corresponding author:** gyoussef@sdsu.edu

5.1 Introduction

The fundamental understanding of the dynamic behavior of elastomeric polymers, especially those with segmental microstructure, is crucial for their utility in impact mitigation structures and protective paddings, reducing the severity of collisions whether in loading due to hypervelocity projectiles or due to biomechanical impacts [1,2]. The efficacy of elastomers in dissipating and absorbing the impact energy stems from multiscale deformation mechanisms, ranging from the molecular scale (*e.g.*, relative conformational mobility) to the mesoscale exemplified in segmental motions and to the microscale imbued in strain localization [3,4]. In past studies, various mechanisms have been proposed at each of these scales, and some have been experimentally or theoretically investigated, *e.g.*, the nanoscale and microscale properties of polyurea, a thermoset elastomer, in pursuit of explaining its remarkable dynamic attributes [5,6]. These mechanisms include dynamic glass-transition shifting (*e.g.*, Vogel-Fulcher-Tammann law), reversible in-operando pseudo-plasticization, deformation localization at soft/hard segment boundaries, significant mobility of the soft segment (up to plastic flow), and increased shear coupling as a function of compressive loading [7–9]. However, probing these mechanisms remains experimentally challenging due to the dichotomy in the timescale at which they occur, the lack of viable approaches, or the deformation exaggeration based on the compliant properties of elastomers.

In addition to comprehensive, advanced mechanics investigations, first steps have been made to experimentally interrogate this class of materials using novel spectroscopic techniques, pointing to drastically different molecular mechanisms responsible for the unique fundamental dynamic behavior of polyurea elastomers [7,10,11]. At low strain rates and ultrahigh compressive stresses, the material was found to vitrify due to the over confinement of the chains based on its incompressible behavior, demonstrated in a substantial increase in the bulk modulus. The latter was measured non-invasively using Brillouin spectroscopy while submitting the material to static ultrahigh pressures up to 13.5GPa using a diamond anvil cell [12]. The phase transformation associated with vitrification corresponds to pressure-driven glass transition, although the material was tested at room temperature, where it is expected to behave as a ductile polymer, *i.e.*, within the rubbery regime [12]. Furthermore, the increased intermingling of the hard and soft segments was reported in polyurea when submitted to hydrostatic compression exceeding 1GPa, irrespective of the stoichiometric composition of the segregated microstructure [13]. The increased hard/soft segments affiliation was associated with elastic contraction of the mean spacing of the interchain hydrogen-bonded hard segments as observed by *in-situ* X-ray scattering. Here, the length of the soft segment plays a crucial role in deformation and recovery processes [13]. This hierarchical architecture is also attributed to strengthening mechanisms at the nanoscale and is responsible for the scale-dependent relaxation and dissipation contrivances associated with dynamic loading scenarios [14]. These nanoscale processes are also directly linked to the remarkable improvement in the dynamic toughness of polyurea and are forecasted to apply to the broader class of elastomeric polymers.

On the other hand, polyurea, unexpectedly, exhibited irreversible plastic deformation combined with signs of adiabatic shearing when tested at ultrahigh strain rate, *ca.* 10^7 s^{-1}, using laser-induced shock waves [7]. The latter loading mechanism commonly results in brittle failure exemplified in partial or total spallation since all inelastic and time-dependent relaxation and deformation processes are suppressed by the exceptionally high loading rate, preventing relative chain motions. The shock-driven plasticization was associated with conformational changes related to hydrogen bonds vibrations, detected using terahertz-based spectroscopy (THz-S). The detection of hydrogen-bond vibrations using THz-S was motivated by the transparency of polymers to the low photon energy of the terahertz regime (0.4 – 40meV), allowing for the nondestructive and nonionizing interrogation of the urea linkages. Furthermore, the shock loading resulted in changes and disappearances of spectral peaks associated with the torsional motion of the interchain hydrogen bonds below 1.5THz, which were only evident after ultrahigh strain loading [7]. The sensitivity of terahertz waves to spectral changes due to underlying conformational changes can be exploited to elucidate the molecular processes responsible for the improved mechanical response of these elastomeric polymers, resembled in polyurea. Therefore, the interchain hydrogen bonds are responsible for the reversible elastic deformation (detected using X-ray scattering spectroscopy) and linked to irreversible plastic changes (revealed using THz-S).

Theoretically, molecular dynamic (MD) simulations attempted to explicate the molecular mechanisms responsible for the resilience and shock-tolerance of polyurea at the atomistic resolution [15–18]. Notably, the predictions of MD-based investigations are eclipsed by the complex, phase-segregated, and hierarchical architecture of polyurea, further exaggerated by its heavily cross-linked molecular structure, which is challenging to replicate in the simulation environment. Using a *no-reactive force field*, MD simulation computed the shock Hugoniot of polyurea, but only in the absence of voids and hard domains (not included in computations to lessen the computational burden but at the expense of physicality), which drastically differs from experimental observations of void collapse and hard domains mobility [18]. Furthermore, MD simulations forecasted the shock energy dissipated associated with adiabatic heating; some experimental evidence of this mechanism was recently reported on the surface of shock-loaded polyurea films [7]. Furthermore, quantum MD simulations revealed that polyurea structure remained intact under 35.7GPa but liquefied when the shock pressure increased beyond this limit. Two common limitations of these MD results are (1) limited experimental data due to a gap in physical testing to probe the materials under similar simulation conditions, and (2) the simulations only make assertions about reduced structure (*e.g.*, soft or hard segments or absence of interchain bonding). Hence, novel experimental approaches are imperative to probe these mechanisms within the realistic realm of the complex structure of elastomeric polymers.

In this context, we have studied the dynamic mechanical response of polyurea using a multifaceted characterization approach, targeting the behavior at the molecular, meso, and microscales. At the molecular scale, we exploit the unique capabilities of THz-S in revealing dynamic mechanical loading-induced conformational changes, including interchain hydrogen bonds. At the mesoscale, the light-polymer interactions with hierarchal chain arrangements as it trespasses the sample thickness results in diffraction, linked to recrystallization. The deformation was analyzed using a digital image correlation (DIC) approach to quantify the in-plane strains and rotations.

5.2 Full-Field Dynamic Strain Evolution

The time-dependent creep response of polyurea, extracted using digital image correlation (Fig. 5.1a), is shown in Fig. 5.1b, where the temporal in-plane normal (*i.e.*, axial, ε_y, and lateral, ε_x) strains, rotation (ω), and shear (ε_{xy}) strains are plotted with time up to ~1800s. Initially, the material undergoes primary creep, where the strain grows exponentially from the outset of the elastic deformation and up to 500-600s. The duration of the linear elastic deformation extended over the first ~20s after the load was applied. After the primary phase, the strain continued to increase but at a constant rate of $3.3\times10^{-6}s^{-1}$ during the secondary phase of the response. Notably, the measurement was terminated, and the load was removed before the polymer could transition into the final and terminal tertiary creep region, *i.e.*, no mechanical failure occurred in any of the tested samples. The ratio of the lateral strain, ε_x, and axial strain, ε_y, remained nearly constant at *ca.* 0.42, implying that Poisson's ratio is insensitive to the underlying time-dependent processes responsible for the creep behavior reported in Fig. 5.1b. This conclusively confirms the standing presumption about the time-independent incompressible behavior of polyurea, where the deviatoric deformations commonly account for the relaxation and creep behaviors, *i.e.*, inherit the viscoelastic response. This is further demonstrated with the relatively negligible in-plane rotations while substantiating gravity-assisted uniaxially applied stress state. Finally, the primary and secondary creep regions were independently fitted into the Norton-Bailey law; the fitting parameters are tabulated in Appendix Table 5.A1. The drastic difference between the primary and secondary creeps is captured in the time-dependent coefficient of the Norton-Bailey equation, representing the viscous material compliance, where $\phi \approx 1.25 \times 10^{-5}\mathrm{MPa}^{-1}\cdot\mathrm{s}^{-1}$ in the primary creep region, increasing to $\phi \approx 1.475 \times 10^{-4}\mathrm{MPa}^{-1}\cdot\mathrm{s}^{-1}$ in secondary creep. The Norton stress power-law yielded an exponent in the primary twice that of the secondary creep, *i.e.*, $\alpha_p = 2\alpha_s = 4$, indicating the fast development of primary creep strains compared to the slower growth in the secondary region. Finally, Bailey's exponent indicated a strain-softening phenomenon dominating the time-dependent deformation behavior of polyurea since $\beta \approx 0.35 < 1$. The dependence on temperature was suppressed since the measurements were done at isothermal conditions $T = 21 \pm 0.7°C$ and constant relative humidity $41.2 \pm 4.1\%$.

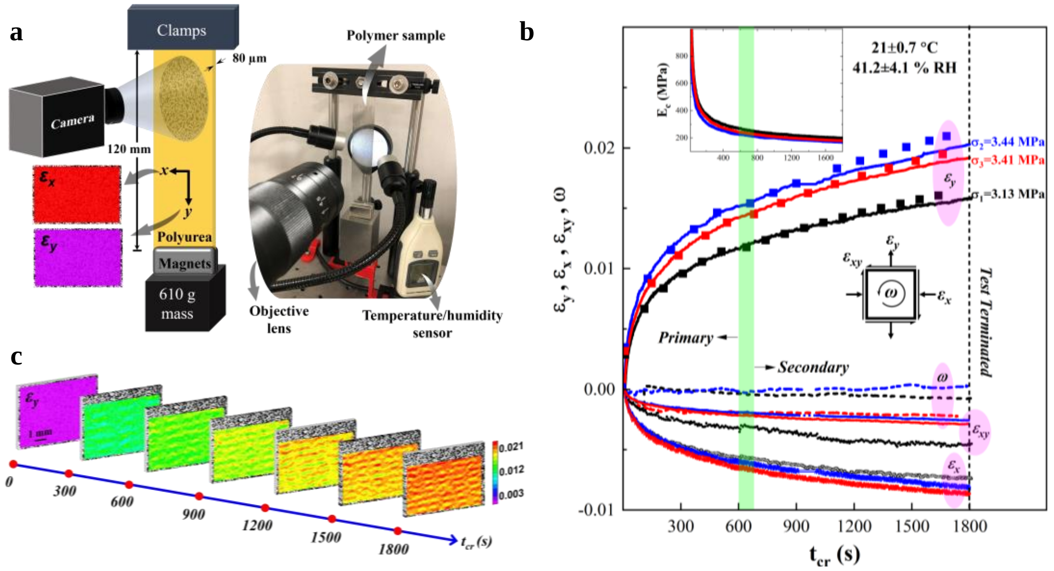

Figure 5.1: (a) Schematic and pictorial diagrams of the experimental setup to concurrently load elastomer films while capturing high-resolution speckled digital images. (b) The time dependence of in-plane strain components over three decades of time while the inset in b shows the creep modulus over the loading time. (c) Full-field contours of interest of the axial strain (ε_y).

Here, we reveal, for the first time, the mild anisotropic behavior of elastomeric polyurea despite the common presumption of its isotropy. Such anisotropic response is manifested in the reported shear strains from full-field measurements. The results in Fig. 5.1b indicate the existence of a shear strain component throughout the entire creep history, even though the stress state was expected to be uniaxial, as guaranteed by the gravity-assisted normal loading. In the Appendix, the inverse problem was then solved based on the resulting state of strain, $\{\varepsilon_x, \varepsilon_y, \varepsilon_{xy}\}$, and the measured properties of polyurea, showing the coexistence of normal and shear stresses. A noteworthy byproduct of the inverse problem is the close match between the modulus calculated from the analysis of the raw data ($E \approx 182$MPa) and the time-modified Norton-Bailey coefficient ($t_{pc}/\phi \rightarrow E \approx 192$MPa, where t_{pc} is primary creep duration). Hence, elastomeric polyurea exhibits a mild anisotropy based on underlying molecular processes, supported by the terahertz results discussed next.

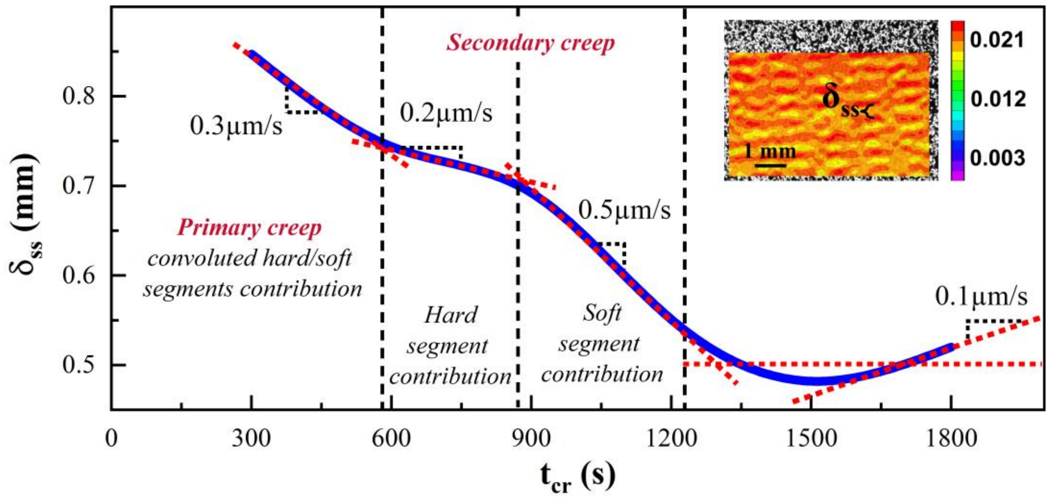

Figure 5.2: Association of segmental mobility with changes of strain striation as a function of t_{cr} delineated into four discernible regimes, where the striations motion records different rates attributed to the convoluted hard and soft segments mobility from the creep strain energy.

The utilized DIC approach revealed a unique strain localization phenomenon, exemplified by sequential striations of low strain regions lagging adjacent areas (Fig. 5.1c), where the strain appeared to be 0.45% higher. Interestingly, the localized deformation appears to have occupied a larger surface area (observed in the contour strain plots, esp. at a longer lapsed time). The strain localization evidently arisen from the segmental microstructure of polyurea, where the soft segments, arising from the aromatic group in the oligomeric diamine, occupies 34-40%, $R(M_{od})/(M_{od} + M_{mdi})$, where R is the molar ratio of the oligomeric diamine to the modified MDI, and M_{od} and M_{mdi} are the molecular weights of the aromatic diamine and the aliphatic diisocyanate, respectively). The regions of strain localization elucidate the drastic difference in the mechanical properties of the segments that constitute the segregated molecular structure of polyurea. The striation formation embodied in ε_y reveals two additional underlying mechanisms. First is the preferential arrangement of the soft segments at high strain in nearly continuous formation distal to the loading site, while the discontinuities proximal to the suspended mass exemplify the transient rearrangement process where the hard segments act as pinning sites, restricting the motion and resulting in lower deformation. The inherent slow creep rate ingrained in the experimental method delayed the accumulation of the strain localization while providing the necessary evidence to substantiate this phenomenon. Second is the narrow gradual transitional regions sandwiched between the high localized deformation and the areas, where the strain continues to develop. The stiffness of the urea-links connecting the oligomeric diamine to the MDI segments appears to define the mechanical behavior of these transitional regions in the deformation response.

The striation spacing (δ_{ss}) was extracted from the contour plots reported from the DIC analysis and plotted in Fig. 5.2, denoting four distinct regions. Initially, δ_{ss} decreased at a rate of 0.3µm/s, attributed to the primary creep that resulted from a convoluted interplay between the deformations of the hard and soft segments. Then, remarkably, the striation distance measurements revealed two secondary creep regions at distinctively descending rates of 0.2µm/s and 0.5µm/s associated with the interchain hydrogen bonding mobility within the hard segments and the uncoiling and stretching of the soft segments, respectively, since the latter lacks interchain hydrogen. The final region in the striation spacing-time history is characteristic of pseudo-time-hardening behavior; the inter-striation spacing is reverting at an ascending rate of 0.1µm/s due to relaxation at the interphasic region separating the hard and soft segments.

5.3 Terahertz spectroscopy

Analysis of the THz power-time signals, $P_{THz} = E^2{}_{THz}$, reveal two fundamental processes associated with the molecular changes occurring in the segregated microstructure during creep loading. To delineate these changes, the area under the THz power curves, capturing the signal energy under the main peak, *i.e.*, Peak 2, and the temporal characteristics (*i.e.*, rise and fall times) of the individual peaks were extracted from the THz power signals. The P_{THz} exhibits a sudden increase in the energy, corresponding to the onset of secondary creep of the hard segments and reaching a plateau, thereafter, corroborating the observations discussed previously based on the creep analysis. Such a sudden increase is only attributed to the hard segments, given the presence of interchain hydrogen bonding within, which is readily detected using THz-TDS due to the low energy of the interrogating wave. The low energy level preceding the transition is notably higher than the nearly constant signal energy of the unloaded sample (Fig. 5.3c). That is to say, the interchain hydrogen bonding mobility within the hard segment not only starts at the onset of loading but also persists throughout the entire loading history, however, at a lower level after the transition. It is worth noting that the samples were macroscopically and microscopically failure-free after loading, implying changes to the THz signals are solely attributed to elastically-dominated molecular changes within the hard segments.

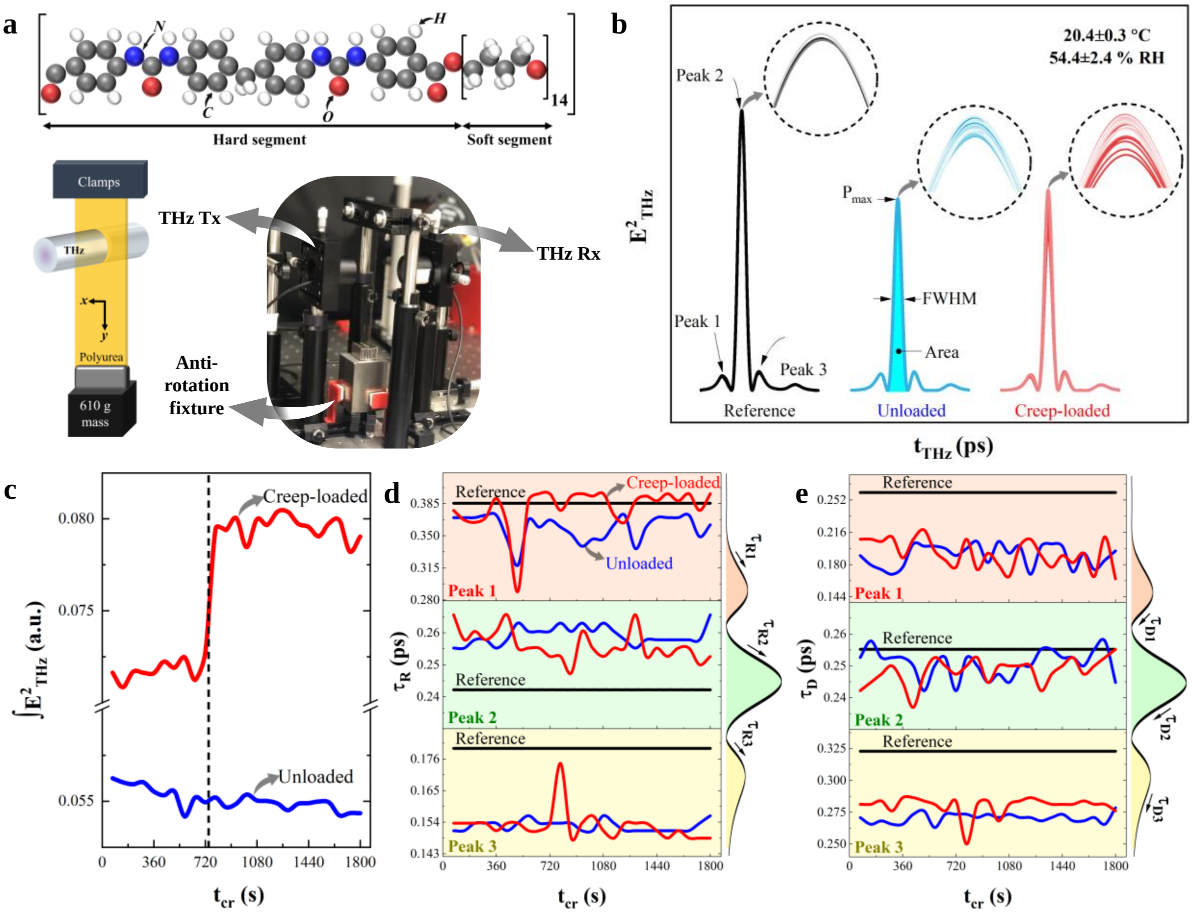

Figure 5.3: (a) Representative molecular structure (top panel) of polyurea elastomer and schematic and pictorial illustrations of the experimental setup. The (b) transmitted terahertz signal power ($E^2{}_{THz}$) signals, demonstrating the repeatability of the reference and pre-load signals, where (c-e) the temporal characteristics of the transmitted terahertz waves provide evidence for molecular conformational changes in the creep-loaded samples.

Within the onset of secondary creep ($500s \preccurlyeq t_{cr} \preccurlyeq 600s$), the rise time of the first peak from the signals collected during loading exhibit an increase compared to the unloaded counterparts. The slowing in the rise time upon loading indicates a corresponding decrease in the stiffness within the macromolecule conformations, translating to a change in the macroscale stiffness, *i.e.*, the creep modulus, as shown in the inset Fig. 5.1b. Interestingly, the decay times of the first peaks have a negative slope as a function of creep loading time while the decay times of the unloaded signals remained constant, implying that damping has decreased and resulted in a quicker time to rest before the second set of molecular vibrations takes place embodied in the second peak. The decay times for the loaded and unloaded signals were ~50fs lower than the reference, sample-free signal due to the inherent damping characteristics of elastomeric polymers based on the ubiquitous viscoelastic properties. Similarly, the decay times of the third peaks were much lower than the reference (*ca.* 50fs, on average); however, the apparent negative slope in the decay times of the unloaded signals has vanished in the loaded counterpart. In the case of the third peak, the decay times also point towards an increase in damping, compensating for the decrease associated with the first peak. Subsequently, the temporal characteristics of the second peak remained nearly unchanged before and during loading, where the peak is symmetric. Therefore, the evolution of the temporal characteristics of each of the three peaks of interest (with respect to the reference, sample-free signal) elucidates the molecular changes discussed previously, associated with the mechanical response that stems from the conformational changes within the soft/hard segregated segmental structure. The raw time-domain terahertz signal revealed physical evidence of the molecular processes responsible for the macroscale creep deformation.

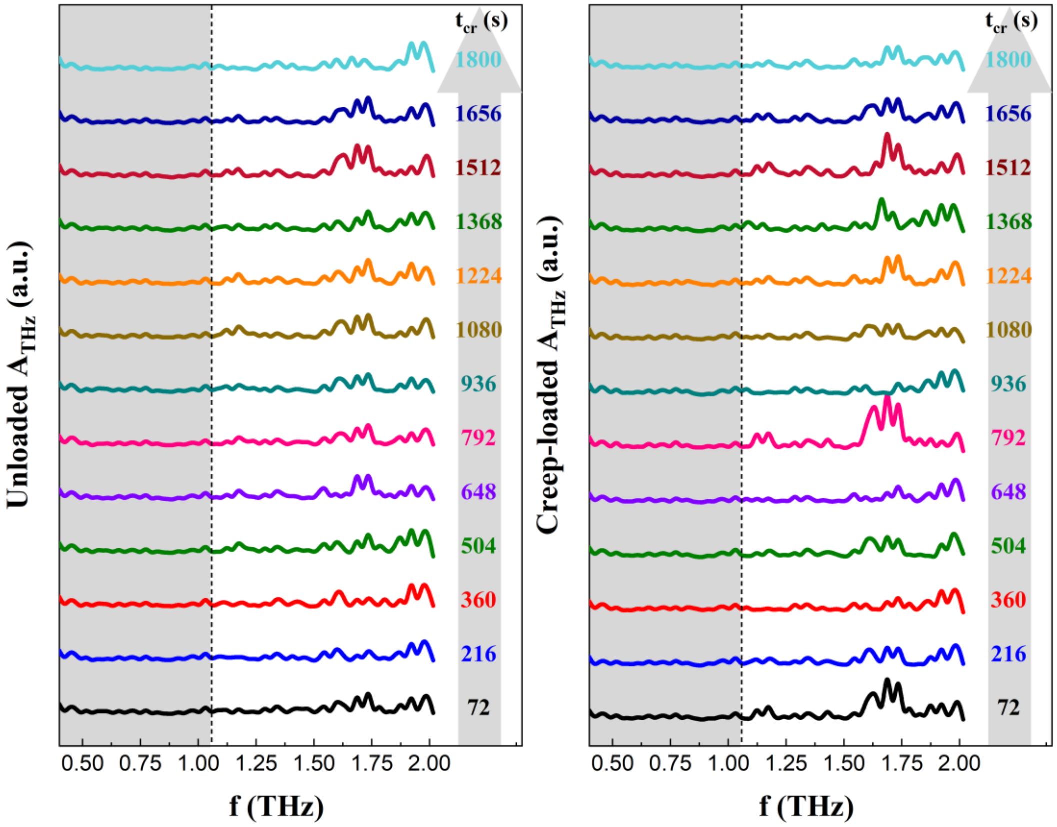

Figure 5.4: Terahertz spectra of polyurea at different creep time, t_{cr}, before loading (left panel) and during loading (right panel). Each spectrum underwent baseline subtraction to elucidate minor peaks throughout the investigated bandwidth.

Terahertz spectral analysis (Fig. 5.4) enabled pinpointing the source of molecular vibrations by attributing spectral absorption peaks to the segmental structure of polyurea and their relative mobility throughout the loading time. The lack of significant spectral features for $f \lesssim 1THz$ is primarily associated with hard aliphatic isocyanate segments based on the prominence of structural restriction provided by the benzene rings. The quiescence region within $f \lesssim 1THz$ persisted throughout all the measurements whether before loading commenced or during loading. The stagnation of the spectra features within this frequency regime, specifically while the polymer was undergoing creep response, indicates that the contributions of the hard segments to the creep response is limited to the mesoscale and the conformational changes within the hard domains are negligible. The former implies that relative mobility of the hard segments is mainly due to the relatively large deformation within the soft segments, as demonstrated earlier by the dichotomy in the striation motion rate within secondary creep. On the other hand, the latter suggests that the minor spectral evolution within the frequency regime of $f \preccurlyeq 1THz$ might be attributed to slight fluctuations in the surrounding environment. The case is different at frequencies above this threshold, where spectral features become extant or extinct. In general, these spectral signatures when $1THz < f \preccurlyeq 2THz$ are associated with interchain hydrogen bonds between the hard segmentation, torsional vibrational modes of urea linkages, and the chemical attributes of the soft segments [19]. For $f > 1THz$, significant spectral changes are observed, including broadening and sharpening and appearance or extinction of absorption peaks (denoted in Fig. 5.4) such as the conformational activities at $f \simeq 1.2THz$ and $f \simeq 1.67THz$. The attribution of the spectral changes to the soft segments mobility during creep loading stems from the dominance of the aromatic domain motions within secondary creep.

5.4 Creep light scattering

An interaction between a monochromatic light source and microstructurally inhomogeneous elastomeric samples resembles a light scattering of suspensions in a dilute in terms of the dynamics as foreseen by Rayleigh scattering and Fraunhofer diffraction theories. Fig. 5.5a is the normalized scattering intensity of a 632.8nm monochromatic light (also frequency-stabilized) calculated based on the illumination of the light through the polyurea strips with the segmental microstructure, consisting of hard and soft segments. The light intensity time-histories in Fig. 5.5a concurrently highlight the dynamic and quasi-static scattering responses as a function of creep time, exemplifying the hard segments mobility within the less viscous soft segments due to the mechanical creep loading. Once secondary creep response has completely developed within the sample, *i.e.*, deformation at a constant rate, the changes in intensity, irrespective of the behavior within the transient scattering region, reached a steady state, where the normalized intensity plateaued around 1200s. Immediately before, the intensity appears to be changing at a constant rate leading to the quasi-static plateau, elucidating the hard segment interactions with the light as previously delineated in Fig. 5.2 by studying the evolution of strain localization. That is to say, the stretching of the mechanically-compliant soft segments within the secondary creep regime is not necessarily coupled with movement of the rigid hard segments indicated by the apparent plateau in the light intensity plot. In the transient region, however, the dichotomy of the dynamic scattering behavior reveals the hard segment mobility as they move in and out of the detectable field of view (*i.e.*, the detector screen). Here, the slight microscopic changes due to the random dispersity of the segmental structure of the investigated elastomeric material (denoted by the dynamic evolution of the light intensity in Fig. 5.5a) are also delineated in the experimental scattering phase portraits shown in Fig. 5.5b. The preceding light-segmental elastomeric polymer interaction mechanisms are summarized in Fig. 5.5c, where the light intensities are lower in areas corresponding to the hard segments (dense regions in the figure), while higher intensities are associated with the soft fibril segments.

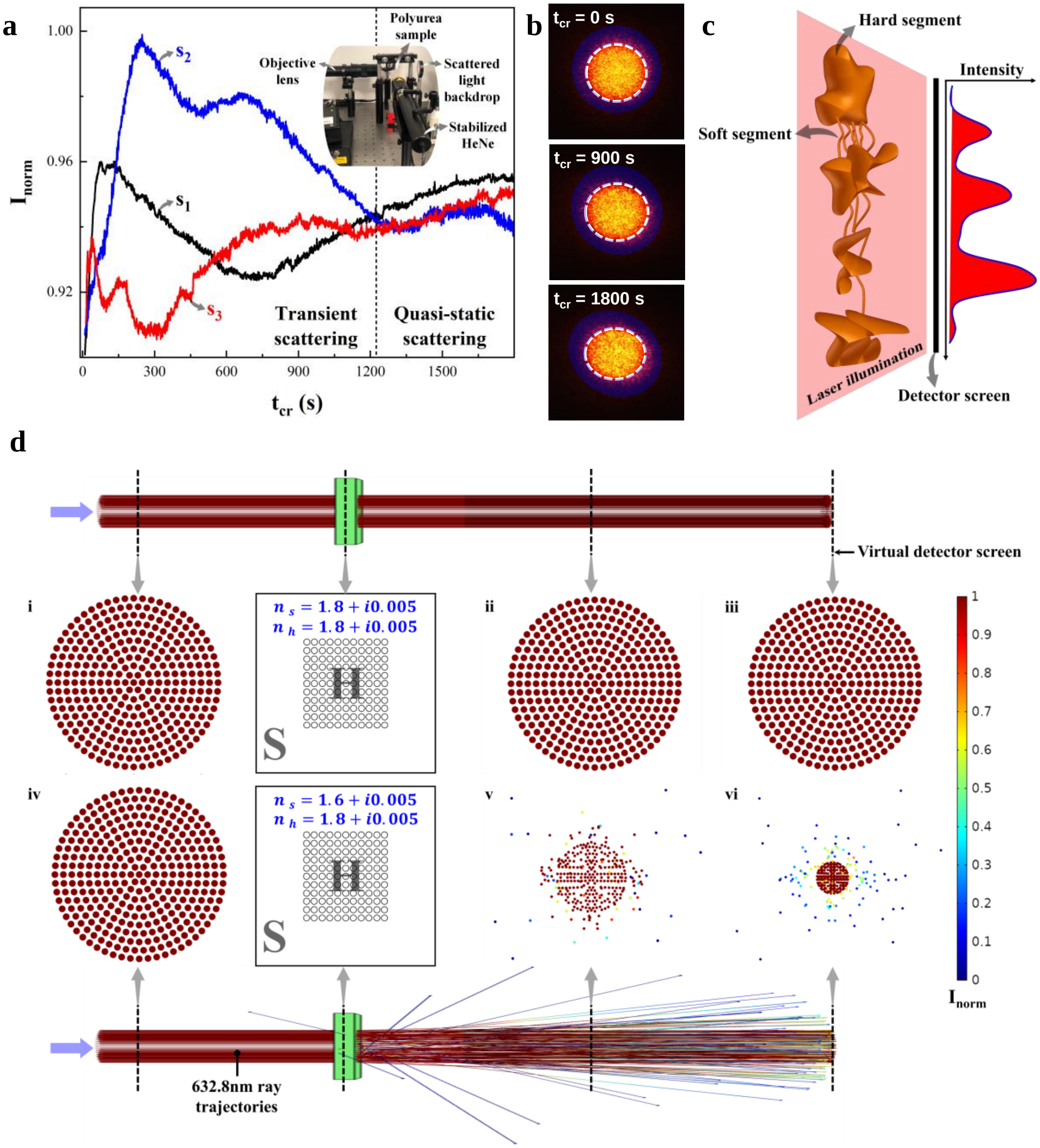

Figure 5.5: Resulting (a) plots of the normalized transmitted monochromatic light intensity from three different samples, (b) scattering pattern at the onset (top panel) and outset (bottom panel) of creep loading, (c) model representation of the light-material interaction between the monochromatic light interacting with the hard and soft segments, and (d) simulated phase portraits at different locations along the ray trajectory.

A companion geometrical ray tracing computational simulation (details in the Appendix) was used to further study the contributions of the hard and soft segments on the resulting light scattering. In the case of a homogenous material where all the domains are assigned the same complex refractive index, a collimated light beam suffers only a negligible reduction of the intensity without any apparent scattering or diffraction, as shown in the computational phase portraits in Fig. 5.5d (panels i-iii). On the other hand, a significant scattering and attenuation was calculated when the hard segments, $n_h = 1.8 + i0.005$, were represented by idealized spherical regions embedded within the soft segment matrix with a different complex refractive index, $n_s = 1.6 + i0.005$. Remarkably, the reduction in the normalized intensity for the case of the inhomogeneous continuum was in excellent agreement with the experimental data, substantiating the light scattering mechanism discussed above based on the segmental microstructure in the investigated elastomeric polymer.

5.5 Methods

5.5.1 Fabrication and mechanical loading

Thin sheets of ~80μm thick polyurea were fabricated using spin coating by slowly and thoroughly mixing an amine (oligomeric diamine) with isocyanate (olycarbodiimide-modified diphenylmethane diisocyanate) in a 1:1 stoichiometric ratio (*i.e.*, 4:1 weight ratio, respectively). A total of 6 sheets were initially fabricated, allowing the extraction of two samples from each sheet, where the dimensions of individual samples were 24mm wide x 142mm long. Additional details of the deposition and curing processes can be found in the Appendix. Three sets of experimental characterization were performed to elucidate the multiscale dynamic behavior of elastomeric polymers, exemplified by polyurea, ranging from the molecular scale to the meso and micro scales. Regardless of the type of characterization, each strip was mechanically loaded by magnetically suspending a steel weight (*ca.* 610g) from one end while fixating the other end by clamping the strip. The applied stress, ranging from 3.2MPa to 3.4MPa, was held constant for 1800s. The corresponding figures discussed in the results section capture the following characterization techniques used to explicate the dynamic evolution of polyurea mechanical and molecular behaviors.

5.5.2 Strain measurements

The strain components were measured using a digital image correlation (DIC) method based on digital photographic images collected concurrently to the mechanical loading. The front surface of each strip sample was coated with an ultrathin random speckle pattern produced by a diluted black paint applied using an airbrush. The images were captured at a rate of 10fps using a digital camera (Basler, acA1300-30gc) fitted with magnifying and focusing lenses. The captured images were used as input to a digital image correlation software (Vic-2D, Correlated Solutions, Inc.). The in-plane strain components were determined during the DIC analysis using subset, step, and strain filter sizes of 41 pixels (214µm), 10 pixels (52µm), and 5, respectively. Full-field strain maps were also extracted at different time increments, as shown in Fig. 5.1c, which were used collectively with the strain components data to elucidate the dynamic mechanical behavior of polyurea. The axial strain data was also used to calculate the creep characteristics of polyurea, including the creep modulus and creep strain rate, by fitting the dynamic response into the Norton-Bailey law ($\varepsilon_c = \phi\sigma^{\alpha}t^{\beta}$, where ϕ, α, and β are parameters found by curve fitting the creep stages piecewise, *i.e.*, the primary and secondary creep have different parameter values) [19]. Details of the fitting process are included in the Appendix.

5.5.3 Terahertz characterization

The molecular-scale characterizations were carried out using built in-house terahertz time-domain spectroscopy, operating in the transmission mode. The spectroscopic signals (25 terahertz waveforms) were collected in-operando while the strip samples were creep loaded at ambient conditions (20.4±0.3°C and 54.4±2.4% RH) at a time interval of 30s/signal. A pulsed femtosecond laser (Menlo systems, ELMO 780 HP) with a repetition rate of 100MHz and average pulse width of 85fs was focused onto a biased photoconductive antenna (Batop, PCA-40-05-10-800) with a bias voltage of 40Vpp and a modulating frequency of 10kHz. The generated, diverged terahertz wave from the photoconductive emitter was collimated using a TPX lens (*f*=32.5mm). Prior to focusing the wave onto the receiving photoconductive antenna (Batop, bPCA-100-05-10-800) with a second TPX lens, the collimated beam interrogates each sample with an 18.4mm diameter beam spot. The bandwidth of the setup was determined to be 0.2-2THz. The time-domain data were transformed to the frequency domain using fast Fourier transform (FFT), where each spectrum was subsequently analyzed to extract the dynamical evolution of the spectral changes in polyurea during loading. The time-domain data was also exploited to reveal additional molecular processes concealed in the frequency domain.

5.5.4 Light scattering measurements

Light scattering analyses were conducted using a collimated beam from a monochromatic, frequency-stabilized 632.8nm laser (Newport™, N-STP-912). The laser beam was passed through the loaded strip polyurea samples, where the projected scattered and diffracted light (on a white screen) was recorded using a digital camera (Basler, acA1300-30gc). The images were collected at a rate of 1fps, which were then analyzed to elucidate mesoscale changes by detecting morphological changes from one frame to another.

Acknowledgement

Chapter 5, in part, is currently being prepared for submission for publication of the material. Huynh, Nha Uyen; Koohbor, Behrad; Youssef, George. The dissertation author was the primary researcher and author of this material.

References

1. Gupta, V. & Youssef, G. Orientation-Dependent Impact Behavior of Polymer/EVA Bilayer Specimens at Long Wavelengths. *Exp. Mech.* **54**, 1133–1137 (2014).

2. Mohotti, D., Ngo, T., Mendis, P. & Raman, S. N. Polyurea coated composite aluminium plates subjected to high velocity projectile impact. *Mater. Des.* **52**, 1–16 (2013).

3. Grujicic, M. & Pandurangan, B. Mesoscale analysis of segmental dynamics in microphase-segregated polyurea. *J. Mater. Sci.* **47**, 3876–3889 (2012).

4. Blourchian, A., Shaik, A. M., Huynh, N. U. & Youssef, G. Segmental evolution of ultraviolet weathered polyurea. *J. Polym. Res.* **28**, (2021).

5. Youssef, G. & Gupta, V. Resonance in Polyurea-Based Multilayer Structures Subjected to Laser-Generated Stress Waves. *Exp. Mech.* **53**, 145–154 (2013).

6. Jain, A., Youssef, G. & Gupta, V. Dynamic tensile strength of polyurea-bonded steel/E-glass composite joints. *J. Adhes. Sci. Technol.* **27**, 403–412 (2013).

7. Huynh, N. U., Gamez, C. & Youssef, G. Spectro-Microscopic Characterization of Elastomers Subjected to Laser-Induced Shock Waves. *Macromol. Mater. Eng.* **307**, 2100506 (2021).

8. Wang, J., Weaver, R. & Sottos, N. A parametric study of laser induced thin film spallation. *Exp. Mech.* (2002).

9. *Elastomeric Polymers with High Rate Sensitivity*. (Elsevier, 2015).

10. Huynh, N. U. & Youssef, G. Physical Evidence of Stress-induced Conformational Changes in Polymers. *Exp. Mech.* (2020) doi:10.1007/s11340-020-00673-7.

11. Jansen, C. *et al.* Terahertz imaging : applications and perspectives. (2010).

12. Ransom, T. C., Ahart, M., Hemley, R. J. & Roland, C. M. Acoustic properties and density of polyurea at pressure up to 13.5 GPa through Brillouin scattering spectroscopy. *J. Appl. Phys.* **123**, (2018).

13. Rosenbloom, S. I., Yang, S. J., Tsakeredes, N. J., Fors, B. P. & Silberstein, M. N. Microstructural evolution of polyurea under hydrostatic pressure. *Polymer (Guildf).* **227**, 123845 (2021).

14. Kim, K.-S., Jin, H. & Jiao, T. Dynamic Fracture-Toughness Testing of a Hierarchically Nano-Structured Solid. in.

15. Heyden, S., Ortiz, M. & Fortunelli, A. All-atom molecular dynamics simulations of multiphase segregated polyurea under quasistatic, adiabatic, uniaxial compression. *Polymer (Guildf).* **106**, 100–108 (2016).

16. Manav, M. & Ortiz, M. Molecular dynamics study of the shock response of polyurea. *Polymer (Guildf).* **212**, 123109 (2021).

17. Chang, K. S., Yoshioka, T., Kanezashi, M., Tsuru, T. & Tung, K. L. A molecular dynamics simulation of a homogeneous organic-inorganic hybrid silica membrane. *Chem. Commun.* **46**, 9140–9142 (2010).

18. Dewapriya, M. A. N. & Miller, R. E. Quantum and classical molecular dynamics simulations of shocked polyurea and polyurethane. *Comput. Mater. Sci.* **203**, 111166 (2022).

19. Zhao, Y. *et al.* Intermolecular vibrational modes and H-bond interactions in crystalline urea investigated by terahertz spectroscopy and theoretical calculation. *Spectrochim. Acta - Part A Mol. Biomol. Spectrosc.* **189**, 528–534 (2018).

20. Youssef, G. *Applied Mechanics of Polymers*. (Elsevier, 2021).

Appendix

5.A1. Sample Preparation

Polyurea, a thermoset elastomer, sheets were prepared by thoroughly mixing Versalink P1000 with Modified Isocyanate at a ratio of 4:1, corresponding to a 1:1 stoichiometric ratio. Once the two parts were added together in the mixing container, the mixture was slowly stirred using a stainless- steel stirrer to avoid the introduction or entrapment of bubbles. The mixture was added to the top of a polypropylene wafer (polyurea easily lifts off polypropylene) and left to rest for 270s, followed by spinning at 400rpm for 600s. The sheets were then left to cure at ambient condition for 7h and in a heated vacuum environment at 80°C for an additional 12h. The polyurea sheets were then lifted off the polypropylene wafer and cut into strips 24mm wide and 142mm long. The thicknesses were measured using ultrasound transducer (PosiTector 6000, DeFelsko) by taking at least 15 measurements along the length of each strip, reporting a thickness of 79.9±3.5μm.

5.A2. Digital Image Correlation

Figure 5.A1 shows a series of full-field strain maps extracted from the samples at the specific time increments.

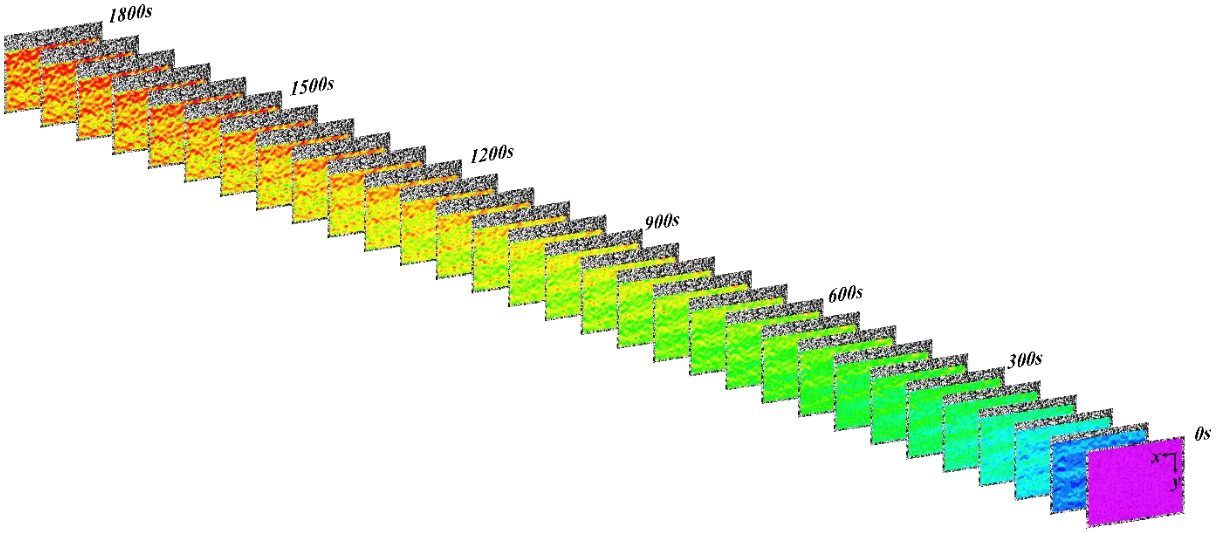

Figure 5.A1: Creep strain components and full-field maps calculated using DIC.

5.A3. Norton-Bailey Fitting Process

Table 5.A1: Parameters from piecewise fitting of the Norton-Bailey law for primary and secondary creep of each sample.

σ_1					
Primary			**Secondary**		
ϕ	**α**	**β**	**ϕ**	**α**	**β**
2.8x10^{-5}	3	0.35	1.00x10^{-4}	2	0.33

σ_2					
Primary			**Secondary**		
ϕ	**α**	**β**	**ϕ**	**α**	**β**
1.2x10^{-5}	4	0.35	1.53x10^{-4}	2	0.33

σ_3					
Primary			**Secondary**		
ϕ	**α**	**β**	**ϕ**	**α**	**β**
1.13x10^{-5}	4	0.35	1.45x10^{-4}	2	0.33

5.A4. Inverse problem

As discussed in the main document, we solved the inverse problem by finding the corresponding values of the stress field using

$$\begin{bmatrix}\sigma_x\\ \sigma_y\\ \tau_{xy}\end{bmatrix}=\frac{E}{(1-\nu^2)}\begin{bmatrix}1 & \nu & 0\\ \nu & 1 & 0\\ 0 & 0 & {(1-\nu)}/{2}\end{bmatrix}\begin{bmatrix}\varepsilon_x\\ \varepsilon_y\\ \varepsilon_{xy}\end{bmatrix}$$

Where the values of the strains were measured using the DIC framework, $\{-0.0086, 0.019, -0.0014\}$, from Fig. 5.1b in the main document and the value of σ_y was forced to be 3.4MPa based on the boundary conditions. The resulting stresses based on adjusting all remaining elements in Eq. 5.S1 are

$$\begin{bmatrix}-137\\ 3400\\ -90\end{bmatrix}=\begin{bmatrix}220951 & 92800 & 0\\ 92800 & 220951 & 0\\ 0 & 0 & 64076\end{bmatrix}\begin{bmatrix}-0.0086\\ 0.019\\ -0.0014\end{bmatrix} \tag{5.S1}$$

using the values of E=182MPa and ν= 0.42.

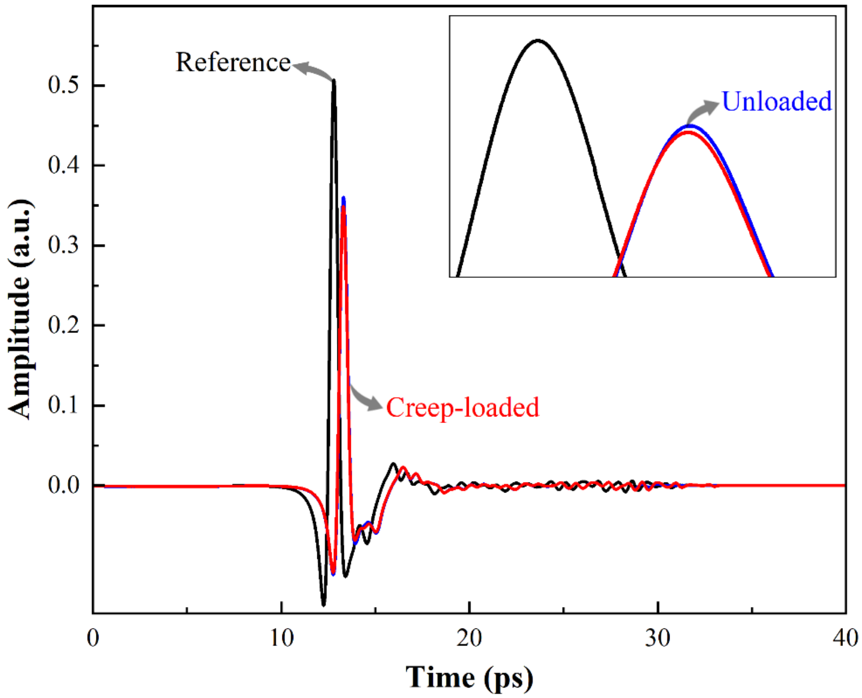

Figure 5.A2: Raw terahertz signal of the air reference, unloaded, and creep-loaded sample.

5.A5. Ray Tracing Computational Study

To supplement the scattering analysis, finite element simulation of light-matter interactions of a 632.8nm beam and polyurea element, 1mm×1mm×80µum, were executed using the ray optics module in Comsol Multiphysics. 40µm spherical particles, representing hard segments, were embedded in a soft segment matrix. The incident beam was released 1mm from the polyurea element and the ray trajectories upon interaction with sample traveled an additional 2mm. From the experimental result of the three samples, the average transmission intensity was found to be 73±1.4% of the incident beam intensity; therefore, a value of 0.005 was selected for the extinction coefficient to match that of the experimental data. Huynh and Youssef found the refractive index of polyurea in the terahertz regime to be ~1.67, thus, the average *n* (the index of refraction) of the segmental phases were designed to meet this criterion.

FUTURE WORK

The research leading to this dissertation introduced a novel and fully-integrated experimental solid mechanics characterization framework, consisting of an external loading mechanism coupled with a bulk spectroscopy technique. The former can submit the material to mechanical loading at a broad range of strain rates to investigate the quasi-static and dynamic behaviors, including creep (Chapter 5) and shock wave testing (Chapter 3). In one set of experiments, elastomeric polymer samples were subjected to constant stress while recording the creep response over three decades [1]. In another set, the same polymer was loaded with shock waves at a strain rate of 10^7 s^{-1} [2]. The bulk spectroscopy, specifically terahertz time-domain spectroscopy, can nondestructively interrogate polymers and capture inter and intramolecular vibrations associated with the material's mechanical response. THz-TDS is also experimentally versatile, allowing several configurations depending on the load modality. For example, transmission THz-TDS was used during the creep experiment, while a right-angle reflective THz-TDS was better suited for experiments at ultrahigh strain rates. Remarkably, it was also demonstrated that other loading mechanisms and characterization approaches could be readily integrated to gain further insight, including thermal or electrical loading and dynamic light scattering or digital image correlation, respectively. Indeed, the experimentation development undertaken by this research conclusively elucidated that light-matter interactions can be exploited beyond the state-of-the-art to gain a fundamental understanding of the mechanical behavior of materials at a wide range of spatial (molecular-to-macro) and temporal (femto-to-seconds) scales.

The overarching focus of this research was on the concurrent mechano-spectroscopic characterization of elastomers, however, materials used in real life scenarios endure the combined effects of mechanical, thermal, electrical, magnetic, chemical, and radiation settings. Therefore, future research can explore two objectives using the integrated laser-induced shock waves and terahertz spectroscopy. First is achieving a fully integrated in-operando experimental solid mechanics setup, where electroactive, photoactive, or magnetoactive polymers can be loaded with electric, illumination, or magnetic fields separately or concurrently. Here, a comprehensive investigation is required to study the interactions between the external field (e.g., electric or magnetic) and the polarization and intensity of the interrogating terahertz waves. For example, the strength and direction of a magnetic field can substantially influence the terahertz waves since electromagnetic waves consists of orthogonal magnetic and electric field waves. Such interactions are further complicated by the effect of the magnetic field on the magnetoactive materials, where the magnetic domains tend to rotate to align with the direction of the applied field, in the process emanating a stray field that may influence the measurements. Therefore, these interrelationships must be fully understood *a priori*.

Second is packaging the in-operando setup into an environmentally controlled chamber, where the gas species are purged in or evacuated out systematically to elucidate the chemo-active nature of freshly failed or activated materials. For example, it has been shown before that shock loading single crystal copper nanopillars results in dislocation mobility that hyper activate the failed surface and increase the propensity of the material to react with the surrounding [3]. Hence, controlling the environment provides unprecedented scientific opportunity to observe the evolution of freshly failed surfaces as a function of the reactivity of the surroundings.

A hidden experimental challenge, also constitute its limitation, of the discussed integrated experimental setup is the extraordinarily laborious effort spent for optical alignments. In the current free-space setup, there are several laser systems and a few dozen optical components working in tandem to load and characterize the samples. Future research should consider streamlining the setup by replacing the free-space optics with fiber mode counterparts, leading to accelerating the collection of data and paving the pathway to more scientific discoveries.

References

1. Huynh, N. U., Koohbor, B. & Youssef, G. *Light-matter interactions revealing load-induced phase mobility in elastomers*. (2022).

2. Huynh, N. U., Gamez, C. & Youssef, G. Spectro-Microscopic Characterization of Elastomers Subjected to Laser-Induced Shock Waves. *Macromol. Mater. Eng.* **307**, 2100506 (2021).

3. Youssef, G. *et al.* The influence of laser-induced nanosecond rise-time stress waves on the microstructure and surface chemical activity of single crystal Cu nanopillars. *J. Appl. Phys.* **113**, (2013).